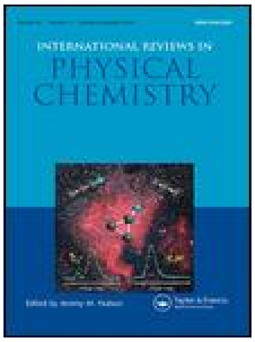

International Reviews in Physical Chemistry

ISSN: 0144-235X (Print) 1366-591X (Online) Journal homepage: http://www.tandfonline.com/loi/trpc20

# Photoelectron spectroscopy of size-selected boron clusters: from planar structures to borophenes and borospherenes

Lai-Sheng Wang

**To cite this article:** Lai-Sheng Wang (2016) Photoelectron spectroscopy of size-selected boron clusters: from planar structures to borophenes and borospherenes, International Reviews in Physical Chemistry, 35:1, 69-142, DOI: 10.1080/0144235X.2016.1147816

**To link to this article:** http://dx.doi.org/10.1080/0144235X.2016.1147816

*International Reviews in Physical Chemistry*, 2016
Vol. 35, No. 1, 69–142, http://dx.doi.org/10.1080/0144235X.2016.1147816

# Photoelectron spectroscopy of size-selected boron clusters: from planar structures to borophenes and borospherenes

Lai-Sheng Wang*

*Department of Chemistry, Brown University, Providence, RI 02912, USA*

(*Received 20 October 2015; final version received 24 November 2015*)

Photoelectron spectroscopy (PES) in combination with computational chemistry has been used systematically over the past decade to elucidate the structures and chemical bonding of size-selected boron clusters. Small boron clusters have been found to be planar or quasi-planar, consisting of a monocyclic circumference with one or more interior atoms. The propensity for planarity has been found to be a result of both $\sigma$ and $\pi$ electron delocalisation over the molecular plane, giving rise to concepts of $\sigma$ and $\pi$ multiple aromaticity. In particular, the $B_{36}$ cluster has been found to possess a highly stable planar structure with a central hexagonal vacancy. This finding provides the first indirect experimental evidence that single-atom layer boron-sheets with hexagonal vacancies, dubbed 'borophene', are potentially viable. Another exciting discovery has been the observation and characterisation of the first all-boron fullerenes. PES revealed that the $B_{40}^-$ cluster consisted of two isomers with very different electron binding energies. Global minimum searches led to two nearly degenerate isomers competing for the global minimum: a quasi-planar isomer with a double hexagonal vacancy and an unprecedented cage isomer. In the neutral, the $B_{40}$ cage is overwhelmingly the global minimum, which is the first all-boron fullerene to be observed and is named 'borospherene'. Rapid progresses in our understanding of the structures and bonding of size-selected boron clusters have been made during the past decade, which will be the focus of this review. The recent findings about borophenes and borospherenes have stimulated growing interests in boron clusters and will accelerate the pace of discovery in boron chemistry and nanostructures.

**Keywords:** photoelectron spectroscopy; boron clusters; aromaticity; borophenes; borospherenes

## Contents

---

*Email: Lai-Sheng_Wang@brown.edu

## 1. Introduction

Boron is an interesting element with diverse and complicated chemistry owing to its electron deficiency [1]. Even elemental boron possesses complex polymorphs with a variety of polyhydra, in particular, the $B_{12}$ icosahedron, as building blocks [2], to accommodate the electron deficiency. Boron–boron bonding is exceptionally strong, as manifested by the fact that all boron polymorphs are superhard materials [3]. The strong bonding capacity of boron suggests that boron may be the basis to discover novel nanostructures. However, in comparison to its neighbour carbon, relatively little experimental attention was paid to boron clusters. The only earlier experimental studies on boron clusters were done by Anderson and co-workers, who investigated the collision-induced dissociation and chemical reactivity of small boron cluster cations using a guided-beam tandem mass spectrometer [4–8]. Inspired by the discovery of the fullerenes, mass spectra of boron clusters with sizes up to ~50 atoms were produced [9,10]. However, there was no structural or spectroscopic information for any boron clusters before photoelectron spectroscopy (PES) in combination with computational chemistry was first used to investigate size-selected boron clusters in 2002 [11].

Even though the $B_{12}$ icosahedral cage is the most common building block in many boron polymorphs, earlier theoretical calculations by Kawai and Weare using molecular dynamics simulations showed that an isolated $B_{12}$ icosahedron was not stable [12], nor was the filled icosahedral $B_{13}^+$ cationic cluster [13], which was observed experimentally to have prominent abundance [4]. They were found to rearrange to lower symmetry three-dimensional (3D) structures. The first systematic structural optimisation was reported by Bonacic-Koutecky and co-workers on small neutral $B_n$ and cationic $B_n^+$ clusters for $n$ up to 8, which were all found to be planar or quasi-planar (2D) [14], including the highly symmetric $D_{7h}$ $B_8$ and $C_{7v}$ $B_8^+$ clusters. A subsequent study by Morokuma and co-workers on $B_n$ and $B_n^+$ up to $n = 12$ found planar cyclic structures for these clusters [15]. Theoretical calculations by Boustani using density functional theory (DFT) on $B_n$ for $n$ up to 14 showed that 2D structures were more stable than 3D isomers [16,17]. Calculations on $B_n^+$ and $B_nH^+$ for $n$ up to 13 by Ricca and Bauschlicher also found 2D structures [18,19]. Fowler and Ugalde first considered the reason for planarity for the $B_{13}^+$ cluster [20]. They found six $\pi$ electrons in the planar $B_{13}^+$ cluster and recognised 'a situation reminiscent of benzene and Huckel aromaticity'. The aromaticity of $B_{13}^+$ was bolstered by its large topological resonance energy subsequently reported by Aihara [21].

Since 2002, PES, in conjunction with theoretical calculations, has been used to probe the electronic structure and chemical bonding of size-selected boron clusters [11,22–28]. The structures and bonding of boron clusters with up to 27 atoms have been systematically elucidated and all found to have 2D global minimum structures [29–36]. Since size-selection by mass spectrometry requires charged clusters, negatively-charged boron clusters ($B_n^-$) have been the main focus in all global minimum searches. All 2D boron clusters consist of a periphery and one or more interior boron atoms. Chemical bonding analyses have found that all peripheral boron atoms are bonded by classical 2-centre–2-electron (2c–2e) bonds, whereas the interior atoms are bonded by delocalised bonds, as a result of boron's electron deficiency. There are both delocalised $\sigma$ and $\pi$ bonds in 2D boron clusters, giving rise to the concept of multiple aromaticity. The $\pi$ systems of the 2D boron clusters are found to obey the Huckel rule and analogy with polycyclic aromatic hydrocarbons (PAHs) has been found for most aromatic boron clusters [24,25]. The elucidation of the structures and bonding of 2D boron clusters has led to a design principle for metal-centred aromatic boron wheel clusters ($M©B_n^-$) [37]. A series of such borometallic molecular wheels have been produced and characterised [38–44], which are not included in this review.

In particular, the discovery of the planar hexagonal $B_{36}$ cluster and its implication for the viability of borophene [45] and the discovery of the first all-boron fullerene (borospherene) at $B_{40}$ [46] have stimulated considerable recent interests in boron clusters and nanostructures. An extensive review was published by Alexandrova *et al.* for the studies of boron clusters reported before 2005 [28]. Recently, a brief account of the unique bonding and structural characteristics of planar boron clusters has also appeared by Sergeeva *et al.* [47]. The current review will provide a more comprehensive account for the progress made over the past ten years, during which major advances have been made in the elucidation of the structures and bonding of medium-sized boron clusters by combining PES and extensive global minimum searches, culminated by the discovery of the first all-boron fullerene or borospherene [46].

The review is organised as follows. In the next section, the experimental details will be presented. Special attention will be paid to the advances for cluster temperature control that made it possible to obtain well-resolved photoelectron spectra for comparison with theoretical calculations. The main body of the review is divided into five sections. In Section 3, the small clusters covered by the previous review [28] will be briefly discussed. Earlier preliminary photoelectron data will be presented in this section, which essentially charted the road map for the subsequent progresses. Sections 4 and 5 present clusters from $B_{16}^-$ to $B_{20}^-$ and $B_{21}^-$ to $B_{27}^-$, respectively. The hexagonal $B_{36}$ cluster and the implication for borophene are discussed in Section 6, whereas the discovery of borospherene is presented in Section 7. The review is concluded with a brief summary and a few concluding remarks.

## 2. Experimental methods

### 2.1. *PES of size-selected clusters*

PES is one of the most powerful experimental techniques to probe the electronic structure of matter. PES using ultraviolet or visible light sources directly probes the valance electrons [48], which are responsible for the chemical bonds of a molecule. UV-PES of size-selected anions has been the most prominent technique to study the electronic structure and chemical bonding of size-selected clusters [49–59]. In particular, the magnetic-bottle PES technique with its high detection efficiency [60] has been very important in the investigation of atomic clusters [50,51]. A photoelectron spectrum can be viewed as an electronic fingerprint for the underlying cluster. A well-resolved photoelectron spectrum can be used to compare with theoretical calculations with proper global minimum searches to understand the structure and chemical bonding of the cluster. In particular, PES in combination with theoretical chemistry has played the most important role in advancing the understanding of the structures and bonding of boron clusters.

### 2.2. *The magnetic-bottle PES apparatus used for size-selected boron clusters*

The PES experiments on size-selected boron clusters have been carried out using a magnetic-bottle apparatus equipped with a laser vaporisation supersonic cluster source [61,62]. Figure 1 displays a schematic of the apparatus at Brown University. A

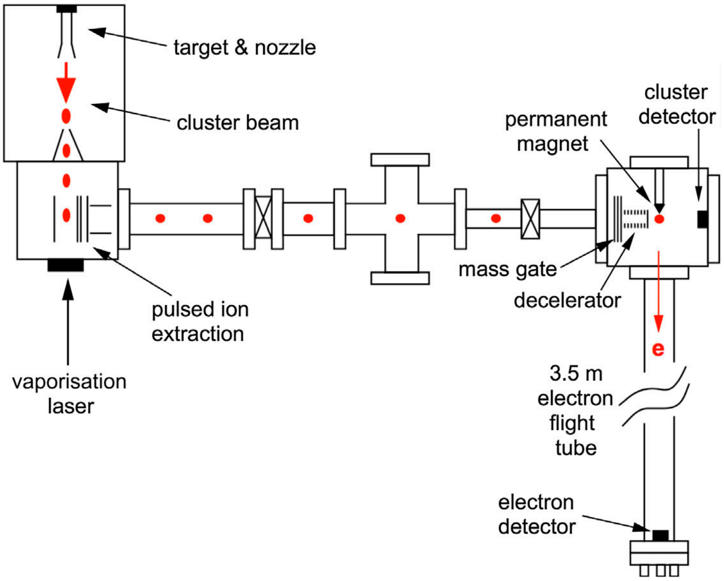

Figure 1. (Colour online) A schematic drawing of the magnetic-bottle PES apparatus equipped with a laser vaporisation supersonic cluster source. Key components are labelled. The red dots represent the trajectory of the clusters.

vaporisation laser beam (532 nm) is focused onto a boron target, made of a compressed disc usually from an isotopically-enriched $^{10}$B or $^{11}$B powder. The laser-induced plasma is quenched by a high-pressure helium carrier gas, cooling the plasma and initiating nucleation of the vaporised atoms to form clusters of various sizes. The nascent clusters formed in the nozzle are entrained by the carrier gas and undergo a supersonic expansion to create a cold cluster beam. After a skimmer, the negatively charged cluster ions from the collimated beam are extracted perpendicularly into a time-of-flight (TOF) spectrometer for mass analyses. Mass spectra of cluster distributions can be taken using the cluster detector at the end of the TOF tube. A typical mass spectrum for medium-sized boron cluster anions is shown in Figure 2, which was obtained with a $^{10}$B-enriched target. The bell-shaped distribution was a result of the perpendicular extraction geometry, such that only a narrow range of clusters could be directed onto the detector by a set of static electrical deflector. The cluster source conditions and the deflector voltage could be tuned to shift the cluster distribution. In general, smooth distributions are produced without the appearance of ‘magic’ numbers like that observed in carbon clusters [63,64]. The unusually low abundance of the $B_{12}^-$ peak was because neutral $B_{12}$ had a large energy gap between its highest occupied molecular orbital (HOMO) and lowest unoccupied molecular orbital (LUMO), which resulted in a very low electron affinity for the $B_{12}$ cluster [25].

The cluster of interest is selected by a mass gate and decelerated before being detached by a laser beam in the interaction zone of the magnetic-bottle electron analyser. Photoelectrons are collected by the magnetic bottle at nearly 100% collecting efficiency and detected at the end of a 3.5 metre long electron TOF tube. The experiment is run at 10 Hz repetition rate, while the detachment laser is run at 20 Hz to provide a background electron signal for shot-to-shot background subtraction. The

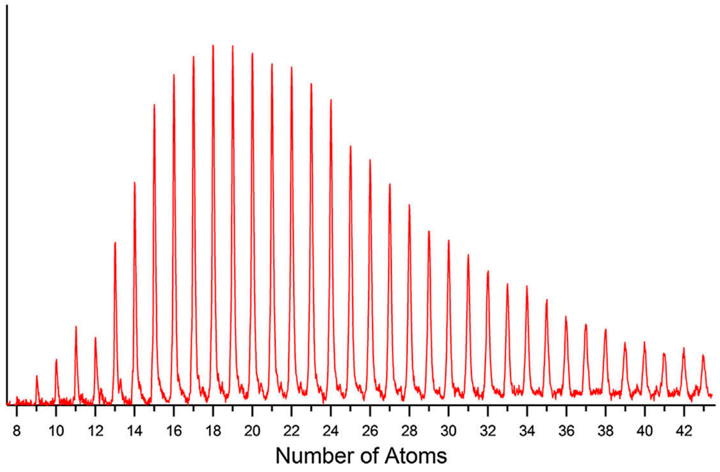

Figure 2. (Colour online) A representative mass spectrum of $B_n^-$ cluster anions ($n = 8-43$) from the laser vaporisation of a hot-pressed boron disc target made of $^{10}$B-enriched power.

photoelectron TOF spectrum is converted into an electron kinetic energy distribution calibrated by the known spectra of atomic anions, usually $Cu^-$ or $Au^-$. Both a Nd: YAG laser (355, 532, and 266 nm) and an excimer laser (193 nm from ArF) have been used for PES of size-selected boron clusters. The background subtraction is important at 266 nm or shorter wavelengths. Figure 3 displays a set of spectra for $Cu^-$ at three photon energies. The detachment features from the 4s orbital and the spin-orbit-split 3d orbitals provide three convenient transitions for calibration. Interestingly, a strong shakeup transition was also observed for $Cu^-$ at 193 nm, due to the detachment of a 4s electron and simultaneous excitation of a 4s electron to the 4p orbital ($4s^{-1}4p^{+1}$) [65]. The electron kinetic energy resolution of the magnetic-bottle PES analyser is about 2.5% (ΔEk/Ek), i.e. ~25 meV for 1 eV electrons. Better resolution is achieved for low-lying detachment transitions by using low photon energies, as shown for the $Cu^-$ spectrum at 355 nm in Figure 3, whereas high photon energies allow high binding energy transitions to be observed.

### 2.3. *The large waiting room nozzle and cluster temperature control*

To obtain well-resolved photoelectron spectra for size-selected clusters requires both good instrumental resolution and more importantly cold clusters. Even though it has been possible recently to actively cool cluster ions in cryogenic ion traps for PES studies [66–68], it is generally quite challenging to produce cold clusters using the laser vaporisation supersonic cluster source. Because of their large heat of formation, nascent boron clusters formed in the nozzle can carry enormous amounts of internal energies, which may not be effectively removed during the supersonic expansion. We have found that a large waiting room nozzle [61,69] could produce relatively cold cluster anions, allowing us to qualitatively control the cluster temperatures to yield well-resolved photoelectron spectra [70,71].

Figure 4 shows a cross sectional view of our large waiting room nozzle assembly, including the double Jordan valve (R. M. Jordan Co., Grass Valley, CA) and the target

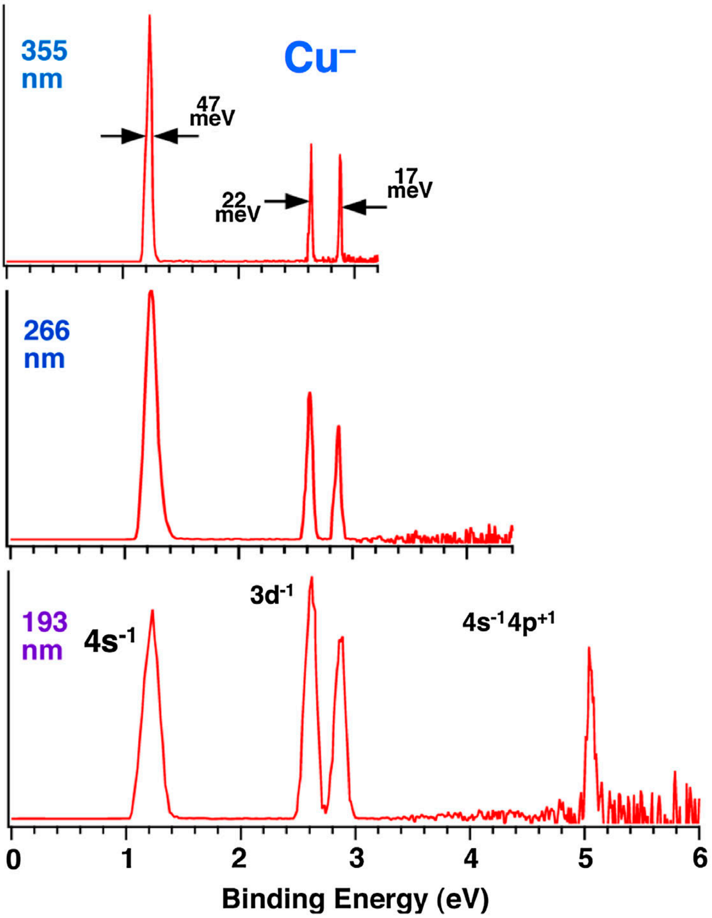

Figure 3. (Colour online) Photoelectron spectra of $Cu^-$ at three photon energies, used as calibrations. The spectral widths are labelled in the 355 nm spectrum, representing the best resolution achieved. The detachment channels are labelled in the 193 nm spectrum. Note the peak at 5 eV is due to a two-electron transition: detachment of a 4s electron and simultaneous excitation of another 4s electron to the 4p orbital [65].

assembly. In this nozzle, the cluster growth takes place in the volume of the so-called waiting room, followed by supersonic expansion via a 2 mm diameter orifice. During our studies of $Al_n^-$ clusters [70], we discovered that clusters, which stayed longer in the waiting room, gave rise to substantially better resolved spectra than those clusters, which left the waiting room earlier, as shown in Figure 5 for $Al_{13}^-$, $Al_{17}^-$, and $Al_{66}^-$. Figure 6 shows the time evolution of the helium carrier gas pressure inside the nozzle and the cluster distribution following the firing of the vaporisation laser [71]. The three arrows represent the positions where the hot, warm, and cold spectra were taken in Figure 5. Even though the abundance of clusters with long residence time was low, the clusters were colder and yielded significantly better resolved spectra. Molecular dynamics simulations showed that the cold clusters had vibrational temperatures as low as 130 K [72], while the nozzle was operated at room temperature. Apparently, the longer

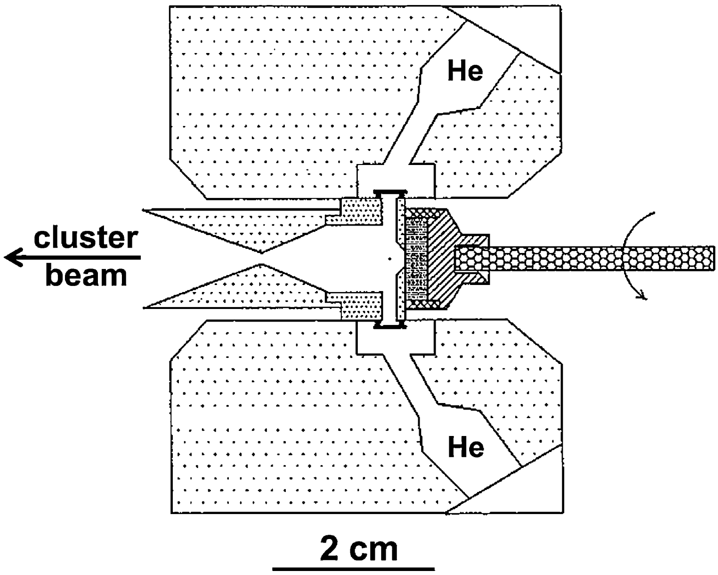

Figure 4. A schematic drawing of the large waiting-room nozzle [61]. The bar in the bottom represents the scale. The two pulsed helium valves and the target rotation are indicated.

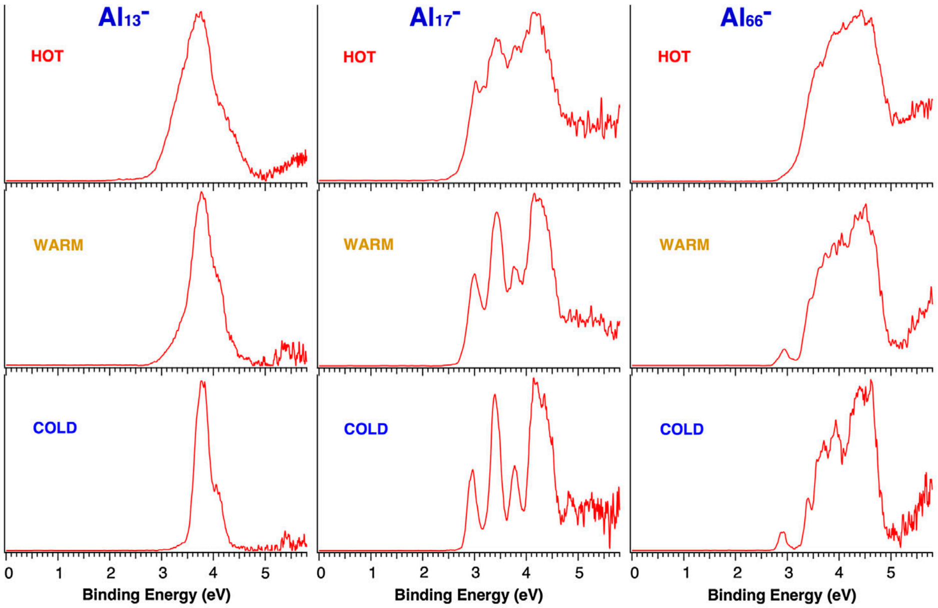

Figure 5. (Colour online) Photoelectron spectra of $Al_{13}^-$, $Al_{17}^-$, and $Al_{66}^-$ at 193 nm and three different temperatures. See Figure 6 for the timing, where the 'hot', 'warm', and 'cold' spectra were taken. In general, clusters leaving the nozzle earlier are hotter and those leaving the nozzle later are colder [71].

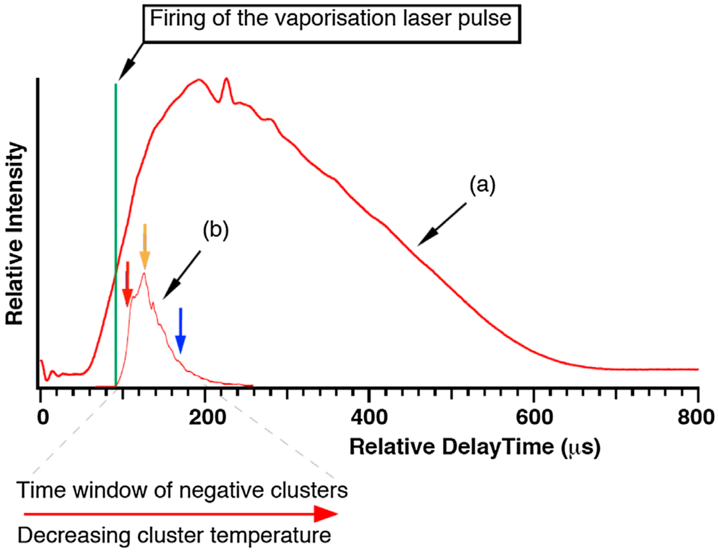

Figure 6. (a) The He carrier gas pressure profile in the large waiting-room nozzle following the opening of the pulsed valves, measured about 5 cm down stream from the nozzle exit with a fast ion gauge (see Figures 1 and 4). The peak pressure in the nozzle was estimated to be about one atmosphere with a ten-atmosphere backing pressure in the pulsed valves. The vertical green line indicates the firing of the vaporisation laser. (b) A typical intensity profile of cluster anions inside the nozzle as a function of time following the firing of the vaporisation laser. The arrows indicate where the spectra in Figure 5 were taken [71].

residence time of the clusters in the nozzle helped thermalise the hot nascent clusters to allow the subsequent supersonic expansion to cool the clusters to be substantially below room temperature. The recent detection of van der Waals complexes of gold cluster anions with argon provided further evidence of the cooling capability of the large waiting room nozzle [73–76].

Because of the strong B−B bonding, it was expected that the heats of formation of boron clusters would be huge, making it more difficult to produce cold boron clusters. Indeed, we had difficulties initially to obtain photoelectron spectra with any resolved features for large boron clusters because of insufficient thermalisation. Figure 7 shows the spectra of $B_{20}^-$ at two photon energies and two different residence times in the nozzle. The large waiting room nozzle with tunable residence times was essential for us to obtain well-resolved photoelectron spectra for size-selected boron clusters, making it possible for effective comparison with theoretical calculations.

## 3. Structures of small boron clusters and PES of medium-sized boron clusters

Boron clusters containing three to 15 atoms were reviewed comprehensively in 2006 by Alexandrova *et al.* [28]. This size range is included here for completeness. Experimental progresses have been made in probing the structures of several cationic and neutral clusters in this size range [77,78], as well as further theoretical studies and bonding analyses [79–83]. A systematic bonding analysis for clusters in this size range was published in 2006 by Zubarev and Boldyrev [84]. Subsequently these authors have

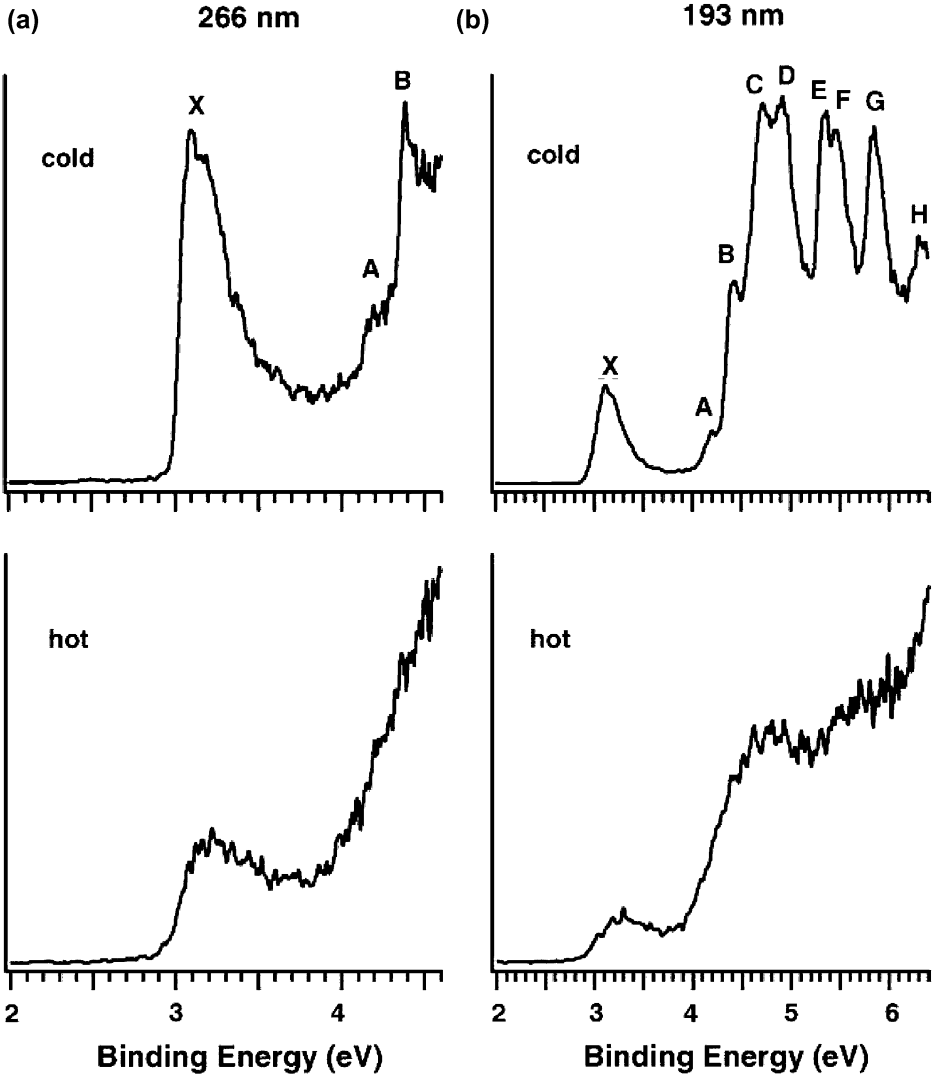

Figure 7. Photoelectron spectra of $B_{20}^-$ at 266 nm (a) and 193 nm (b) and two different temperatures. The cold spectra were taken for clusters with longer resident time in the nozzle. See Figure 6.

developed the adaptive natural density partitioning (AdNDP) method as a new paradigm for chemical bonding [85], which is particularly suitable for 2D boron clusters and has contributed substantially to our understanding of the bonding in these complex systems.

### 3.1. *The structures of small boron clusters from $B_3^-$ to $B_{15}^-$*

Figure 8 summarises the global minimum structures of $B_n^-$ for $n = 3$ to 27. Clusters beyond $B_{15}^-$ will be discussed in the following Sections. Isomers have been observed for some clusters, but only those for the two largest clusters ($B_{25}^-$ and $B_{27}^-$) in this size range are included in Figure 8 [35,36]. In particular, a new isomer has been found for $B_9^-$ [79], which was present in the original photoelectron spectra (see Figure 9(b)), but not initially recognised. The global minimum of $B_9^-$ was found to be a beautiful $D_{8h}$ molecular wheel in the original study [24]. Global minimum searches at B3LYP level showed that the nearest isomer was about 23 kcal/mol higher in energy. Thus, the weak features observed in the photoelectron spectra were thought not to be due to low-lying isomers, even though they were not satisfactorily accounted for by the $D_{8h}$ global minimum. Pan *et al.* did extensive theoretical calculations using seven theoretical methods with three different basis sets and found that the B3LYP method underestimated the

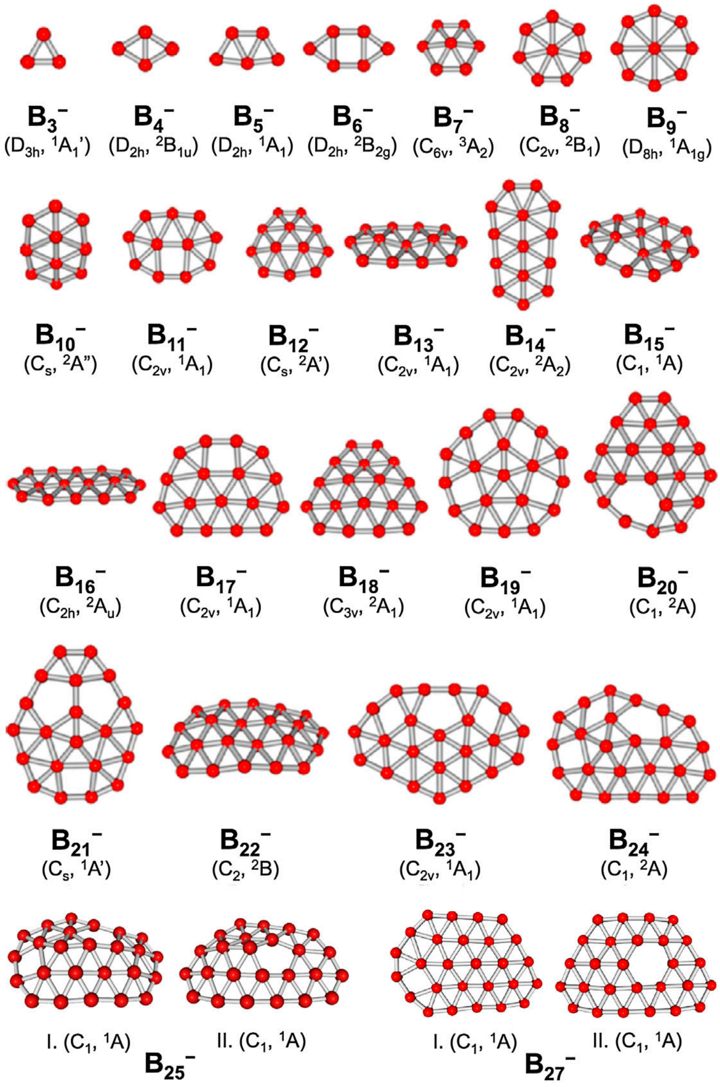

Figure 8. (Colour online) A summary of the global minima of $B_n^-$ clusters ($n = 3-25$, 27) confirmed by experiment. Note that a close-lying isomer is also shown for $B_{25}^-$ and $B_{27}^-$.

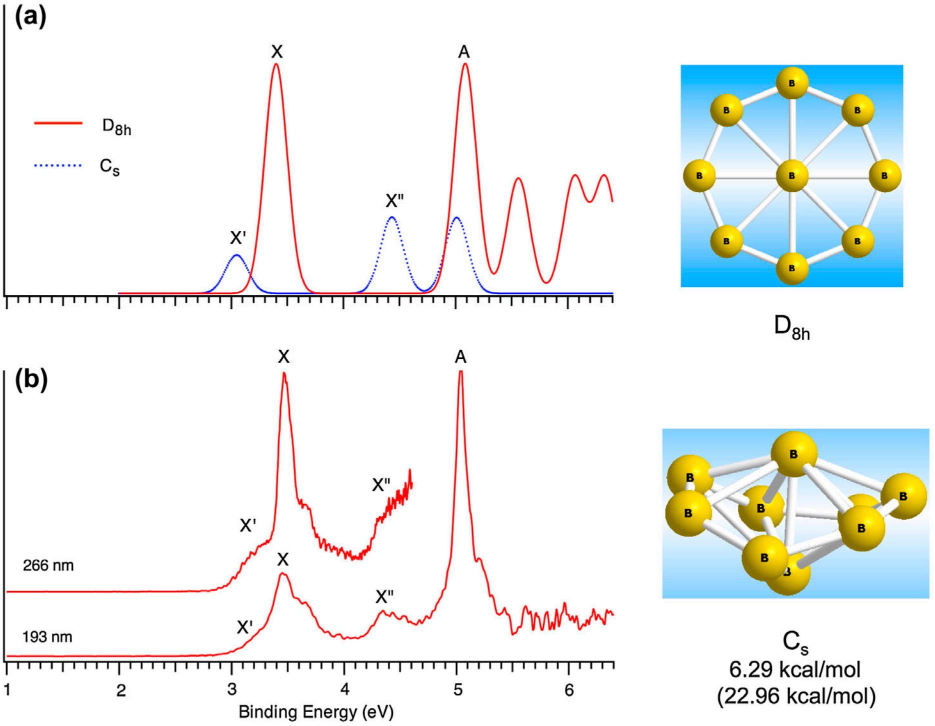

Figure 9. (Colour online) The simulated spectra of the global minimum ($D_{8h}$) of $B_9^-$ and a low-lying isomer ($C_s$) (a), compared with the experimental photoelectron spectra of $B_9^-$ at two photon energies (b). The structures of the global minimum and the $C_s$ isomer are shown, as well as the relative energies of the $C_s$ isomer above the global minimum at CCSD(T) and B3LYP (in parentheses) levels of theory [79].

stability of the 3D isomers [79]. At the CCSD(T) level of theory, it was found that a 3D structure ($C_s$, Figure 9) was only 6.29 kcal/mol higher than the global minimum $D_{8h}$ structure. If the finite temperature effect was taken into account, the free energy of the 3D isomer was only about 3 kcal/mol above the $D_{8h}$ structure, making it quite plausible to be accessed experimentally. More importantly, the simulated spectrum of the 3D isomer (Figure 9(a)) was in excellent agreement with the weak features in the experimental spectra.

Some of the 2D structures shown in Figure 8 are quasi-planar. For example, both $B_7^-$ and $B_{12}^-$ were found to have bowl-shaped structures [25,26], even though both were aromatic. The out-of-plane distortion was found to be due to the fact that the peripheral B−B bonds were stronger with slightly shorter bond lengths and could squeeze out the interior atoms slightly. This observation was confirmed by substituting a peripheral B atom by a larger valence-isoelectronic Al atom and the resulting $AlB_6^-$ and $AlB_{11}^-$ clusters were found to be planar [86]. It was also found that the larger Al atom did not favour the interior of 2D boron clusters. In a series of Al-doped boron clusters ($AlB_n^-$, $n = 8-10$), umbrella-type structures were found [87,88]. The putative $Al@B_n^-$ wheel-type structures [89] were found to be high energy isomers and were not observed experimentally. It was further found that the carbon atom also preferred the peripheral sites in C-doped planar boron clusters [90–94]. In Au-doped boron clusters ($AuB_n^-$), the Au atom was found to bond to the periphery of the planar clusters akin to a hydrogen atom [95–97].

Neutral boron clusters are considerably more challenging to study. The infrared (IR) spectrum of neutral $B_{11}$ was obtained using an IR/UV two colour ionisation scheme in the wavelength range from 650 to 1550 $cm^{-1}$ [78]. It was found that the global minimum of neutral $B_{11}$ ($C_{2v}$, $^2B_2$) is nearly identical to that of the $B_{11}^-$ anion (Figure 8) [25]. A more significant experimental study was carried out by Oger *et al.* to probe the $B_n^+$ cation structures for $n = 12-25$ using ion mobility in combination with DFT calculations [77]. The structures of $B_{12}^+$ and $B_{15}^+$ were found to be similar to those of the corresponding anions (Figure 8), whereas the structures of $B_{13}^+$ and $B_{14}^+$ were found to be more circular, consistent with previous calculations [18]. It should be mentioned that Cheng found a compact 3D isomer for $B_{14}$ and showed that it was more stable than several planar structures using *ab initio* calculations [81]. However, this result has not been confirmed experimentally and the 3D structure was not even a low-lying isomer for either $B_{14}^-$ or $B_{14}^+$ [25,77].

### 3.2. *Deciphering the chemical bonds of boron clusters using AdNDP*

The chemical bonding of the planar boron clusters is very interesting, but highly complex due to both localised and delocalised bonds, owing to boron's electron deficiency. For smaller clusters with high symmetries, the canonical molecular orbitals (MOs) can be used directly to deduce essential chemical bonding information. MOs are eigenvectors of the model Hamiltonian and they are completely delocalised over the molecule. Hence, for large and low-symmetry boron clusters, the MOs are no longer sufficient to decipher their chemical bonding. The AdNDP method developed by Zubarev and Boldyrev provides the most chemically intuitive pictures of the chemical bonds for boron clusters [47,85], as well as PAH molecules and planar nanostructures [98–100].

The AdNDP method is a generalisation of the natural bonding orbital analysis [101] and is based on the concept of electron pairs as the main elements of chemical bonds. It combines the compactness and intuitive simplicity of the Lewis structures with the MO theory and represents the molecular electronic structure in terms of *n*-centre two-electron (*n*c–2e) bonds, recovering the familiar lone pairs (1c–2e) and localised 2c–2e bonds familiar in the Lewis model or delocalised *n*c–2e bonds ($3 \leq n \leq$ total number of atoms in the system). In AdNDP, charge density is partitioned into elements with the highest degree of localisation of electron pairs. If some part of the density cannot be localised, it is left delocalised (or localised on the maximum number of available centres). AdNDP can result in completely delocalised bonding, which is directly related to aromaticity. Hence, AdNDP achieves seamless description of chemical bonding even for very complicated molecular systems, connecting MO theory with the familiar and more intuitive Lewis model.

Figure 10 shows an AdNDP analysis for the bonding in the $D_{8h}$ $B_9^-$ cluster [85]. Previous MO analysis showed that, among the fourteen fully occupied MOs, eight are responsible for the peripheral bonding, three $\sigma$ and three $\pi$ MOs are responsible for bonding between the central atom and the periphery [24]. Figure 10 shows clearly eight localised 2c–2e peripheral B–B bonds, and three totally delocalised (9c–2e) $\sigma$ and $\pi$ bonds, which give rise to the concept of multiple aromaticity. The understanding of the bonding and stability of the $D_{8h}$ $B_9^-$ cluster directly led to the design principle for the

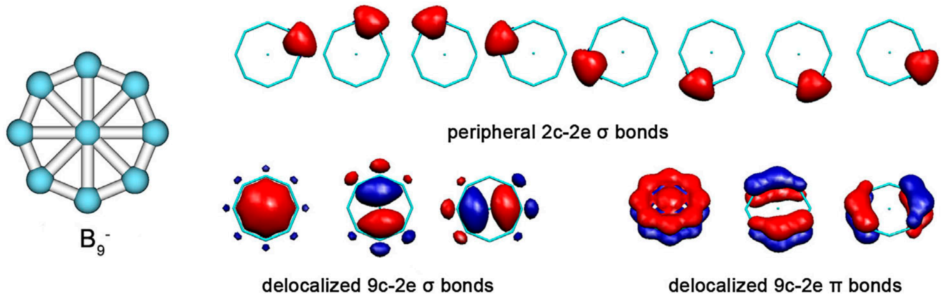

Figure 10. AdNDP analyses of the bonding in the $D_{8h}$ global minimum of the $B_9^-$ cluster [85].

borometallic $M©B_n^-$ type molecular wheels [37–44]. Indeed, the AdNDP approach has been essential to analyse the bonding in large boron clusters, which will become clear in the rest of the review.

### 3.3. *Preliminary PES of medium-sized boron clusters and the challenge of global minimum searches*

Because of the enormous challenges of global minimum searches, progress was very slow in solving the structures of boron clusters beyond 15 atoms, except $B_{20}^-$ [27], which will be discussed in the next Section. Preliminary photoelectron data were obtained for $B_n^-$ up to $n = 42$ around 2005. Figure 11 displays a manual plot made by the author in 2005, displaying the trend of the estimated first adiabatic electron detachment energies (ADEs) of $B_n^-$ or the electron affinity (EA) of the corresponding neutral $B_n$ clusters as a function of cluster size from $n = 3-42$. To this day, not all clusters in this size range have been solved. Precise EAs and the first vertical electron detachment energies (VDEs) for those clusters that have been published are given in Table 1. The EAs in Figure 11 are approximate values for $n = 16-19$ and $21-42$ estimated from the preliminary PES data. But they are in general within the uncertainties of the subsequently reported values listed in Table 1. A clear odd-even alternation was observed for $n > 8$, indicating that all odd-sized $B_n^-$ anions are closed shell and the even-sized $B_n$ neutral clusters are closed shell.

A pressing issue at the time was to find the 2D to 3D transition. Because of the computational challenges for global minimum searches, an attempt was made to collaborate with the Kappes' group to use ion mobility, which might yield direct information about the structural transition. Ion mobility experiments [102] could give rise to cross section information of size-selected clusters. Because the 2D and 3D clusters were expected to have very different cross sections, ion mobility data in principle could identify the size for the 2D–3D transition straightforwardly, as was reported for small $Au_n^-$ clusters by the Kappes group [103]. However, due to experimental challenges to perform ion mobility measurements for $B_n^-$ anions, only $B_n^+$ cations were studied in the size range of $n = 12-25$ [77]. Hence, we still had to resort to the combination of PES and computational chemistry to slowly solve structures for $n > 15$. The manual plot of Figure 11 essentially served as a road map for future progresses. Specifically, note was taken for the two unusual data points at $n = 36$ and 40, that foresaw future discoveries

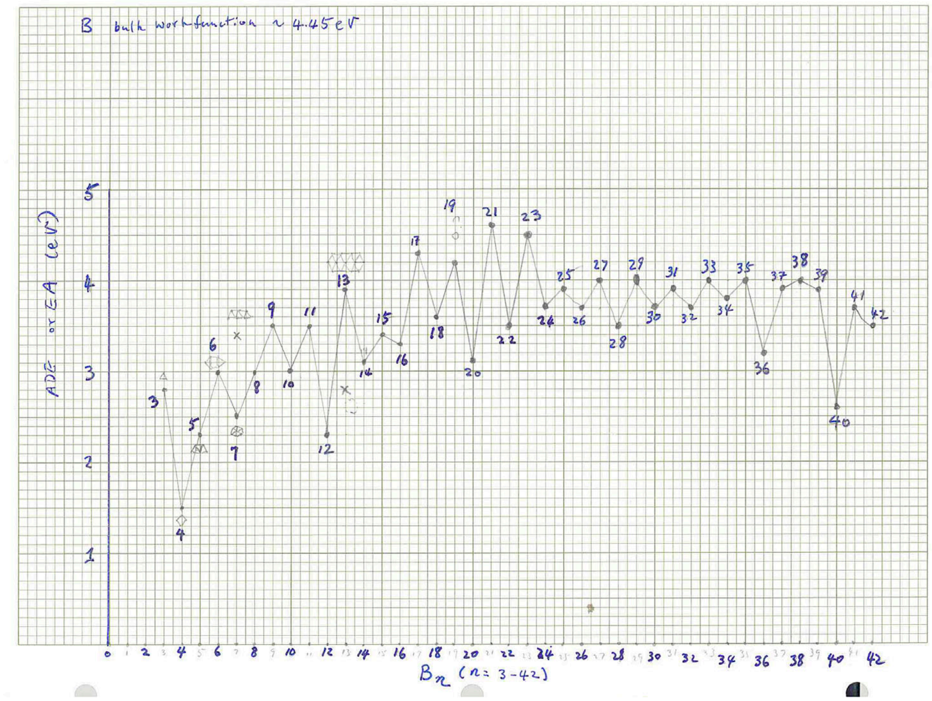

Figure 11. (Colour online) A preliminary plot of the electron affinity (EA) of $B_n$ ($n = 3{-}42$) made in 2005. See Table 1 for the precise EA values for those clusters, for which photoelectron spectra have been published.

Table 1. Measured first adiabatic detachment energy (ADE) and the first vertical detachment energy (VDE1) of boron clusters ($B_n^-$) and their known low-lying isomers.[a]

| Cluster | ADE | VDE1 | Ref. | Cluster | ADE | VDE1 | Ref. |
|---|---|---|---|---|---|---|---|
| $B_3^-$ | 2.82(2) | 2.82(2) | [23] | $B_{17}^-$ | 4.23(2) | 4.48(5) | [31] |
| $B_4^-$ | ~1.6 | 1.99(5) | [23] | $B_{18}^-$ | 3.53(5) | 3.71(5) | [31] |
| $B_5^-$ | 2.33(2) | 2.40(2) | [11] | $B_{19}^-$ | 4.2(1) | 4.34(4) | [30] |
| $B_6^-$ | 3.01(4) | 3.01(4) | [22] | $B_{20}^-$ | 3.02(2) | 3.11(2) | [27] |
| $B_7^-$ ($C_{6v}$) | 2.55(5) | 2.85(5) | [26] | $B_{21}^-$ | 4.38(5) | 4.58(4) | [32] |
| $B_7^-$ ($C_{2v}$) | 3.44(2) | 3.44(2) | [26] | $B_{22}^-$ | 3.34(5) | 3.48(5) | [33] |
| $B_8^-$ | 3.02(2) | 3.02(2) | [24] | $B_{23}^-$ | 4.32(5) | 4.46(3) | [33] |
| $B_9^-$ ($D_{8h}$) | 3.39(6) | 3.46(6) | [24] | $B_{24}^-$ | 3.55(7) | 3.75(7) | [34] |
| $B_9^-$ ($C_s$) | ~3.1 | ~3.2 | [79] | $B_{25}^-$ | 3.8(1) | 4.02(6) | [35] |
| $B_{10}^-$ | 2.88(9) | 3.06(3) | [25] | | | | |
| $B_{11}^-$ | 3.426(10) | 3.426(10) | [25] | $B_{27}^-$ | 3.9(1) | 4.09(6) | [36] |
| $B_{12}^-$ | 2.21(4) | 2.26(4) | [25] | $B_{30}^-$ | 3.59(7) | 3.69(7) | [130] |
| $B_{13}^-$ ($C_s$) | 3.78(2) | 3.78(2) | [25] | $B_{35}^-$ | 3.96(5) | 4.06(5) | [131] |
| $B_{13}^-$ ($C_{2v}$) | 2.70(4) | 2.80(4) | [25] | $B_{36}^-$ | 3.12(3) | 3.3(1) | [45] |
| $B_{14}^-$ | 3.102(10) | 3.102(10) | [25] | $B_{39}^-$ | 3.84(5) | 4.00(5) | [132] |
| $B_{15}^-$ | 3.34(4) | 3.43(4) | [25] | $B_{40}^-$ ($D_{2d}$) | 2.50(5) | 2.62(5) | [46] |
| $B_{16}^-$ | 3.25(5) | 3.39(4) | [29] | $B_{40}^-$ ($C_s$) | 3.51(5) | 3.63(5) | [46] |

[a] All energies are in eV. The ADE also represents the electron affinity of the corresponding neutral clusters. The numbers in the parentheses indicate the uncertainty in the last digit.

for borophenes [45] and borospherenes [46]. With increasing powers in computational hardware and software, much faster progress has been possible since 2011.

## 4. Structures of boron clusters from $B_{16}^-$ to $B_{20}^-$

### 4.1. *$B_{16}^-$: an all-boron naphthalene*

Beyond $B_{15}^-$, it took five years before the structure of the next cluster of $B_{16}^-$ was solved by Sergeeva *et al.* [29], due to the above-mentioned challenges of global minimum searches and the demand on computational resources. The photoelectron spectra of $B_{16}^-$ at two photon energies are shown in Figure 12 with well-resolved spectral features and a relatively broad ground state transition (X). Global minimum searches were done using the gradient embedded genetic algorithm [104,105] at the B3LYP level of theory. The global minimum of $B_{16}^-$ was found to be an elongated quasi-planar structure with $C_{2h}$ symmetry (I.1 in Figure 13). At the CCSD(T) level, the $C_{2h}$ global minimum was more stable than the first low-lying isomer, which was also 2D, by 3.7 kcal/mol. The calculated VDEs from the $C_{2h}$ global minimum, given as vertical bars in Figure 12(b), agreed well with the observed photoelectron spectral pattern, providing considerable credence to the determined global minimum.

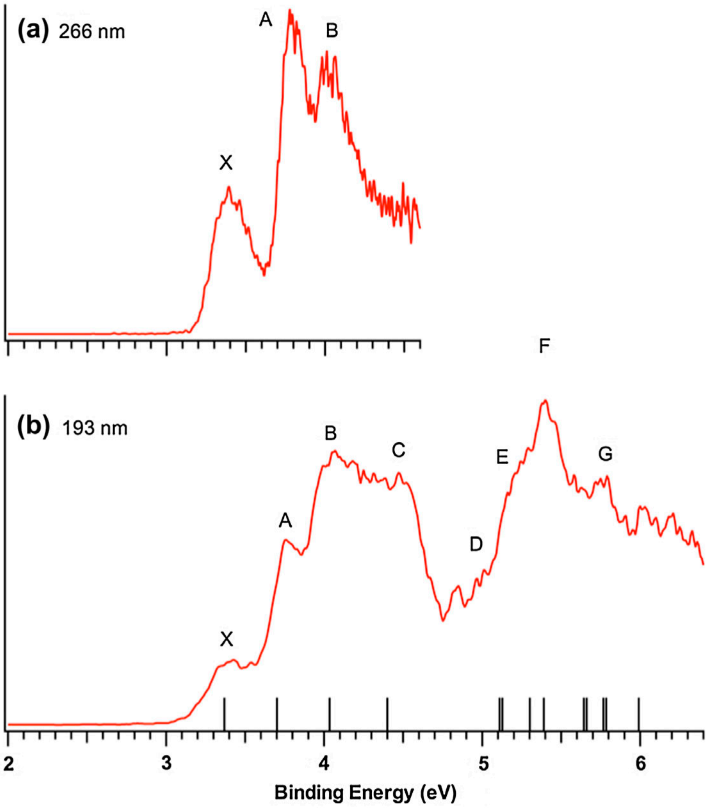

Figure 12. (Colour online) Photoelectron spectra of $B_{16}^-$ at 266 nm (a) and 193 nm (b) [29]. The vertical bars represent the calculated VDEs from the global minimum of $B_{16}^-$ (see Figure 13).

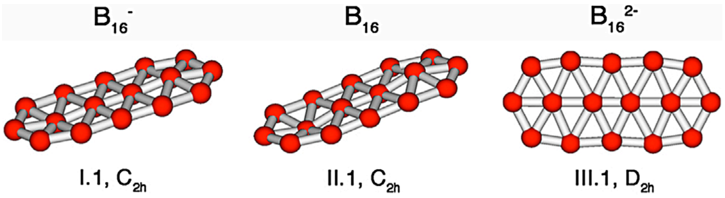

Figure 13. (Colour online) The global minimum structures of $B_{16}^{-}$ ($^2A_u$), $B_{16}$ ($^1A_g$), and $B_{16}^{2-}$ ($^1A_g$) [29].

The global minimum of $B_{16}^{-}$ (I.1 in Figure 13) was quasi-planar because the four inner B atoms displayed a zigzag pattern with an out-of-plane distortion of 0.08 Å. The global minimum of $B_{16}$ was found to be similar to that of $B_{16}^{-}$, but with more severe out-of-plane distortions by 0.24 Å (II.1 in Figure 13), consistent with the broad ground state transition in the photoelectron spectrum. The IR spectrum of neutral $B_{16}$ was obtained and confirmed the $C_{2h}$ global minimum [78]. The global minimum of $B_{16}^{-}$ was open-shell with a doublet electronic state ($C_{2h}$, $^2A_u$). It was found that addition of an electron to $B_{16}^{-}$ resulted in a perfect planar and closed-shell $B_{16}^{2-}$ dianion ($D_{2h}$, $^1A_g$) (see III.1 in Figure 13).

MO analyses showed that the $D_{2h}$ $B_{16}^{2-}$ dianion possessed ten $\pi$ electrons, analogous to the well-known aromatic naphthalene, as compared in Figure 14. Thus, $B_{16}^{2-}$ was considered to be an 'all-boron naphthalene' [29]. Removal of two electrons from the HOMO of $B_{16}^{2-}$ led to an $B_{16}$ species with eight $\pi$ electrons, i.e. an anti-aromatic system, which explained the out-of-plane distortions in $B_{16}$. AdNDP analyses found twelve localised 2c–2e peripheral B−B $\sigma$ bonds, two 4c–2e $\sigma$ bonds at the two ends of the cluster, and six 3c–2e $\sigma$ bonds in the interior of the planar $B_{16}^{2-}$ cluster.

A double ring isomer for $B_{16}^{-}$ was found to be 36 kcal/mol above the $C_{2h}$ global minimum, but for neutral $B_{16}$ the double ring isomer was found to be 14 kcal/mol at the B3LYP level of theory [78]. The IR spectrum of $B_{16}$ also ruled out the presence of the double ring isomer, consistent with the fact that it was a much higher-lying isomer. However, calculations for $B_{16}^{+}$ showed that a $C_{2v}$ 3D structure was competing with the $C_{2h}$ structure for the global minimum [77,82]. This $C_{2v}$ 3D isomer was also found to be a low-lying isomer for neutral $B_{16}$ and could contribute to the observed IR spectrum of $B_{16}$ as a minor component [78]. On the other hand, the double ring isomer for the cationic $B_{16}^{+}$ became much lower in energy, only 2.3 kcal/mol at the TPSS level of

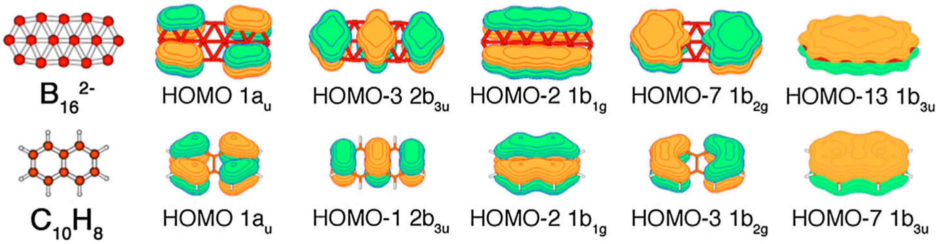

Figure 14. (Colour online) Comparison of the occupied $\pi$ MOs of $B_{16}^{2-}$ with those of naphthalene [29].

theory [77] and 3.9 kcal/mol at the CCSD(T) level of theory [82], above the global minimum. Nevertheless, the calculated cross section of the double ring $B_{16}^+$ was concluded to be in better agreement with the ion mobility experiment. In fact, all $B_n^+$ clusters above $B_{16}^+$ that were measured by ion mobility up to $n = 25$ were concluded to have the double ring structure, including the odd-sized $B_n^+$ clusters in this size range [77]. Hence, the 2D-to-3D transition for cationic boron clusters has been concluded to occur at $B_{16}^+$. However, the double ring structures for boron clusters remain enigmatic and the conundrum will be discussed in the context of the $B_{20}^-$ cluster in Section 4.4 (*vide infra*).

### 4.2. $B_{19}^-$: *a doubly aromatic Wankel motor*

Two years elapsed before the next boron cluster, $B_{19}^-$, was solved by Huang *et al.* [30] using two different global minimum search methods, coalescence kick [106] and basin hopping [107]. The photoelectron spectra of $B_{19}^-$ at two photon energies are shown in Figure 15 with rather high binding energies. The global minimum was found to be a 'spider-web' structure (I in Figure 16), which is almost perfectly circular with one boron atom at the centre surrounded by five boron atoms and an outer ring of thirteen atoms. Another planar isomer with a triangular $B_6$ in the centre (II in Figure 16) was found to be quite low-lying, 1.75 kcal/mol at B3LYP and 3.73 kcal/mol at CCSD(T)

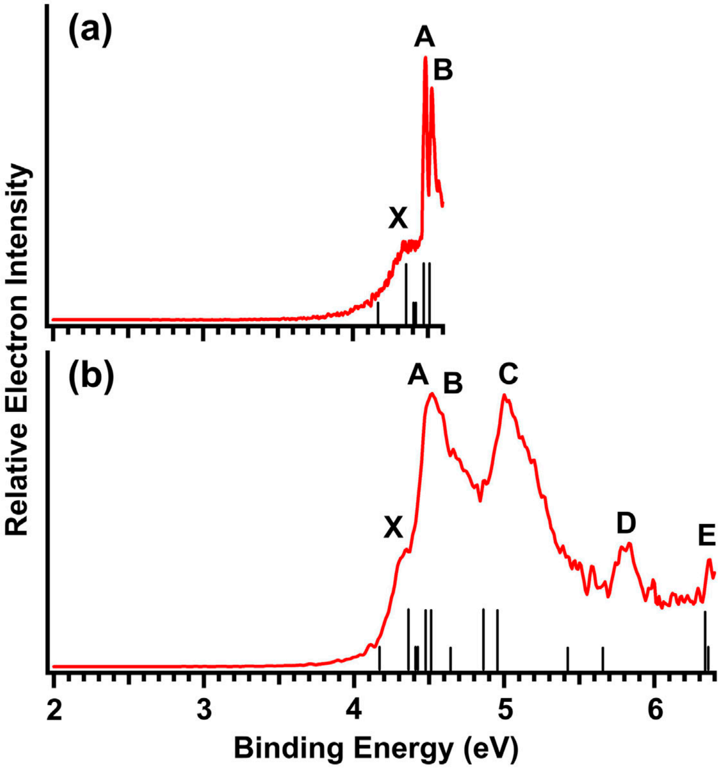

Figure 15. (Colour online) Photoelectron spectra of $B_{19}^-$ at 266 nm (a) and 193 nm (b) [30]. The long vertical bars represent the calculated VDEs from the global minimum of $B_{19}^-$ (see I Figure 16) and the short vertical bars represent the calculated VDEs from a low-lying isomer (see II in Figure 16).

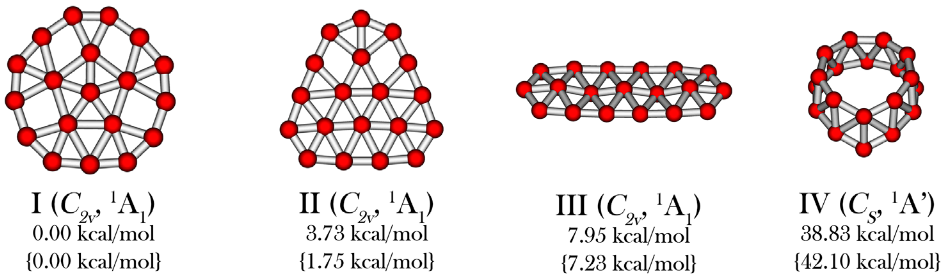

Figure 16. (Colour online) The global minimum and three higher energy isomers of $B_{19}^-$. The relative energies of the higher energy isomers are given at the CCSD(T) and B3LYP (in curly brackets) levels of theory [30].

level of theory above the global minimum. The calculated VDEs from the global minimum (long vertical bars in Figure 15) agreed well with the main PES features, whereas the calculated VDEs from the low-lying isomer (short vertical bars in Figure 15) could not be ruled out as a minor contributor. The double ring structure, which was found to be the global minimum for $B_{19}^+$ previously [77], was a much higher energy isomer for $B_{19}^-$ (IV in Figure 16).

MO analyses for the global minimum of $B_{19}^-$ (Figure 17(b)) showed similarity of its $\pi$ bonding with that in the [10]annulene molecule (Figure 17(a)), except that $B_{19}^-$ has one extra $\pi$ MO. Close examination found that a linear combination of the HOMO and HOMO-15 would generate one MO delocalised between the $B_5$ ring and the outer ring and another MO delocalised over the inner filled pentagon. Hence, $B_{19}^-$ consisted of two concentric delocalised $\pi$ systems: one between the $B_5$ ring and the outer $B_{13}$ ring

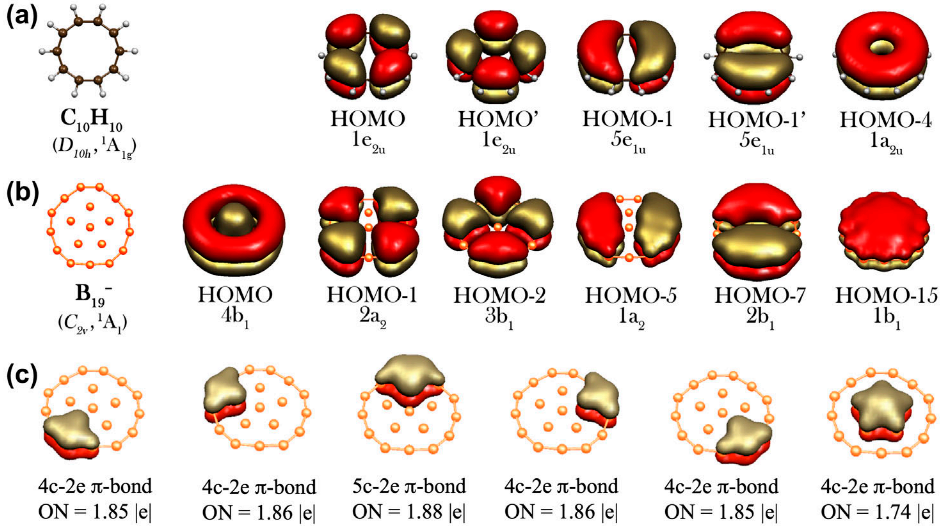

Figure 17. (Colour online) Comparison of the $\pi$ MOs of [10]annulene (a) with those of the global minimum of $B_{19}^-$ (b). (c) AdNDP analyses of the $\pi$ bonding in $B_{19}^-$, showing five $\pi$ bonds are delocalised between the inner $B_5$ ring and the outer $B_{13}$ ring similar to those in [10]annulene and one $\pi$ bond delocalized over the inner filled pentagon [30].

with five π MOs, which were analogous to the π system in the [10] annulene, and another single π MO delocalised over the central filled pentagon. The AdNDP analyses showed more clearly the two π systems, as seen in Figure 17(c). Thus, the $B_{19}^-$ cluster was considered to be a concentric doubly π aromatic species.

The low-lying isomer II of $B_{19}^-$ (Figure 16), which could have made minor contributions to the observed photoelectron spectra, was also found to be doubly π aromatic with a similar concentric π system as isomer I. The key structural difference between the two isomers was the arrangement of the central $B_6$ unit. In the global minimum isomer I, the $B_6$ unit was a filled pentagon with near $D_{5h}$ symmetry, resulting in its near circular structure, whereas in isomer II the $B_6$ unit formed a triangle, giving rise to the overall triangular shape of this isomer. AdNDP analyses showed that the σ bonding patterns in the two isomers were similar, but the π bonding patterns were slightly different [30]. It was speculated that the less delocalised π bonding in isomer II made it slightly less stable. Such subtle differences in the two isomers would demand theoretical methods that can take into account well the electron correlation effects.

A subsequent DFT calculation using LDA found that isomer II was the global minimum for $B_{19}^-$, whereas the perfectly round spider-web structure was 0.15 eV higher in energy [108]. Clearly, DFT overestimated the stability of isomer II, as was also shown at the B3LYP level of theory (Figure 16). Merino and co-workers found a 22.7 kcal/mol barrier from isomer I to II of $B_{19}^-$ at B3LYP level of theory [109]. Remarkably, using MD simulations they found that the inner filled pentagon in the $B_{19}^-$ global minimum could freely rotate at finite temperatures against the outer $B_{13}$ ring and proposed $B_{19}^-$ as a molecular Wankel motor. They further found that substituting one peripheral boron atom by a carbon atom significantly increased the rotational barrier and would halt the $B_{19}^-$ Wankel motor [110]. Similar analyses of the planar $B_{13}^+$ cluster also found that its inner $B_3$ triangle could rotate relative to the $B_{10}$ outer ring with a relatively small barrier [111]. It was even suggested that the rotational direction might be controlled using circularly polarised IR radiation [112]. By inserting a boron atom into the interior of the $B_{19}^-$ cluster, Tai *et al.* obtained a planar $B_{20}^{2-}$ cluster with a central filled hexagon and showed that it has similar π bonding and fluxionality as the $B_{19}^-$ parent [113,114].

### 4.3. $B_{17}^-$ *and* $B_{18}^-$*: hydrocarbon analogues and Wankel motors*

Once the structures of $B_{19}^-$ were solved, the $B_{17}^-$ and $B_{18}^-$ clusters followed readily by Sergeeva *et al.* [31]. The global minima and low-lying isomers of $B_{17}^-$ and $B_{18}^-$ were found to be related to those of $B_{19}^-$. The photoelectron spectra of $B_{17}^-$ and $B_{18}^-$ are shown in Figure 18 at two photon energies. The spectra of $B_{17}^-$ showed relatively high electron binding energies and even a vibrationally resolved PES band at 193 nm (band B in Figure 18(b)), suggesting that the global minimum of $B_{17}^-$ was rigid. The spectra of $B_{18}^-$ exhibited relatively low binding energies with a weak ground state band (band X in Figure 18(c) and (d)), suggesting that neutral $B_{18}$ is closed shell. The global minima and low-lying isomers of $B_{17}^-$ and $B_{18}^-$ are shown in Figure 19. The global minimum of $B_{17}^-$ (I in Figure 19) was found to be perfectly planar and relatively circular with $C_{2v}$ symmetry, which could be viewed to be derived from isomer II of $B_{19}^-$ (Figure 16) by removing the top apex atom of the inner triangle and the adjacent peripheral atom. The second more elongated isomer, which could be viewed as adding one atom to the periphery of $B_{16}^-$ (I in Figure 13), was found to be 19.5 kcal/mol higher in energy, suggesting that the global minimum of $B_{17}^-$ was overwhelmingly stable. The

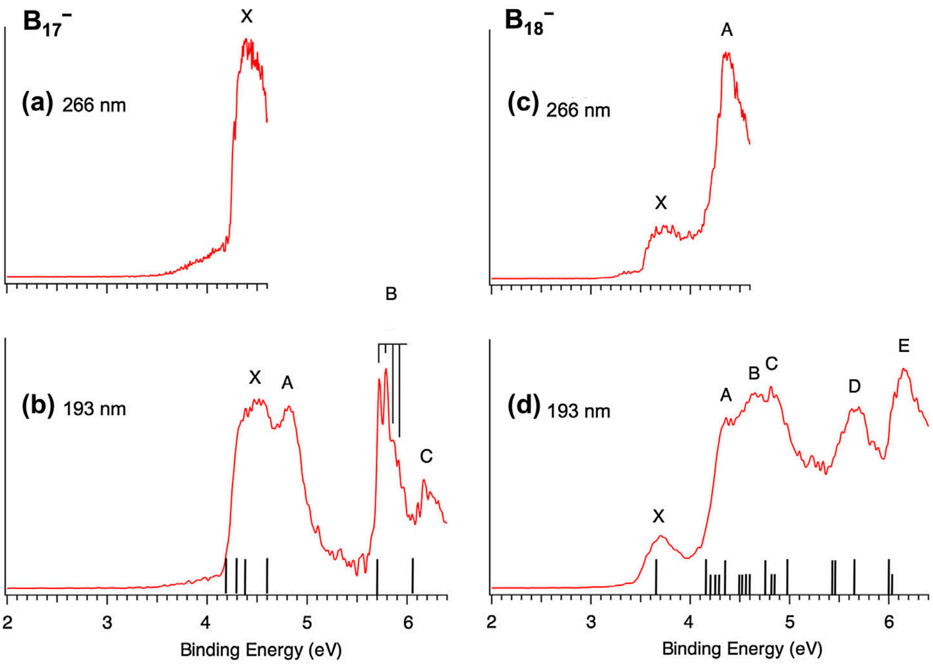

Figure 18. (Colour online) Photoelectron spectra of $B_{17}^-$ and $B_{18}^-$ at two photon energies [31]. The vertical bars in (b) represent the calculated VDEs from the global minimum of $B_{17}^-$ (see I in Figure 19). The long vertical bars in (d) represent the calculated VDEs from the global minimum of $B_{18}^-$ (see V in Figure 19) and the short bars in (d) represent the calculated VDEs from a low-lying isomer of $B_{18}^-$ (see VI in Figure 19).

calculated VDEs from the global minimum of $B_{17}^-$, plotted as vertical bars in Figure 18(b), were in excellent agreement with the photoelectron spectra. The broad X band contained three closely lying detachment channels and there was no hint of any contributions from other isomers.

Two close-lying isomers, which were related to the two low-lying isomers of $B_{19}^-$ (Figure 16), were found for $B_{18}^-$ to compete for the global minimum (Figure 19). The lowest energy structure at both B3LYP and CCSD(T) levels of theory had $C_{3v}$ symmetry (V in Figure 19), which could be viewed as removing a peripheral atom from isomer II of $B_{19}^-$. The reduced periphery caused the inner atoms to be slightly squeezed out of plane, giving rise to the quasi-planar bowl-shaped $C_{3v}$ symmetry. The second isomer of $B_{18}^-$ (VI in Figure 19), which could be viewed as removing a peripheral atom from the global minimum of $B_{19}^-$, was only 1.6 kcal/mol above the $C_{3v}$ global minimum at the CCSD(T) level. Again, the reduced periphery squeezed the inner filled pentagon slightly out of plane, giving rise to the $C_s$ symmetry for this isomer. The calculated VDEs from the $C_{3v}$ global minimum of $B_{18}^-$ are plotted as long vertical bars in Figure 18(d) and they were in good agreement with the main PES features. The calculated VDEs for the $C_s$ isomer were plotted in Figure 18(d) as short bars and they were clearly contributing to the congested spectra, in particular, in the spectral range between 4 and 5 eV, which encompassed nine detachment channels from the $C_s$ isomer.

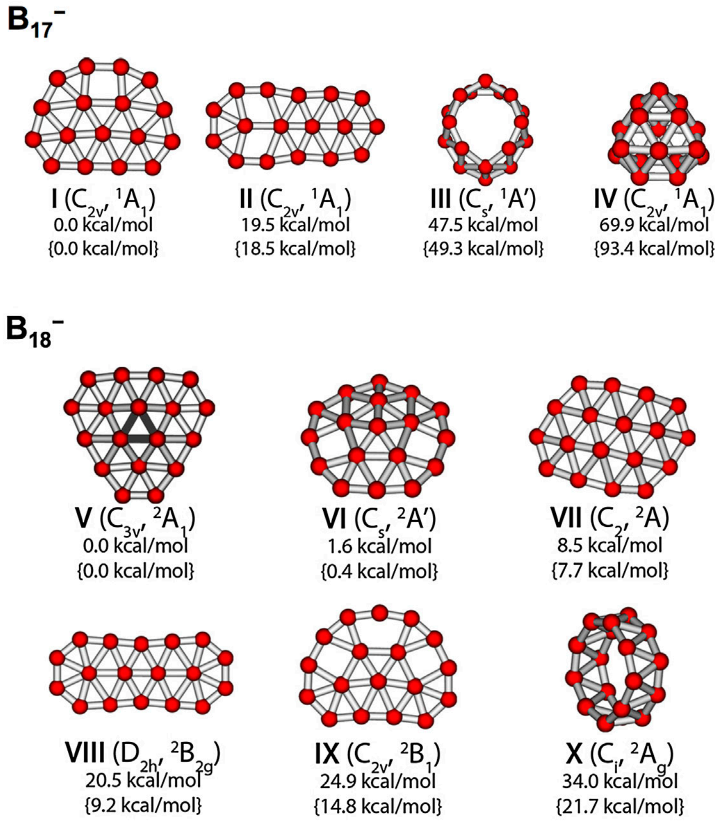

Figure 19. (Colour online) The global minima and low-lying isomers of $B_{17}^-$ and $B_{18}^-$. The relative energies are given at CCSD(T) and B3LYP (in curly brackets) levels of theory [31].

MO analyses showed that $B_{17}^-$ had five filled $\pi$ orbitals with ten $\pi$ electrons [31], similar to those of naphthalene, as shown in Figure 20. In fact, the $\pi$ MOs of $B_{17}^-$ were found to be similar to those of $B_{16}^{2-}$ (Figure 14), even though the latter was more

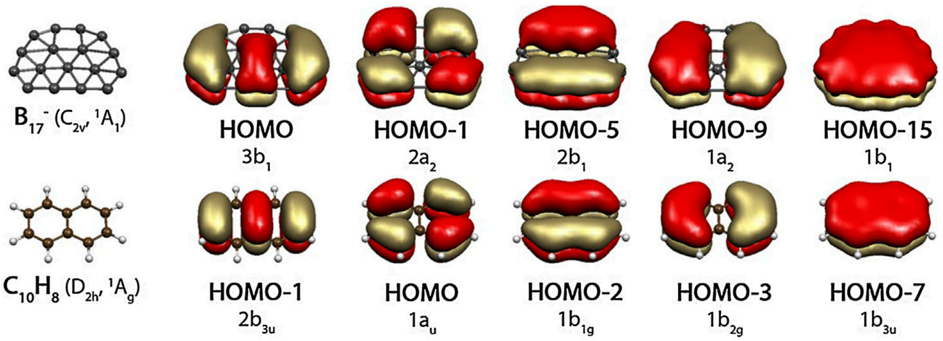

Figure 20. (Colour online) Comparisons of the $\pi$ MOs of the global minimum of $B_{17}^-$ with those of naphthalene [31].

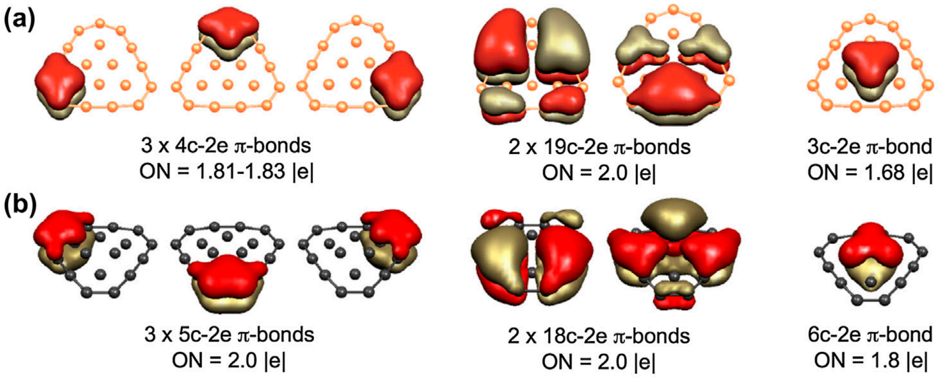

Figure 21. (Colour online) (a) AdNDP analyses of the $\pi$ bonding in the low-lying isomer of $B_{19}^-$ (II in Figure 16) [30]. (b) AdNDP analyses of the $\pi$ bonding in the global minimum of $B_{18}^-$ (V in Figure 19) [31]. ON indicates the occupation number.

elongated. Thus, $B_{17}^-$ was a highly aromatic boron cluster and could also be considered as an all-boron naphthalene. The aromaticity provided considerable electronic stability for $B_{17}^-$, making the $C_{2v}$ global minimum the overwhelmingly stable structure relative to all other isomers of $B_{17}^-$. The structural stability of the aromatic $B_{17}^-$ was also reflected by the relatively sharp PES features, indicating that there was little structural change by detaching an electron from the planar $B_{17}^-$ global minimum. The IR spectrum of neutral $B_{17}$ was obtained and it confirmed that its structure was similar to that of the $B_{17}^-$ global minimum with very little structural distortion [78].

Chemical bonding analyses showed that the $\pi$ bonds in the $B_{18}^-$ global minimum were similar to those of isomer II of $B_{19}^-$, as compared in Figure 21. The $C_{3v}$ $B_{18}^-$ global minimum had a doublet state, but the unpaired electron was found to be in a $\sigma$ MO, resulting in ten $\pi$ electrons and rendering it $\pi$ aromatic. Chemical bonding analyses of the $C_s$ low-lying isomer of $B_{18}^-$ showed that its $\pi$ bonding pattern is similar to that of the global minimum of $B_{19}^-$, despite the fact that it was slightly out-of-plane with a bowl shape. Because the HOMO of the $C_s$ $B_{18}^-$ was a $\pi$ orbital, it was singly occupied. Adding an electron to the $C_s$ $B_{18}^-$ would result in a closed-shell $B_{18}^{2-}$ species with the same number of $\pi$ electrons as that of $B_{19}^-$, and the resulting $B_{18}^{2-}$ could also be viewed as a doubly $\pi$ aromatic system with two concentric $\pi$ sub-systems [31]. In fact, Merino and co-workers have found that the inner filled pentagon in the bowl-shaped $B_{18}^{2-}$ could also undergo hindered-rotations against the $B_{12}$ periphery, making it a member of the molecular Wankel motor family [115].

### 4.4. $B_{20}^-$ *and the double ring conundrum*

The $B_{20}^-$ and $B_{20}$ clusters were solved [27] shortly after the study on $B_{10}^-$ to $B_{15}^-$ [25] and before the study of the $B_{16}^-$ cluster [29], by using the basin-hopping method for global minimum searches [107]. They were included in the 2006 review by Alexandrova *et al.* [28]. They are discussed here because there have been many follow-up studies on their structures and bonding [116–124], in particular, concerning the double ring structure, and because there are still some puzzling issues about the 20-atom boron cluster. The low-lying structures of $B_{20}^-$ and $B_{20}$ are shown in Figure 22. The global

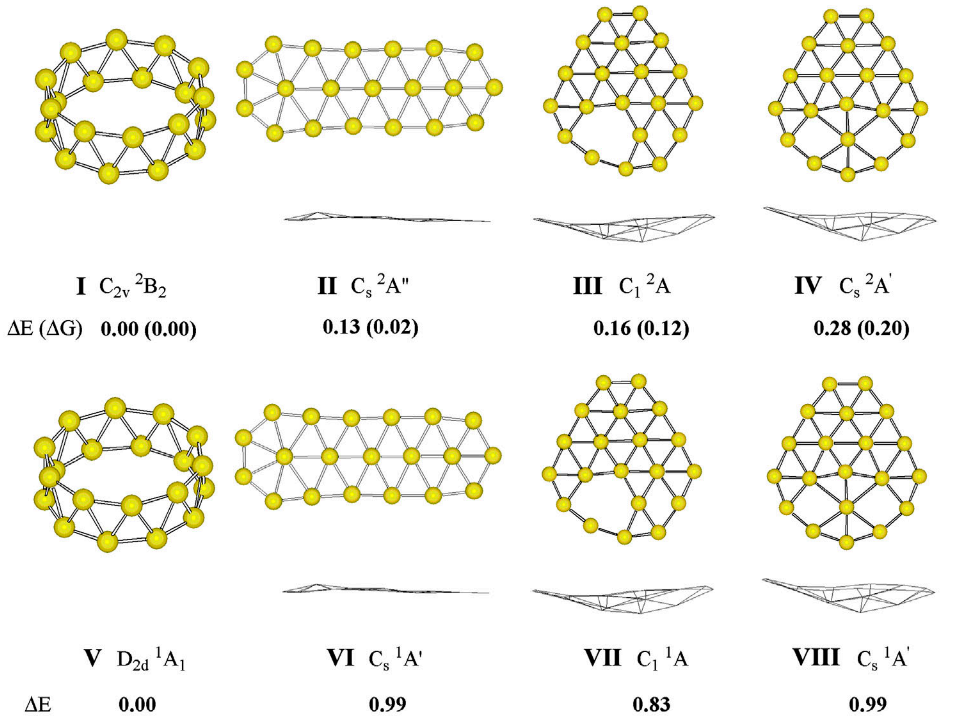

Figure 22. (Colour online) The global minimum and low-lying isomers of $B_{20}^{-}$ (I−IV) and $B_{20}$ (V−VIII) at the B3LYP level of theory [27].

minimum of neutral $B_{20}$ was found to be a beautiful 3D tubular or double-ring structure, whereas the three nearest low-lying isomers were all planar and were nearly 1 eV higher in energy. The $B_{20}$ double ring structure was suggested to be an embryo of single-wall boron nanotubes and $B_{20}$ was considered to be the size, where 2D to 3D structure transition occurred for neutral boron clusters [27].

For the $B_{20}^{-}$ anion, the tubular structure remained to be the global minimum (I in Figure 22), but the three planar isomers were considerably stabilised and isomers II and III were only about 0.13 and 0.16 eV above the tubular isomer, respectively (Figure 22). The simulated PE spectra for isomers I−III are compared with the experimental spectrum in Figure 23. With a small shift, the simulated spectrum of isomer III was almost in quantitative agreement with the major observed PES bands, except the weak band A, which seemed to correspond to the second band of isomer II and provided tangible evidence for its presence experimentally. However, the simulated spectrum of the tubular isomer I totally disagreed with the experiment. In particular, the first VDE of isomer I was quite low, and there was no hint of any PES signals in the same spectral range, suggesting that the tubular isomer was not present in the cluster beam at all. Even with the temperature effects included, the free energy of the tubular structure at 298 K was still lower than isomers II and III (Figure 22). Kinetic argument was invoked to explain the absence of the tubular isomer [27]. But it was not a satisfactory explanation, because it has never been observed experimentally that a true global minimum was not formed, even in small quantity, in the laser vapourisation cluster beam source.

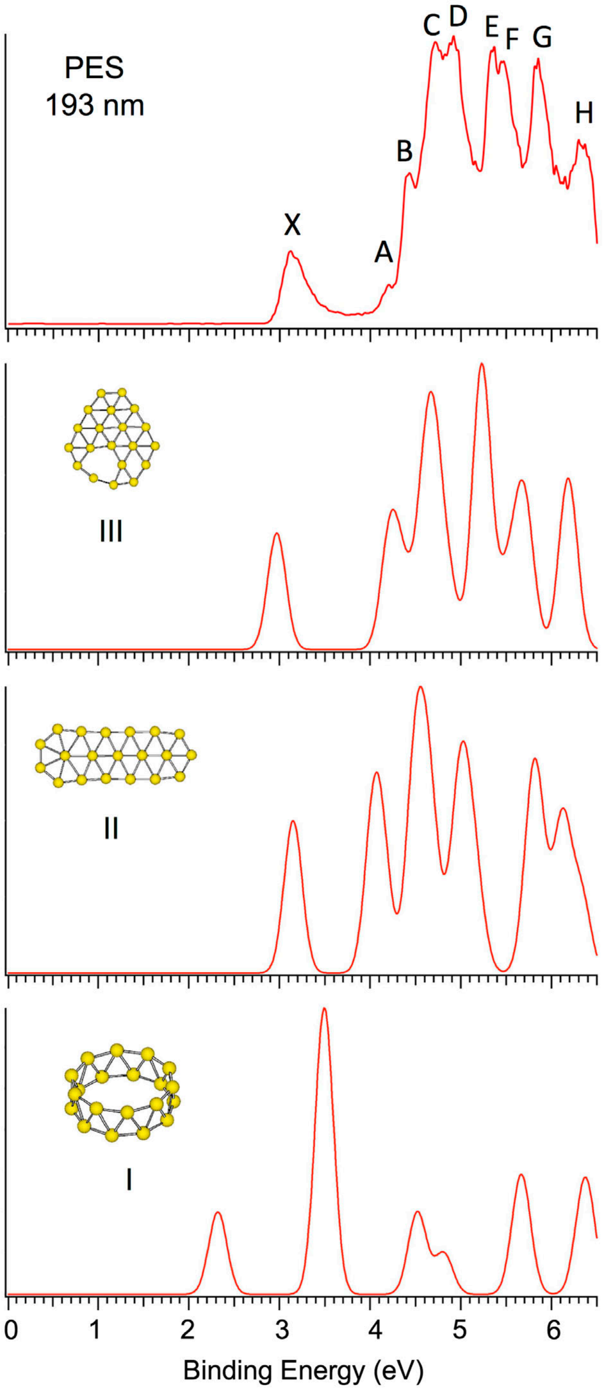

Figure 23. (Colour online) Comparison of simulated photoelectron spectra from isomers I−III of $B_{20}^{-}$ (see Figure 22) with the experimental spectrum measured at 193 nm [27].

Because calculations showed the tubular isomer for neutral $B_{20}$ was overwhelmingly more stable than all the other planar isomers even at the CCSD(T) level of theory [116], one would expect that the tubular $B_{20}$ should be formed in neutral boron cluster beams. The previous IR/UV two-colour experiment [78] was specifically designed to detect the $B_{20}$ double ring structure, which, according to the calculated ionisation energy, should be well suitable for the two-colour scheme. However, no IR spectrum was observed in this experiment, which could be due to one of two reasons: either the IP calculation was not accurate enough or the true global minimum of $B_{20}$ was not the tubular structure. It should be noted that the IP calculations using the same method did predict the correct ionisation energies for $B_{11}$, $B_{16}$, and $B_{17}$, whose IR spectra were successfully measured [78]. Thus, there remains a real possibility that the tubular isomer is not the true global minimum for $B_{20}$. It should be pointed out that no tubular isomers have been observed for any larger boron cluster anions (Figure 8), as will be shown below, even though theoretical calculations did suggest that tubular structures were the lowest energy isomers in a number of cases. It is possible that the available theoretical methods favour the tubular isomer over 2D structures. As shown in the case of $B_9^-$ (Figure 9), different theoretical methods can give quite different relative energies for boron clusters of different structure types [79].

It should be pointed out that ion mobility experiments on cationic boron clusters ($B_n^+$ for $n = 12-25$) have shown that for $n = 16$ to 25 the tubular isomers gave calculated overall cross sections that agreed better with the experimental measurements [77]. In the ion mobility experiment, a size-selected $B_n^+$ cluster was allowed to drift through a helium-filled cell. The drift time depended on the size of the cluster and was used to compute a cross section, which was then used to compare with the calculated cross sections of different low-lying isomers. Since there existed the possibility that different structures might give similar cross sections, it would be desirable to confirm the conclusions from the ion mobility experiments about tubular $B_n^+$ clusters using spectroscopic experiments. Until that is done, the tubular structures for boron clusters still remain an enigma.

## 5. Jumping over $B_{20}^-$ by random walk

Even though the $B_{20}^-$ cluster was solved in 2005 [27], it took seven years to solve the next cluster, $B_{21}^-$ [32]. In addition to the challenges of global minimum searches, the photoelectron spectrum of $B_{21}^-$ was very congested (Figure 24), making it difficult to compare with calculations and posing much more demands on the accuracy of the calculations. To guarantee a more thorough global minimum search, a more efficient method, called Cartesian Walk (CW) [32], was developed by Piazza in the Wang group in collaboration with the Boldyrev group. CW was made to rapidly search for 2D structures, though it could also search for 3D structures. Because of the importance of CW in the investigations of boron clusters beyond 20 atoms, this method is briefly described next before the results of $B_{21}^-$ are discussed.

### 5.1. *The CW global minimum search method*

Local optimisation of trial structures to their corresponding minimum on the potential energy surface was by far the most time consuming step of a global search. Thus, judicious generation of trial structures that were close to their corresponding minimum, while maintaining the generality of randomness, was highly desirable. Trial structures,

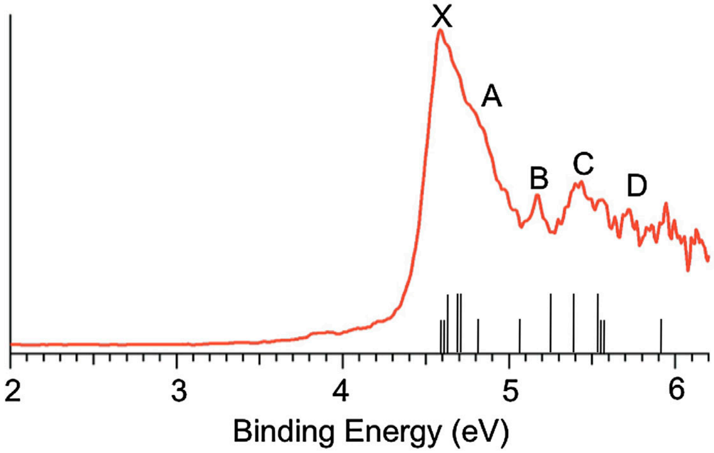

Figure 24. (Colour online) The photoelectron spectrum of $B_{21}^-$ at 193 nm. The long vertical bars represent the calculated VDEs from the global minimum of $B_{21}^-$ (I in Figure 25) and the short bars are for those from the low-lying isomer of $B_{21}^-$ (II in Figure 25) [32].

which did not reach SCF convergence, were inefficient use of computation time and should be avoided as much as possible. The CW method was developed to deal with these issues. The CW method generated trial structures by performing constrained random walks on a user specified Cartesian grid; the trial structures were then optimised using an external quantum mechanical package. Both the overall volume of the grid and the grid mesh could be tailored to a given system. Keeping the volume of the grid small produced the effect of lowering the probability of finding elongated structures, while using a more rectangular grid might bias the search towards elongated structures. The choice of a fine grid mesh allowed for trial structures that could result in highly coordinated atomic centres, while the choice of a more coarse mesh lowered the probability of trial structures. Once the appropriate grid was constructed, a constrained random walk on the grid dictated the geometry of a trial structure.

The random walk took place in the following steps: (1) Atom 1 was placed on the grid at random; (2) A random move up to a set maximum distance from atom 1 was made. If the move landed within a set minimum distance to atom 1 the move was rejected and a new move was made. If not, it was accepted and atom 2 was placed; (3) A random move up to a set maximum distance from atom 2 was made. If the move landed within a set minimum distance of atom 1 or atom 2, the move was rejected and a new move was made. If not, it was accepted and atom 3 was placed; (4) The procedure continued until all atoms were placed; (5) In rare cases, there might be no legal moves, i.e. the system might walk itself into a corner or an atom might become surrounded. Then, the walk started over at step 1.

The effect of the appropriate maximum distance constraint was that the trial structures would never be fragmented, i.e. separated groups of one or a few atoms together. The effect of the appropriate minimum distance constraint was that no two atoms were positioned too close to one another. This led to bond lengths that were close to their relaxed state, which alleviated SCF convergence issues and resulted in relatively quick local optimisations. With appropriately chosen constraints and the proper grid, or set of grids, the overall result was a set of trial structures, which were somewhat tailored to the system at hand while maintaining the generality of a random search. With finite computational resources, the CW method was essential for the global minimum searches for medium-sized boron clusters beyond 20 atoms.

### 5.2. $B_{21}^-$: *a difficult cluster to solve*

The photoelectron spectrum of $B_{21}^-$ at 193 nm is shown in Figure 24 [32]. This spectrum was quite congested with few resolved features and displayed extremely high electron binding energies. In fact, the first VDE of $B_{21}^-$ was the highest among the boron clusters presented in the preliminary Figure 11. The spectrum in Figure 24 represented the most congested photoelectron spectrum up to that size and suggested possible population of several low-lying isomers. Two global minimum search methods were used to locate the low-lying isomers of $B_{21}^-$ to guarantee the authenticity of the search. In addition to the CW method described above, the coalescence kick method was also used [106]. In total, about 4000 trial structures were generated using the coalescence kick method and about 1500 trial structures with the CW method independently. Low levels of theory were used to optimise these structures and then successively higher levels of theory were deployed for the most promising low-lying isomers. The first ten isomers are presented in Figure 25 at two levels of theory: B3LYP and PBE1PBE. The first five isomers were also computed at MP2 and CCSD (T) levels of theory. At the highest level of theory, isomers I and II were found to be nearly degenerate, with isomer II only 1.9 kcal/mol higher in energy, whereas isomer II was lower in energy than isomer I at PBE1PBE and MP2. The method dependence of relative energies was quite common in boron clusters, making it quite dangerous to

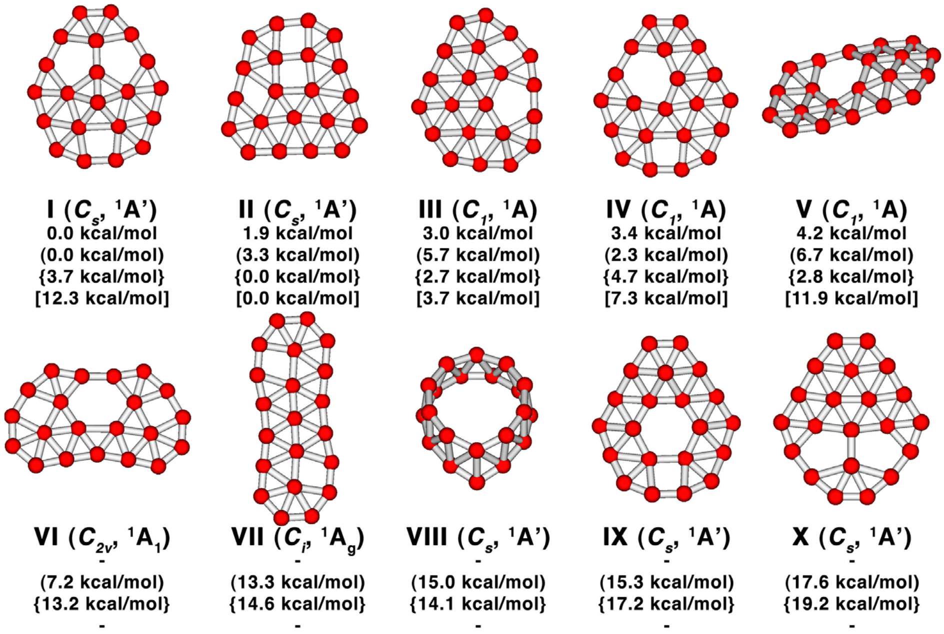

Figure 25. (Colour online) The global minimum and low-lying isomers of $B_{21}^-$ at four levels of theory: CCSD(T), B3LYP (in parentheses), PBE1PBE (in curly brackets), and MP2 (in square brackets) [32].

claim global minimum by using any single computational method. Ultimately, only careful comparison between theory and experiment could truly solve the global minimum for these complicated cluster systems.

The global minimum isomer I had $C_s$ symmetry with two adjacent pentagonal holes. The calculated VDEs from isomer I are shown in Figure 24 as long vertical bars and they were in good agreement with the observed spectrum. The first three detachment channels of isomer I were closely spaced, consistent with the strong and broad spectral bands. There was an energy gap between the first and next three detachment channels of isomer I, but the experimental spectrum was essentially continuous in the higher binding energy side, indicating contributions from other isomers. Isomer II, which also had $C_s$ symmetry with two adjacent tetragonal holes (Figure 25), was very close in energy to the global minimum and was expected to be present in the experiment. The calculated VDEs from isomer II are given in Figure 24 as short bars. The combination of the two isomers gave a very good explanation of the observed spectrum. Without the thorough global minimum searches using the two different methods and the highly accurate calculations, it would have been very difficult to interpret the photoelectron spectrum of $B_{21}^-$ and to ascertain its global minimum.

The bonding of isomers I and II was analysed using AdNDP and showed that they each consisted of fourteen 2c–2e $\sigma$ bonds on the periphery, eleven delocalised $\sigma$ bonds, and six delocalised $\pi$ bonds. For the first time, each isomer also contained a 2c–2e $\sigma$ bond in the interior, localised between the two boron atoms shared by the two pentagonal holes in isomer I and the two boron atoms shared by the two tetragonal holes in isomer II. The anomalously high electron binding energies of $B_{21}^-$ were not well understood. It was possible that they were related to the localised bond in the interior of the 2D clusters. The VDEs for isomers III–V were also computed and their first VDEs were all smaller, 3.5 eV for isomer III, 4.4 eV for isomer IV, and 4.2 eV for isomer V [32]. All these isomers do not have adjacent holes to give rise to a localised B–B bond (Figure 25).

Casillas *et al.* investigated the structures of $B_{21}$ and both its cationic and anionic counterparts using limited step basin-hopping and simulated annealing random searches and DFT calculations [125]. A total of 1191 trial structures were used for neutral $B_{21}$. The charged clusters were computed using the neutral isomers as starting structures. They found that the lowest energy structures for all three charge states of $B_{21}$ were planar. For the anion, the global minimum and the low-lying isomers presented had no overlap with those presented in Figure 25. The calculated electron affinities for all isomers were less than 3.5 eV, much smaller than the experimental observation (Table 1 and Figure 24).

### 5.3. $B_{22}^-$: an all-boron analogue of anthracene

The photoelectron spectrum of $B_{22}^-$ at 193 nm was shown in Figure 26 [33]. In comparison with the spectrum of $B_{21}^-$, the spectrum of $B_{22}^-$ was better structured, but still quite congested, suggesting existence of multiple isomers. The binding energies of $B_{22}^-$ were much lower, compared with the spectrum of $B_{21}^-$. The CW global minimum search was more efficient and was used exclusively to find the global minimum of $B_{22}^-$. Roughly 2000 trial structures were tested and the first four isomers are shown in Figure 27. A double ring structure was found to be the global minimum, but at the CCSD(T) level of theory the double ring was found to be nearly degenerate with a quasi-planar isomer

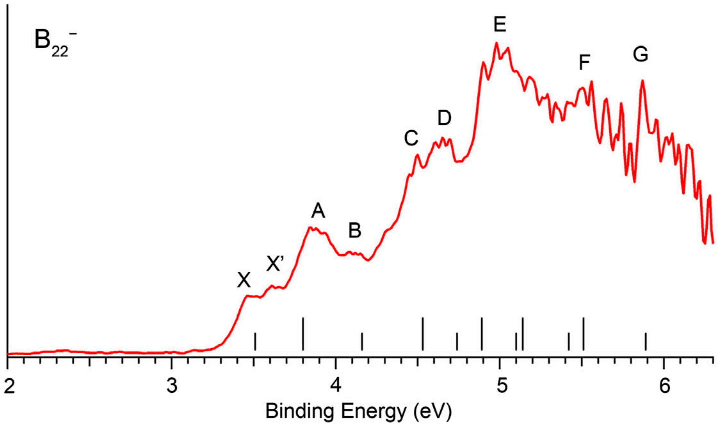

Figure 26. The photoelectron spectrum of $B_{22}^-$ at 193 nm. The vertical bars represent the calculated VDEs from isomer II of $B_{22}^-$ (Figure 27). The short and long vertical bars in this case represent the singlet and triplet final states, respectively [33].

II. Isomers III and IV were both 2D structures with a hexagonal and pentagonal hole, respectively, and they were close in energy with isomer II.

However, the calculated VDEs of the double ring isomer I did not agree with the experiment, and were ruled out to contribute to the observed spectrum, similar to the situation found for $B_{20}^-$ earlier (Section 4.4.). The calculated VDEs from isomer II are plotted as vertical bars in Figure 26 and they were found to be in good agreement with the main PES features. However, there were features present, e.g., band X', which were not accounted for by isomer II. The VDEs for isomers III and IV were also calculated and the first VDEs of both isomers were in agreement with band X', suggesting that they were likely present as minor species in the experiment. The calculations at the CCSD(T) level found significant multi-configurational characters, making the relative energies even at this high level of theory unreliable. Hence, the planar isomer II was probably the true global minimum for $B_{22}^-$ with isomers III and IV as low-lying

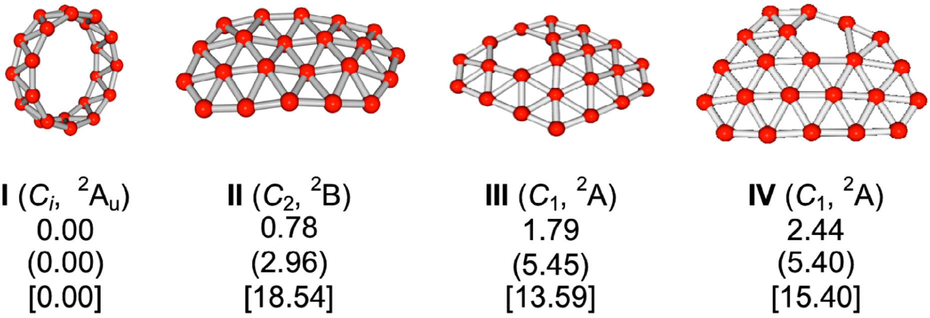

Figure 27. (Colour online) The low-lying isomers of $B_{22}^-$ at three levels of theory: CCSD(T), PBE1PBE (in parentheses), and B3LYP (in square brackets) [33]. Note that the computed VDEs of isomer I did not agree with the experiment.

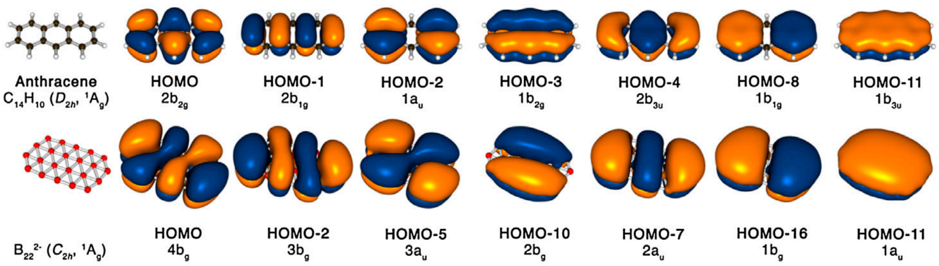

Figure 28. (Colour online) Comparison of the π MOs of a planarised closed-shell $B_{22}^{2-}$ of isomer II of $B_{22}^-$ with those of anthracene [33].

isomers. Higher levels of theory with multi-references are required to confirm the quasi-planar isomer II as the true global minimum of $B_{22}^-$.

Isomer II consisted of a rippled triangular lattice without any defects or holes. Because $B_{22}^-$ was open-shell with an unpaired electron, chemical bonding analyses were done using a closed-shell and planarised $B_{22}^{2-}$ species. MO analyses of this $B_{22}^{2-}$ species showed seven π orbitals, which were similar to anthracene ($C_{14}H_{10}$), as shown in Figure 28. Hence, $B_{22}^{2-}$ could be viewed as an all-boron analogue of anthracene or $B_{21}^-$ could be viewed as an analogue of the anthracene cation ($C_{14}H_{10}^+$). In addition to the seven delocalised π bonds, AdNDP analyses found fourteen localised 2c–2e σ bonds on the periphery of $B_{22}^{2-}$ and thirteen delocalised σ bonds.

Hikmat *et al.* investigated the structures of $B_{22}$ in three charge states using DFT at the PBE level [126]. They tested about 300 trial structures constructed randomly and found that the double ring structure was the lowest in energy for $B_{22}$, $B_{22}^+$, and $B_{22}^-$. The second isomer was found to be planar with a tetragonal hole for all three charge states. In fact, the three 2D structures shown in Figure 27 were not among the low-lying planar structures presented by Hikmat *et al.* Their computed electron affinity for the lowest planar structure was 3.1 eV, which was significantly lower than the experimental value (Table 1 and Figure 26). Pham *et al.* also compared the stability of the tubular $B_{22}$ with planar isomers at the TPSSh level of theory [127]. They found that for neutral and cationic $B_{22}$ the tubular structure was more stable than 2D isomers, in agreement with the previous findings [33,77]. For $B_{22}^-$, they found that the tubular isomer was nearly degenerate with two planar isomers: one was similar to isomer II in Figure 27 and another was an elongated structure by extending $B_{16}^-$ (Figure 13).

### 5.4. $B_{23}^-$: *a nanoheart and all-boron analogue of phenanthrene*

The photoelectron spectrum of $B_{23}^-$ at 193 nm is shown in Figure 29 [33]. This spectrum displayed quite high binding energies and was much less congested relative to that of $B_{22}^-$ or $B_{21}^-$, suggesting there was likely a single isomer responsible for the spectrum. Both the coalescence kick and CW methods were used to search for the global minimum of $B_{23}^-$. The first five isomers are shown in Figure 30 at two levels of theory. A heart-shaped planar structure with a pentagonal hole was found to be the global minimum. The second isomer consisted of a rippled triangular lattice, but was significantly higher in energy. The other three isomers were much higher in energy, including the tubular isomer V in Figure 30. The calculated VDEs of the heart-shaped global minimum are plotted in Figure 29 as vertical bars and the agreement with experiment was

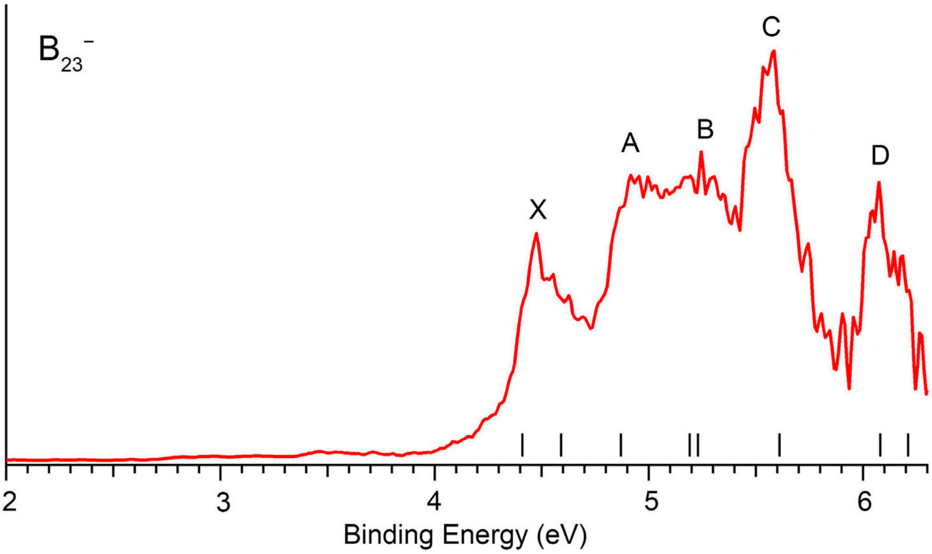

Figure 29. (Colour online) The photoelectron spectrum of $B_{23}^-$ at 193 nm. The vertical bars represent the calculated VDEs from the global minimum of $B_{23}^-$ (I in Figure 30) [33].

excellent. The VDEs of isomer II were also computed, but they disagreed with the experiment. The hear-shaped $B_{23}^-$ was particularly stable and was the only contributor to the observed photoelectron spectrum, confirming firmly that it was the global minimum of $B_{23}^-$.

The heart-shaped global minimum of $B_{23}^-$ was beautiful. MO analyses found seven $\pi$ orbitals, which were identical to those of phenanthrene, as shown in Figure 31. Thus, $B_{23}^-$ could be considered as an all-boron phenanthrene [33]. In addition to the seven delocalised $\pi$ bonds, AdNDP analyses showed that $B_{23}^-$ consisted of fifteen localised 2c–2e $\sigma$ bonds on the periphery and thirteen delocalised $\sigma$ bonds. The aromaticity seemed to play a major role in stabilising the $B_{23}^-$ nanoheart. The heart-shaped $B_{23}^+$ cation would lose two $\pi$ electrons in the HOMO and become $\pi$ antiaromatic, thus much less stable. Indeed, the global minimum of the $B_{23}^+$ cation was shown to be something similar to isomer II, but distorted to $C_2$ symmetry, at the TPSS level of theory [77],

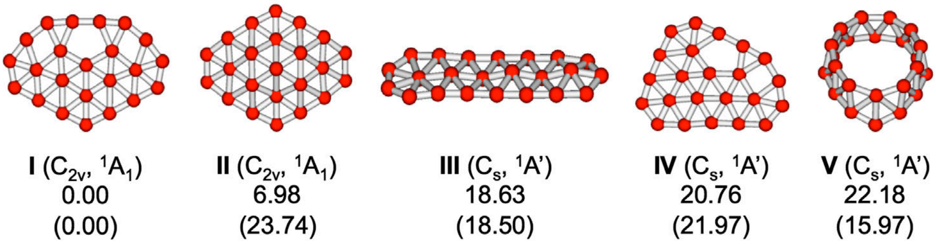

Figure 30. (Colour online) The global minimum and low-lying isomers of $B_{23}^-$ at PBE1PBE and B3LYP (in parentheses) levels of theory [33].

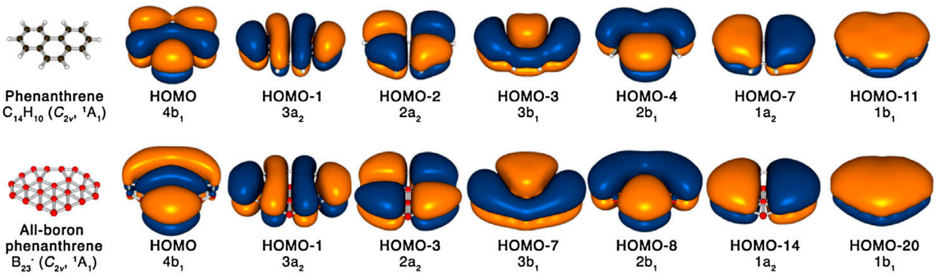

Figure 31. (Colour online) Comparison of the $\pi$ MOs of $B_{23}^-$ with those of phenanthrene [33].

though the ion mobility data was in better agreement with a higher energy, low symmetry tubular structure.

## 5.5. *$B_{24}^-$: a low-symmetry quasi-planar cluster*

The photoelectron spectrum of $B_{24}^-$ at 193 nm is shown in Figure 32(a) [34]. The spectrum was well structured and the gap between the X and A bands suggested a sizable HOMO–LUMO gap, indicating that neutral $B_{24}$ was a closed shell system. Global minimum searches were done using both the coalescence kick and CW methods and about 13,000 trial structures were examined. The eight low-lying isomers, calculated at four levels of theory are shown in Figure 33 [34]. At the two DFT levels of theory, the double ring tubular structure was found to be the global minimum. But at the CCSD(T) level of theory, a low-symmetry quasi-planar structure (I in Figure 33) was found to be the global minimum and the double ring isomer was 4.5 kcal/mol higher in energy. All other isomers from III to VIII were planar and they remained to be higher energy isomers at all levels of theory. The reversed stabilities of isomers I and II again showed the importance of electron correlations.

The VDEs were calculated at two levels of theory and each VDE was fitted with a unit area Gaussian to produce a simulated spectrum, as shown in Figure 32(b) and (c), where the simulated spectra for the global minimum using two theoretical methods are presented. There were some minor differences in the simulated spectra by the two methods, but their overall spectral patterns were similar and were in good agreement with the experiment. The first VDE of the double ring isomer was calculated to be at 2.8 eV [34], much lower than the first experimental VDE and the overall calculated VDEs for the double ring isomer II did not agree with the experiment. Hence, the double ring isomer was ruled out to be present in the experiment. The global minimum of $B_{24}^-$ contained a tetragonal and a pentagonal hole (I in Figure 33). Such defects seemed essential to keep the cluster flat because a perfect triangular lattice of boron was shown to be always rippled. However, the global minimum of $B_{24}^-$ was still quasi-planar owing to the out-of-plane distortion of the boron atom in the centre of the filled pentagonal motif, similar to that observed in the global minimum of $B_{21}^-$ (Figure 25). The appearance of such filled pentagonal units with ever increasing out-of-plane distortions for large boron clusters might hint the onset to form icosahedral motifs found in bulk boron. Chemical bonding analyses using AdNDP on a closed-shell $B_{24}^{2-}$ (at the geometry of the $B_{24}^-$ global minimum) revealed fifteen 2c–2e localised $\sigma$ bonds on the

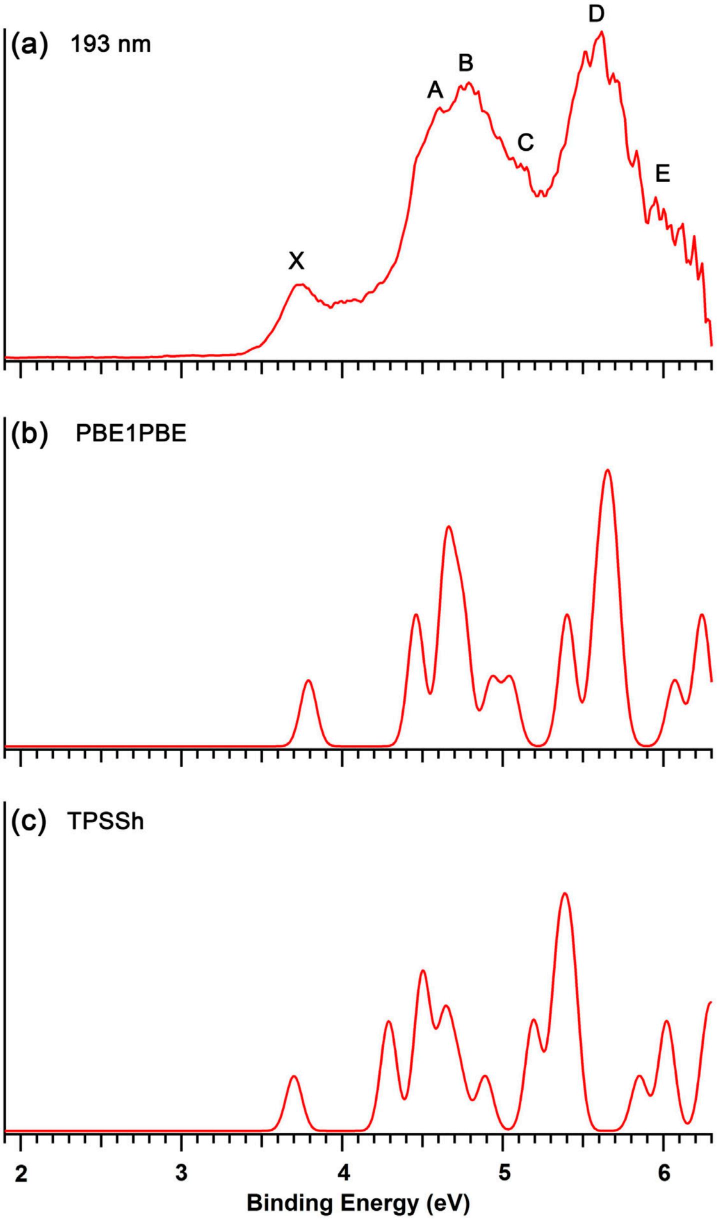

Figure 32. (Colour online) (a) The photoelectron spectrum of $B_{24}^-$ at 193 nm. (b) and (c) Simulated spectra from the global minimum of $B_{24}^-$ (I in Figure 33) at two levels of theory [34].

periphery, fourteen multi-centre $\sigma$ bonds in the interior, and eight delocalised $\pi$ bonds, including a 6c–2e $\pi$-bond over the filled pentagonal moiety [34].

The ion mobility experiment showed that $B_{24}^+$ had the double ring structure as its global minimum [77]. An earlier DFT calculation compared several selected structures of $B_{24}$ and also found the double ring structure was more stable [128]. Pham *et al.*

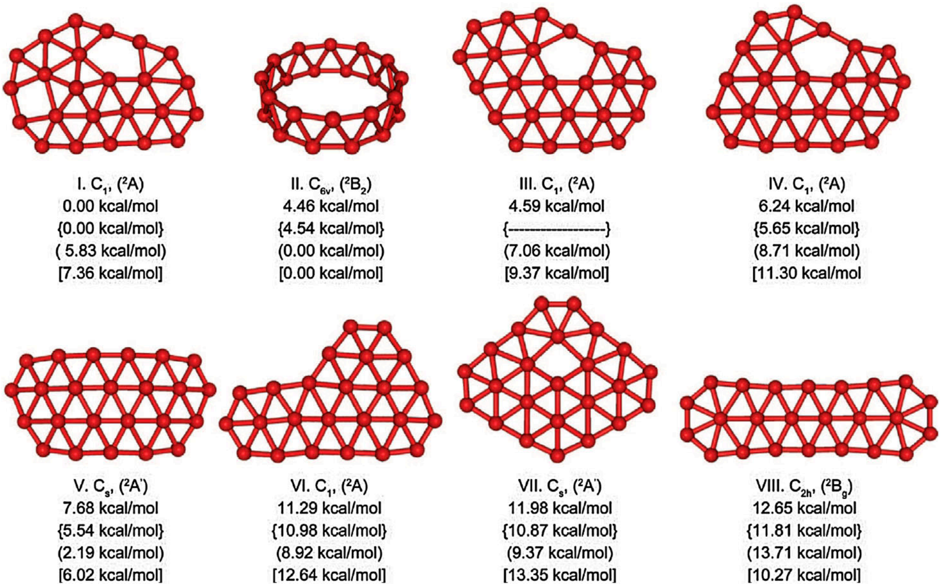

Figure 33. (Colour online) The global minimum and low-lying isomers of $B_{24}^-$ at four levels of theory: ROCCSD, ROCCSD(T) (in curly brackets), PBE0 (in parentheses), and TPSSh (in square brackets) [34].

considered the structures of $B_{24}$ in both its neutral and charged forms using DFT and found that the double ring was more stable regardless of the charge state [127]. All these results were in agreement with the results shown in Figure 33, where at DFT level the double-ring structure was found to be the global minimum. Clearly, in this case DFT was not sufficient to predict the global minimum and the higher-level correlated methods were necessary.

### 5.6. $B_{25}^-$: more planar structures

The photoelectron spectrum of $B_{25}^-$ at 193 nm shown in Figure 34 was congested with broad PES features [35]. Relative to the two smaller odd-sized boron clusters $B_{23}^-$ and $B_{21}^-$, the $B_{25}^-$ cluster showed unusually low electron binding energies (Figure 11 and Table 1). Global minimum searches for $B_{25}^-$ were done using three different methods, coalescence kick, CW, and basin hopping, independently. About 10,000 structures were considered by coalescence kick, 3,000 by CW, and about 250 by basin hopping at low levels of theory. The potential energy landscape of $B_{25}^-$ was very complicated, and many low-lying isomers were found. Consequently, many more structures had to be computed using the very expansive CCSD(T) level of theory. The isomers within 10 kcal/mol of the global minimum at the CCSD(T) level of theory are presented in Figure 35. A total of thirteen isomers were found within this narrow energy range, and three 2D structures (I–III) were found to be within 0.9 kcal/mol of the global minimum. Hence they could all contribute to the experimental spectrum.

The simulated spectra for the three close-lying lowest energy structures are compared with the experimental data in Figure 34. The simulated spectrum of isomer II seemed to agree well with the experimental spectrum. However, on the bases of both

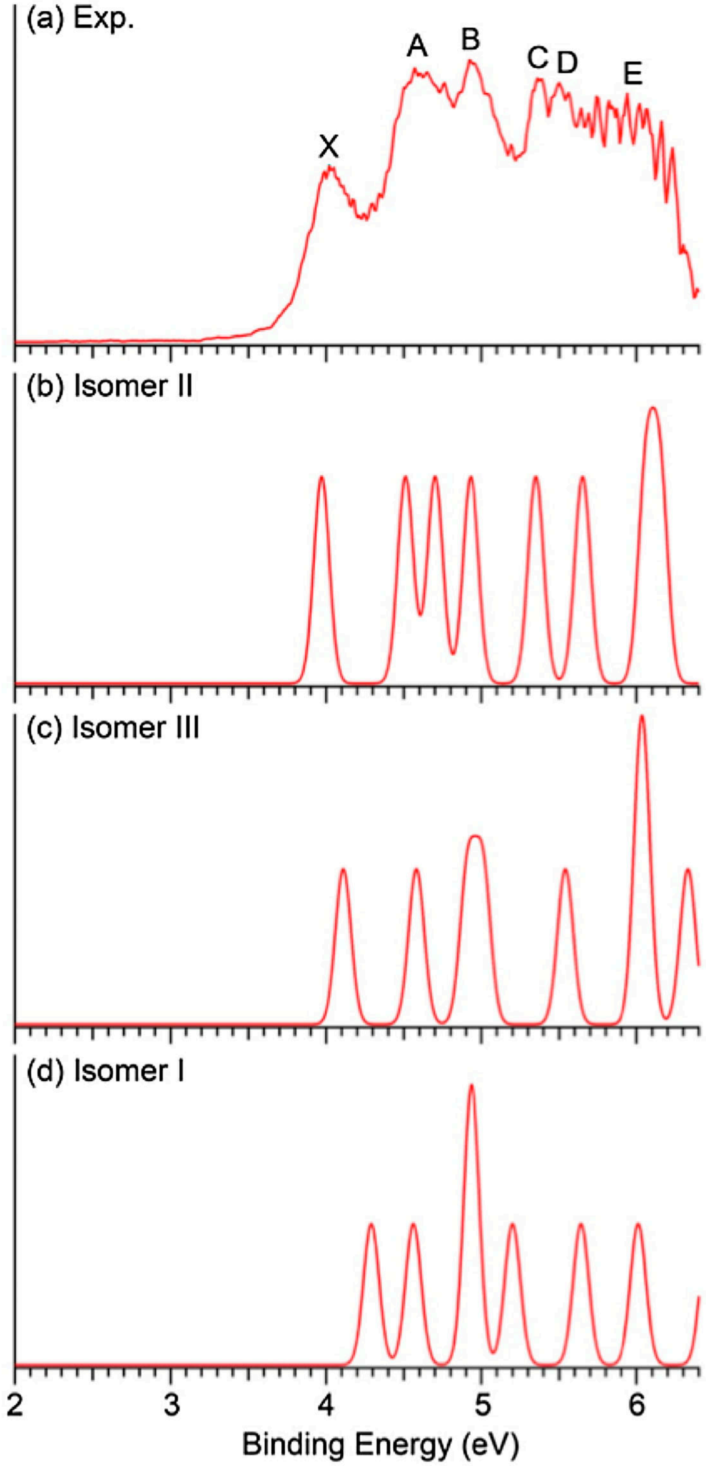

Figure 34. (Colour online) The photoelectron spectrum of $B_{25}^-$ at 193 nm (a), compared with the simulated spectra of isomers I−III of $B_{25}^-$ (see Figure 35) [35].

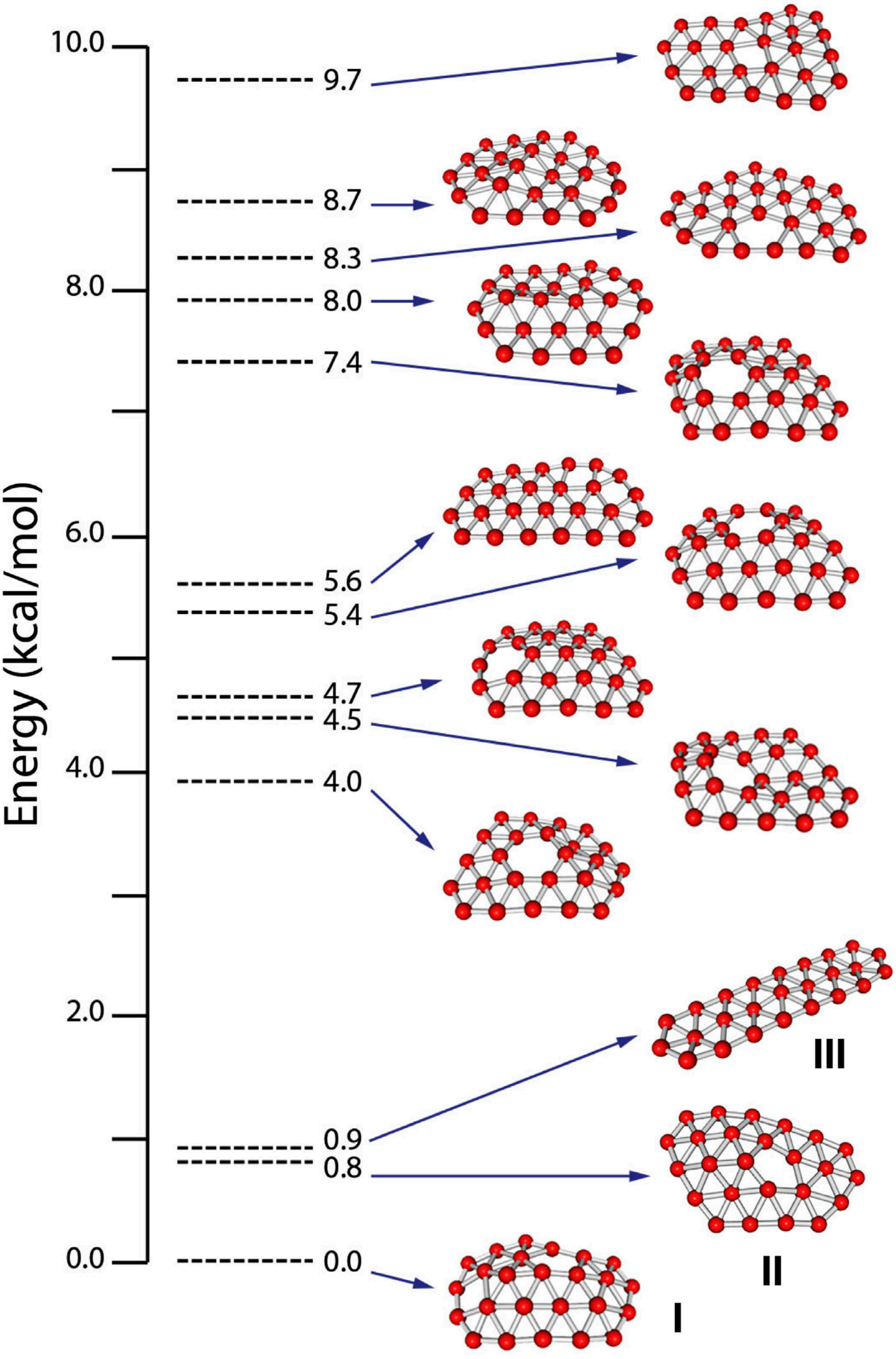

Figure 35. (Colour online) The global minimum and low-lying isomers of $B_{25}^{-}$ within 10 kcal/-mol of the global minimum at the CCSD(T) level of theory [35].

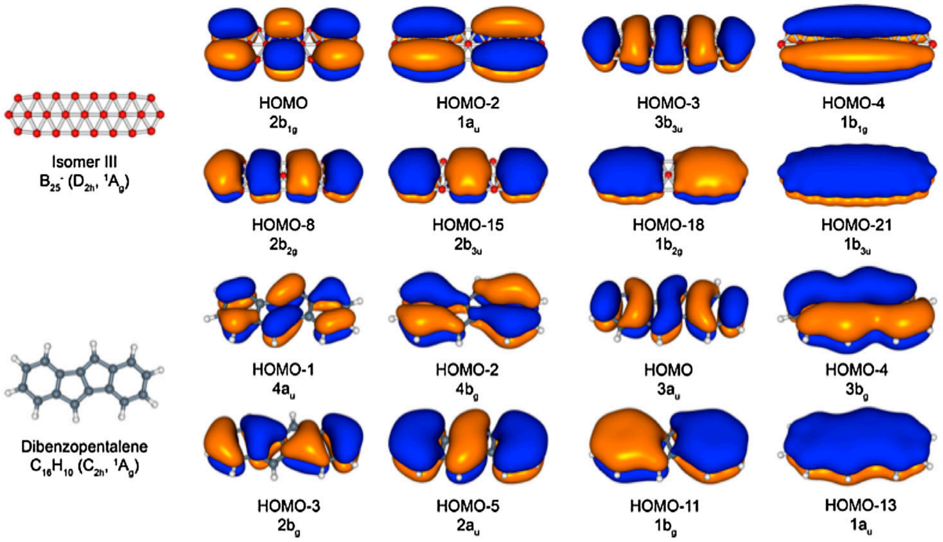

Figure 36. (Colour online) Comparison of the $\pi$ MOs of isomer III of $B_{25}^{-}$ with those of dibenzopentalene [35].

relative energies and the simulated spectra, isomers I and III could not be ruled out. In fact, they could both be present in the experiment and contributed to the broad features. It should be pointed out that at all DFT levels of theory the elongated isomer III was the global minimum. Comparison of the simulated spectra with experiment suggested that isomer II should be the dominant isomer and was most likely the true global minimum. The double ring isomer, which was found to be the global minimum for $B_{25}^{+}$ [77], was found to be a much higher energy isomer for $B_{25}^{-}$.

Both isomers I and II of $B_{25}^{-}$ have low-symmetry quasi-planar structures ($C_1$) with a fifteen-atom periphery and ten interior atoms. Isomer I of $B_{25}^{-}$ was similar to the global minimum of $B_{24}^{-}$ (Figure 33), containing a tetragonal and pentagonal defect, whereas isomer II contained a single pentagonal hole. Chemical bonding analyses showed that both isomers I and II consisted of fifteen 2c–2e $\sigma$ bonds on the periphery, fifteen delocalised $\sigma$ bonds, and eight delocalised $\pi$ bonds. The appearance of the elongated isomer III as a low-lying structure for $B_{25}^{-}$ was interesting. This structure with $C_{2v}$ symmetry was a nano-ribbon and could be viewed as an extension of the global minimum of $B_{16}^{-}$ (Figure 13). Chemical bonding analyses showed that the $B_{25}^{-}$ nano-ribbon contained eighteen peripheral 2c–2e $\sigma$ bonds, twelve delocalised $\sigma$ bonds, and eight delocalised $\pi$ bonds. Interestingly, the $\pi$ bonding of the $B_{25}^{-}$ nano-ribbon was found to be similar to that of the dibenzopentalene hydrocarbon molecule, as shown in Figure 36. Thus, the $B_{25}^{-}$ nano-ribbon was another all-boron analogue of a PAH molecule.

### 5.7. $B_{27}^{-}$: *planar structures with hexagonal holes*

The photoelectron spectrum of $B_{27}^{-}$ at 193 nm shown in Figure 37(a) was also very congested with broad features [36]. The electron binding energies of $B_{27}^{-}$ were also relatively low, similar to $B_{25}^{-}$ (Figure 34). Global minimum searches for $B_{27}^{-}$ were done using both the CW and basin-hopping methods. The first eight low-lying isomers are shown in Figure 38 with their relative energies computed at three levels of theory.

There were three isomers within 5 kcal/mol of each other to compete for the global minimum. Again it was observed that there was a reverse of stability for the first and second isomers between the DFT and CCSD(T) levels of theory. At the DFT levels of

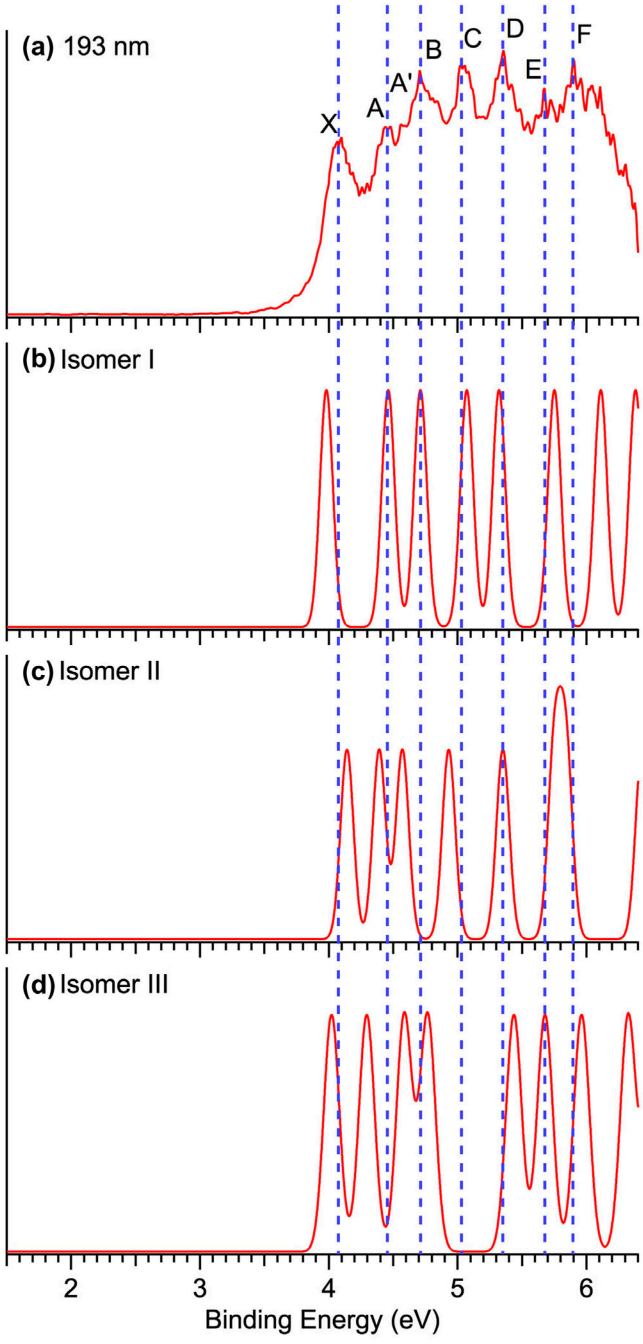

Figure 37. (Colour online) The photoelectron spectrum of $B_{27}^-$ at 193 nm (a), compared with the simulated spectra of isomers I–III of $B_{27}^-$ in Figure 38 [36]. The dashed lines were drawn to guide the eyes.

theory, isomer I with a tetragonal hole was the global minimum, whereas at the CCSD(T) level isomer II with a hexagonal hole was the global minimum. In fact, at the CCSD(T) level the second low-lying isomer was isomer III, which was 3.13 kcal/mol higher in energy, and isomer I was 4.66 kcal/mol in energy above the global minimum. All other isomers from IV to VIII, which were all quasi-planar, remained high in energy at all levels of theory.

The simulated spectra for isomers I to III are compared with the experimental spectrum in Figure 37. The vertical dashed lines over the main PES features were drawn to guide the eyes for comparison with the simulated spectra. Isomers I and II gave very similar simulated PES spectra and both were in good agreement with the experiment. Isomer III, though higher in energy in all levels of theory, could not be ruled out on the basis of the simulated spectrum and could make minor contributions to the observed spectrum. But the comparison between theory and experiment could not determine either isomer I or II as the global minimum. They might be present experimentally in comparable populations, giving rise to the broad PES features.

All the three low-lying isomers of $B_{27}^-$ consisted of sixteen peripheral atoms and eleven interior atoms. However, chemical bonding analyses of isomers I to III revealed that the presence of the hexagonal hole had significant consequences in the bonding and electronic structures of the different isomers. AdNDP analyses showed that isomer I consisted of sixteen 2c–2e peripheral $\sigma$ bonds, sixteen delocalised $\sigma$ bonds, and nine delocalised $\pi$ bonds. For isomers II and III, each was found to consist of sixteen 2c–2e peripheral $\sigma$ bonds, seventeen delocalised $\sigma$ bonds, and eight delocalised $\pi$ bonds. The presence of the hexagonal hole seemed to favour more delocalised $\sigma$ bond over $\pi$ bond.

The appearance of a hexagonal hole among the global minima in $B_{27}^-$ was interesting. In fact, $B_{27}^-$ was the smallest boron cluster with such a structural feature among its most stable isomers. Isomers with hexagonal holes were observed in smaller

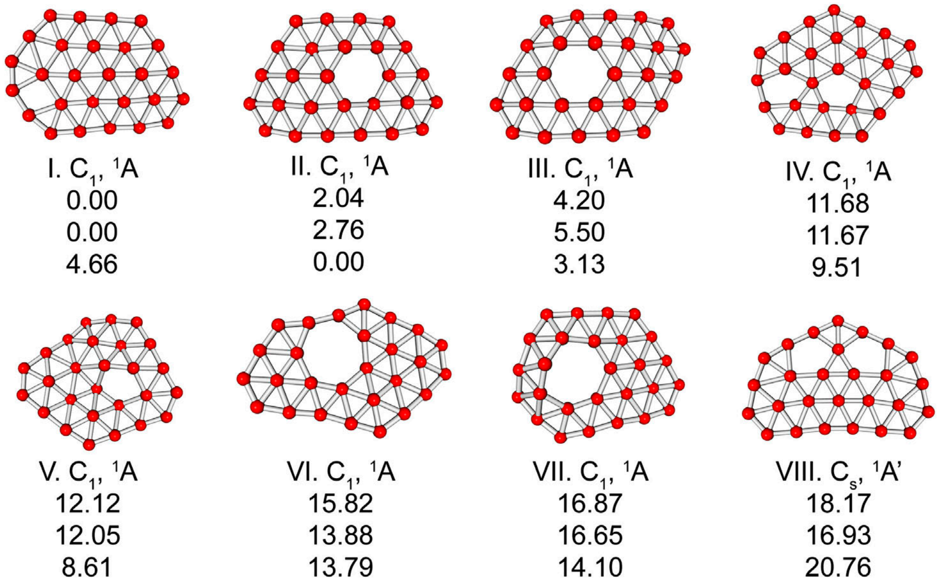

Figure 38. (Colour online) The global minimum and low-lying isomers of $B_{27}^-$ at three levels of theory: PBE0 (top), TPSSh (middle), and CCSD(T) (bottom) [36].

clusters, but they were all high energy isomers (see Figures 25, 27, 35). As will be discussed below, the 36-atom boron cluster was first discovered to have a hexagonal planar structure featuring a hexagonal hole, which provided indirect experimental evidence for the viability of borophenes [45]. It was also interesting to note that 2D clusters with heptagonal holes also appeared to be among the low-lying isomers in $B_{27}^-$ (VI and VII in Figure 38). As will be shown below, heptagonal holes were observed in the first all-boron fullerene, $B_{40}$ [46], and they seemed to be common in borospherenes.

Recently, a computational study has been presented on $B_n$ ($n = 26-29$) at both PBE and CCSD(T) levels of theory by Tai *et al.* [129]. The global minimum of their $B_{27}^-$ was similar to isomer II in Figure 38 with a low-lying isomer, which appeared to be a mirror-image of isomer III (which is chiral). However, isomer I was not among the presented low-lying structures by Tai *et al.* Furthermore, the presented simulated photoelectrons spectra for the two low-lying isomers seemed to have little resemblance to the experimental spectrum shown in Figure 37(a).

## 6. Borophenes and boron clusters with hexagonal vacancies

The preliminary Figure 11 showed that the $B_{36}^-$ cluster had an unusually low electron binding energy, suggesting that it might have an interesting structure with high symmetry. However, for several years it could not be solved because of the challenges of global minimum searches. With the increasing computational power and the development of the CW global minimum search method, a breakthrough was made in 2013 to solve the structures of $B_{36}^-$ and $B_{36}$ [45]. Their quasi-planar hexagonal global minima with a central hexagonal hole were quite surprising and they provided indirect experimental evidence for the viability of mono-layer boron sheets with hexagonal vacancies, dubbed borophenes. Upon solving $B_{36}^-$, the solutions of several mid-sized boron clusters were quickly followed [130–132], including the even more surprising $B_{40}$ borospherene [46], which will be discussed in the next section.

### 6.1. *The hexagonal planar $B_{36}$ and evidence for the viability of borophene*

#### 6.1.1. *PES and comparison with theoretical calculations*

The photoelectron spectra of $B_{36}^-$ are shown in Figure 39 at two detachment photon energies, revealing anomalously low electron binding energies [45]. The ground state band (X) yielded a first VDE of 3.3 eV and an ADE of 3.12 eV (Table 1 and Figure 11). The ADE also represented the EA of neutral $B_{36}$, and it was lower than that of all the smaller clusters above $B_{20}$. The global minimum of $B_{36}^-$ was first searched using the CW method. Among roughly 500 trial structures, a quasi-planar structure with near $C_{6v}$ symmetry and a central hexagonal hole was found to be the lowest energy structure. To confirm this result, the global minimum was further searched using a constrained basin-hopping method, called TMmin, developed in Jun Li's group at Tsinghua University [45]. Among the approximately 2500 structures generated by TGmin, again a pseudo-$C_{6v}$ $B_{36}^-$ was found to be the global minimum, consistent with the CW search. The global minimum and two low-lying isomers of $B_{36}^-$ are shown in Figure 40(a). The global minimum of $B_{36}^-$ actually had $C_{2v}$ symmetry with a doublet electronic state ($^2A_1$), slightly distorted from the perfectly hexagonal $C_{6v}$ symmetry. At the PEB0 level of theory, the second isomer had a tubular or triple-ring structure and the third isomer was 2D with a hexagonal and a heptagonal double hole. At the higher

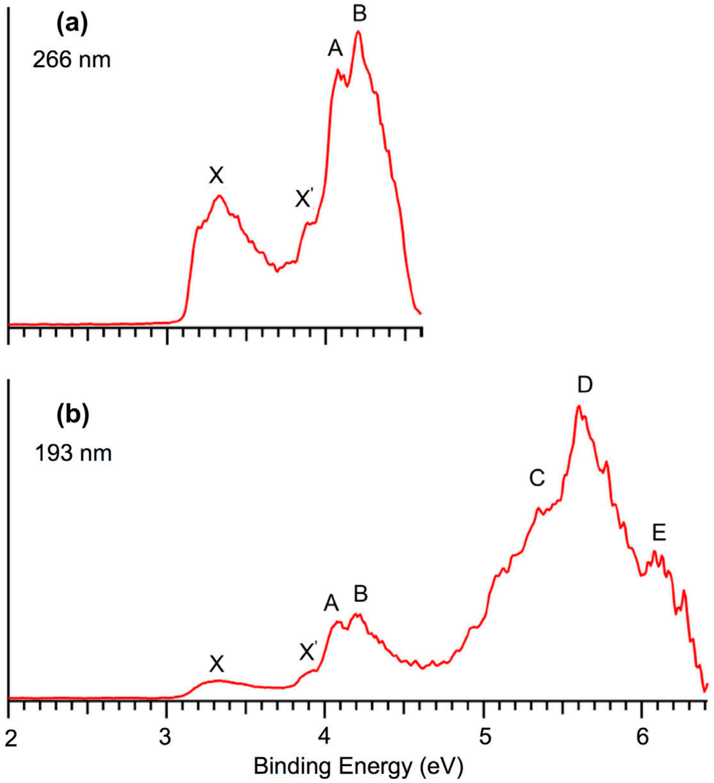

Figure 39. The photoelectron spectra of $B_{36}^-$ at (a) 266 nm and (b) 193 nm [45].

CCSD level, the 2D isomer III was only 1.17 kcal/mol above the global minimum, whereas the tubular isomer II was much higher in energy, being 23.97 kcal/mol above the global minimum. For neutral $B_{36}$, the structures of the anions by removing an electron were optimised at the PBE0 level of theory. The hexagonal global minimum became perfectly $C_{6v}$ symmetry with a close-shell electronic configuration ($I^0$ in Figure 40(b)). The tubular and the double-hole 2D isomer were at least 20 kcal/mol higher in energy.

The simulated spectra of isomers I to III are compared with the experimental spectrum in Figure 41. The simulated spectrum of isomer I was in excellent agreement with the experiment, providing unequivocal evidence for the hexagonal global minimum for $B_{36}^-$. The simulated spectrum of the tubular isomer II did not agree with the experiment. On the bases of both the simulated spectrum and the energetics, the tubular structure could be ruled out. If the CCSD energy was reliable, the double-hole 2D isomer III should be accessible experimentally. The simulated spectrum of isomer III would be overlapped with features of the dominating global minimum. The weak X’ feature was in good agreement with the first calculated VDE of isomer III and could be taken as experimental evidence for the population of the double hole 2D isomer, which was quite interesting on its own right, though in the neutral this isomer was much higher in energy at the PBE0 level ($III^0$ in Figure 40(b)).

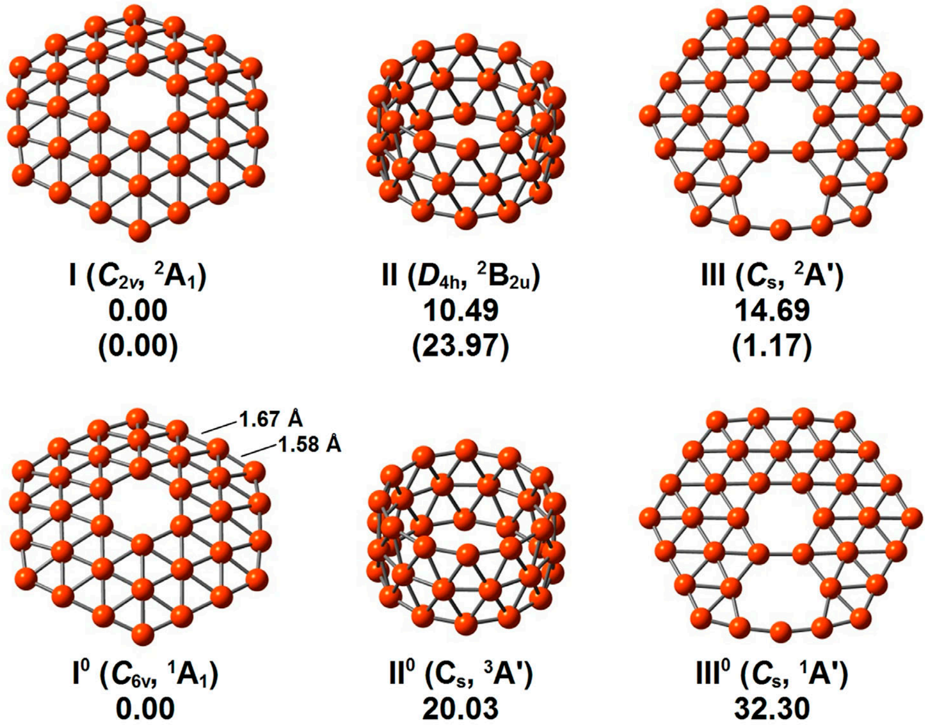

Figure 40. (Colour online) The global minimum and low-lying isomers of $B_{36}^-$ (a) and $B_{36}$ (b) [45].

### 6.1.2. *Chemical bonding analyses*

Results of chemical bonding analyses for the $C_{6v}$ $B_{36}$ using AdNDP are shown in Figure 42. Because the peripheral bonds were not equivalent, twelve 2c–2e peripheral $\sigma$ bonds were found and the six slightly longer peripheral bonds were found to involve in 3c–2e $\sigma$ bonds. The inner $B_6$ hexagon was also found to involve in six 3c–2e $\sigma$ bonds. There were eighteen 4c–2e $\sigma$ bonds, which suggested that the $B_{36}$ cluster could be viewed as six filled hexagonal $B_7$ ($B@B_6$) units. The $\pi$ bonding patterns were also very interesting. There were six 4c–2e $\pi$ bonds on the outer part of the $B_{36}$ cluster and six completely delocalised 36c–2e $\pi$ bonds. Because the AdNDP analyses did not give unique solutions for the bonding pattern [85], Chen *at el.* found a beautiful analogy of the $\pi$ bonding pattern of $B_{36}$ with that of coronene with slightly lower occupation numbers [133], extending the PAH analogy of 2D boron cluster to a very large system.

### 6.1.3. *The implication of the hexagonal $B_{36}$ for the viability of borophenes*

Because of its electron deficiency, boron cannot form the hexagonal layers like graphene. By filling a boron atom to the centre of the hexagon in a graphene-like structure, one obtains a boron sheet with a triangular lattice, which has been considered for boron nanotubes [134,135]. However, such a triangular lattice is too electron-rich and out-of-plane distortions occur, giving rise to a rippled boron layer [136–139]. It was proposed via DFT calculations that a triangular lattice with periodic hexagonal holes

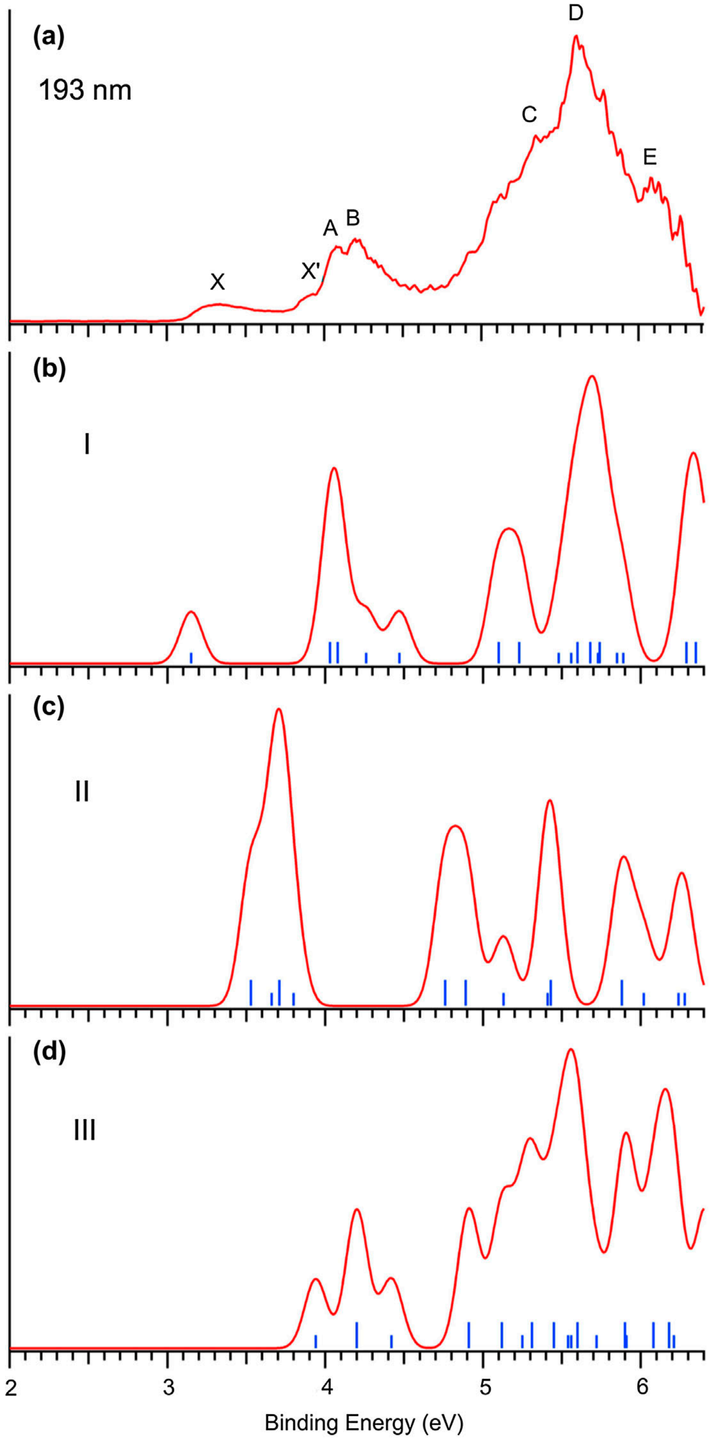

Figure 41. (Colour online) Comparison of the photoelectron spectrum of $B_{36}^{-}$ (a) with simulated spectra from isomers I−III of $B_{36}^{-}$ in Figure 40 [45].

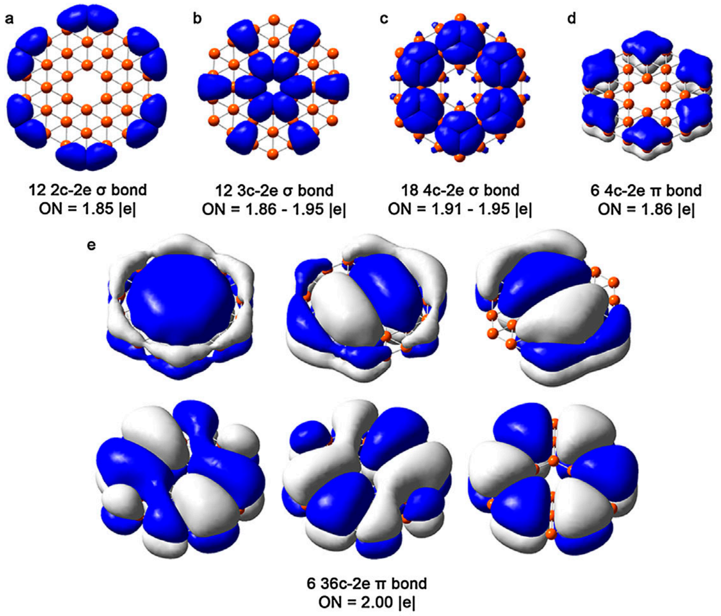

Figure 42. (Colour online) AdNDP analyses of the chemical bonding in the global minimum of $B_{36}$ [45]. ON indicates the occupation number.

was much more stable than a close-packed triangular lattice [140,141]. More importantly, such a structure was perfectly planar and would be better to form boron nanotubes [141,142]. However, monolayer boron has not been realised experimentally, even though there have been extensive theoretical studies [143–148].

The hexagonal hole in the $B_{36}$ cluster is reminiscent of the hexagonal holes in the 2D boron sheets [140,141]. The $B_{36}$ cluster can be viewed as the analogous boron unit of the hexagonal $C_6$ unit in graphene to form extended graphene-like boron nanostructures with hexagonal holes, as shown schematically in Figure 43. The structure shown in Figure 43 represented a hexagonal hole density of $\eta = 1/27$ (one vacancy per 27 lattice sites in a triangular lattice), as defined for the 2D boron sheet [140]. The structure in Figure 43 was constructed by sharing a row of B atoms between two neighbouring $B_{36}$ units. The apex atoms (circled in Figure 43) were shared by three neighbouring $B_{36}$ units. If these atoms were removed, one arrived at the more stable $\alpha$-sheet with $\eta = 1/9$ [140,141]. A $B_{30}$ model cluster was used to analyse the bonding in the proposed $\alpha$-sheet [99], which was equivalent to removing all six apex B atoms in the $B_{36}$ cluster. Hence, it was suggested that the $B_{36}$ cluster could be viewed as the embryo for the proposed stable 2D boron sheets. More importantly, the hexagonal $B_{36}$ provided indirect evidence for the viability of monolayered boron with hexagonal vacancies. A name 'borophene' was, thus, coined to designate this class of new boron nanostructures [45].

However, it should be pointed out that Figure 43 was only schematically showing the relationship between the $B_{36}$ cluster with a hexagonal hole and the putative borophene. It did not represent the growth mechanism of borophenes. Because bulk boron does not have a layered structure, it would be difficult to achieve free-standing

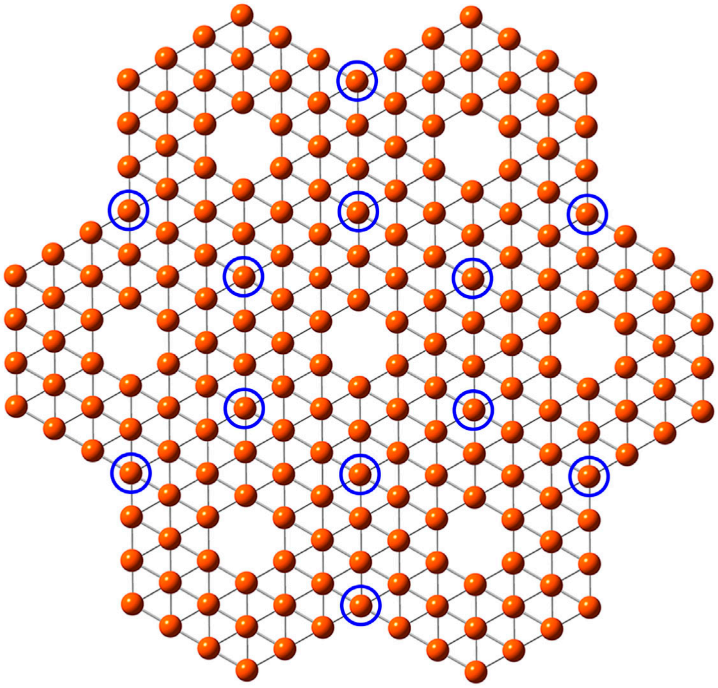

Figure 43. (Colour online) A schematic view of building up an atom-thin boron sheet with hexagonal holes or borophene using the hexagonal $B_{36}$ by sharing one role of boron atoms between neighbouring $B_{36}$ units [45]. Removal of the circled atoms would result in the so-called $\alpha$-sheet.

borophenes. It is likely that borophene would have to be grown on relatively inert substrates. It was suggested computationally that coinage metals would be suitable substrates for borophenes or they may be formed on surfaces of metal borides [146–148]. Thus, $B_{36}$ or other small boron clusters with hexagonal holes may serve as the nucleus for the formation of large scale borophenes on surfaces.

Several theoretical studies on large boron clusters have appeared recently, reporting 2D structures with various arrangements of hexagonal holes. Xu *et al.* investigated $B_n$ ($n = 30-51$) and found a stable planar $B_{49}$ cluster with a double-hexagonal vacancy (DHV) [149]. Kumar and co-workers studied the $B_{84}$ cluster and found a quasi-planar structure with four hexagonal holes [150]. This 2D structure was shown to be more stable than various tubular structures containing hexagonal holes.

### 6.2. $B_{35}^-$: a planar boron cluster with a DHV and a more flexible motif for borophenes

The photoelectron spectrum of $B_{35}^-$ at 193 nm shown in Figure 44(a) was well resolved and appeared relatively simple, suggesting that there were likely no mixtures of low-lying isomers [131]. The $B_{35}^-$ spectrum displayed some resemblance to the high binding energy part of the $B_{36}^-$ spectrum minus the X band (Figure 39(b)). This observation hinted that the structure of $B_{35}^-$ might be similar to $B_{36}^-$. A thorough global minimum search was carried out using TGmin, as well as minimum-hopping [151].

The global minimum of $B_{35}^-$ is shown in Figure 45, featuring a DHV. The global minimum of $B_{35}^-$ was quasi-planar with a closed shell electronic state ($^1A'$). The lowest-lying isomer was in fact a triplet state of the same structure as the global minimum at 12 kcal/mol above the global minimum singlet state at the PBE0 level of theory. All other isomers were at least 14 kcal/mol higher in energy above the global minimum, suggesting the overwhelming stability of the DHV structure for $B_{35}^-$. The simulated spectrum of the DHV global minimum of $B_{35}^-$ is compared with the experiment in Figure 44. The agreement with the experiment was almost quantitative, providing firm confirmation of the stability of the DHV global minimum for $B_{35}^-$. The excellent agreement between experiment and theory also indicated that there was no population of low-lying isomers experimentally.

The DHV global minimum of $B_{35}^-$ could be viewed as removing an atom from the hexagonal $B_{36}^-$ cluster with little structural change. In fact, the DHV structure of $B_{35}^-$ could be overlaid on top of the hexagonal $B_{36}^-$ global minimum, consistent with the PES similarity of the two clusters. Chemical bonding analyses for $B_{35}^-$ using AdNDP are shown in Figure 46(a), featuring eighteen localised 2c–2e peripheral $\sigma$ bonds and a

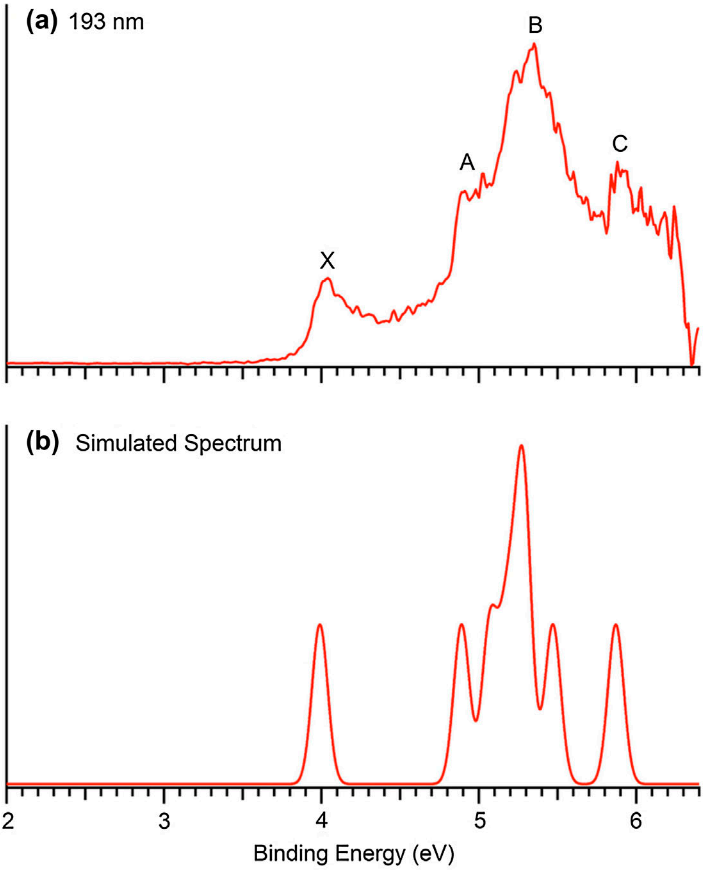

Figure 44. (Colour online) The photoelectron spectrum of $B_{35}^-$ at 193 nm (a), compared with the simulated spectrum of the global minimum of $B_{35}^-$ (Figure 45) [131].

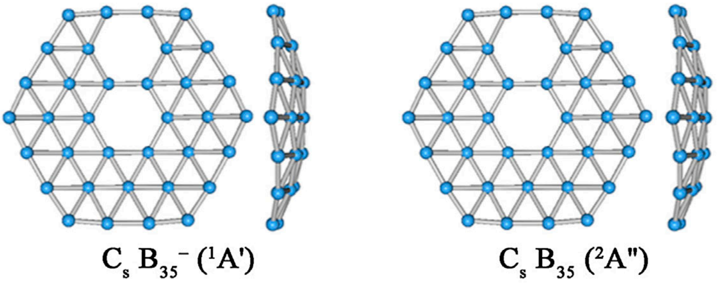

Figure 45. (Colour online) The global minimum of $B_{35}^-$ and $B_{35}$ [131].

localised interior 2c–2e $\sigma$ bond between the two hexagonal holes. A similar localised interior 2c–2e $\sigma$ bond was observed in $B_{21}^-$ between its two pentagonal holes (Figure 25) [32]. In addition, there were twenty-three delocalised $\sigma$ bonds and eleven delocalised $\pi$ bonds. The $\pi$ bonding in $B_{35}^-$ was found to be analogous to that in the benzo(g,h,i)perylene PAH molecule ($C_{22}H_{12}$), as shown in Figure 46(b).

The central hexagonal hole in the $C_{6v}$ $B_{36}$ was critical for its 2D structure. The slight out-of-plane distortion was really due to the peripheral effect, i.e. the peripheral B–B bonds tend to be stronger or slightly shorter than the interior B–B bonds. It was interesting to note that the second hexagonal hole in $B_{35}^-$ induced very little structural distortion and in fact made the cluster slightly more planar, reinforcing the importance of hexagonal vacancies in the stabilisation of borophenes. The hexagonal $B_{36}$ cluster was considered as a motif for borophene consisting of isolated hexagonal holes or the $\alpha$-sheet (Figure 43). Other monolayer boron sheets were also considered theoretically with different hexagonal hole density and patterns [143,144]. For example, the so-called $\beta$-sheet referred to boron monolayers with DHVs or adjacent hexagonal holes [140]. It was found that the planar $B_{35}$ cluster was in fact a more flexible motif to construct borophenes with DHVs or mixed hexagonal holes and DHVs. Figure 47 shows schematically two such arrangements [131]. Other arrangements of the $B_{35}$ clusters would be possible, allowing the creation of borophenes with different hole densities.

### 6.3. $B_{30}^-$: *a quasi-planar chiral cluster with a hexagonal vacancy*

The structures of $B_{35}^-$ and $B_{36}^-$ showed that the hexagonal vacancy was a characteristic structural feature for mid-sized boron clusters. For smaller clusters, tetragonal and pentagonal defects were common (Figure 8). In fact, $B_{27}^-$ was the smallest boron cluster to have a hexagonal hole among its low-lying structures (Figures 8 and 38). To find the smallest boron clusters with the hexagonal hole, $B_{30}^-$ was first studied before $B_{27}^-$ was solved [130], partly because $B_{30}^-$ had a more distinct photoelectron spectrum, as shown in Figure 48(a) at 193 nm. The X and A band separation in the spectrum indicated a significant HOMO-LUMO gap in neutral $B_{30}$. The global minimum search for $B_{30}^-$ was done using the TGmin code [45]. The top eleven isomers were computed at both the PBE0 and LPNO-CCSD levels of theory, as shown in Figure 49. The global minimum was found to be a degenerate pair of quasi-planar structure (I and II in Figure 49), each featuring a hexagonal hole. It turned out that isomers I and II were mirror images of each other and were the enantiomers of a chiral global minimum. Isomer III was only 1.9 kcal/mol higher in energy also featuring a hexagonal hole in a different position of

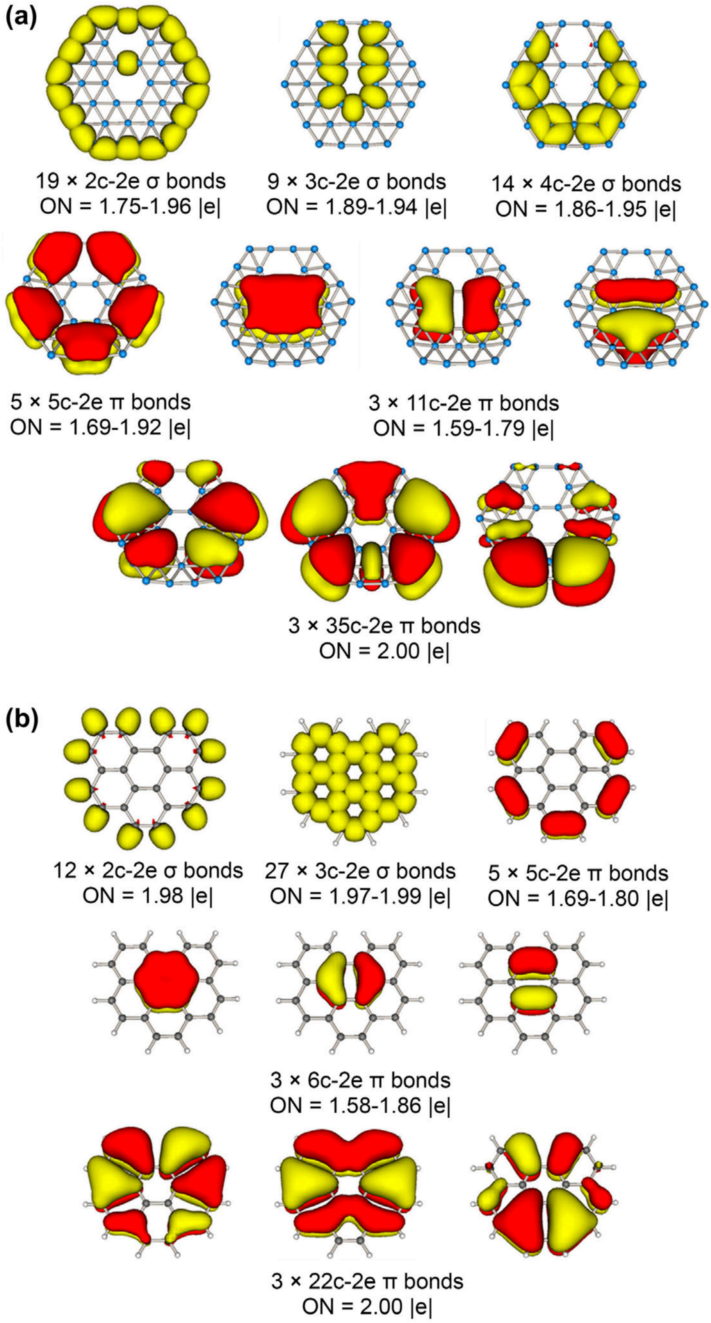

Figure 46. (Colour online) Comparison of the chemical bonding of $B_{35}^{-}$ with that of the $C_{22}H_{12}$ PAH molecule using AdNDP analyses [131]. Note the similarity in $\pi$ bonding in the two systems. ON indicates the occupation number.

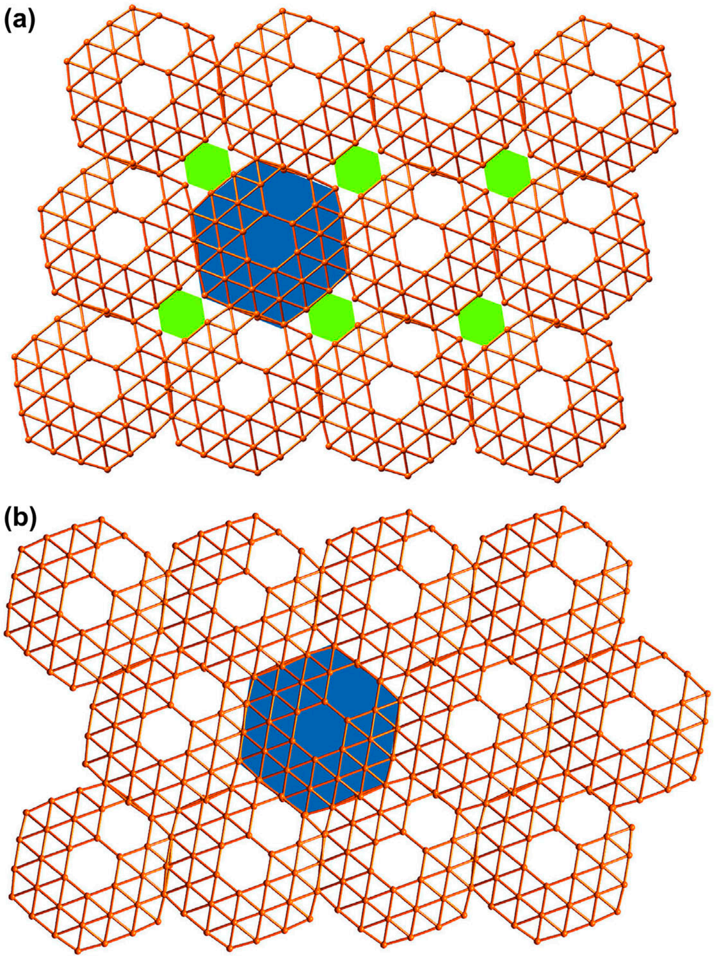

Figure 47. (Colour online) Schematics of building up borophenes with two different hexagonal hole patterns using the $B_{35}$ units [131]. The blue shaded area represents a single $B_{35}$ unit and the green area in (a) indicate monohexagonal holes created as a result of the arrangement of the $B_{35}$ units.

the quasi-planar structure. Isomer IV was a low-symmetry 3D structure. Both the double ring (V) and triple ring (XI) structures were found to be higher energy isomers. All other isomers were 2D with either pentagonal or hexagonal holes.

Isomers I and II gave the same simulated spectrum (Figure 48(b)), which was in good agreement with the experimental spectrum. The simulated spectrum of isomer III is shown in Figure 48(c) and it overlapped with the features of the global minimum. Isomer III could be weakly populated in the experiment and make minor contributions to the observed spectrum, on the bases of both the simulated spectrum and the relative energetics. Chemical bonding analyses using AdNDP are shown in Figure 50 for the closed-shell $B_{30}$ at the anion geometry. The $C_1$ $B_{30}$ consisted of seventeen 2c–2e localised peripheral $\sigma$ bonds, nineteen delocalised $\sigma$ bonds, and nine delocalised $\pi$ bonds.

Chirality is important in chemistry. The two chiral isomers of $B_{30}^-$ were independently found in the global minimum search. The chirality of the global minimum of

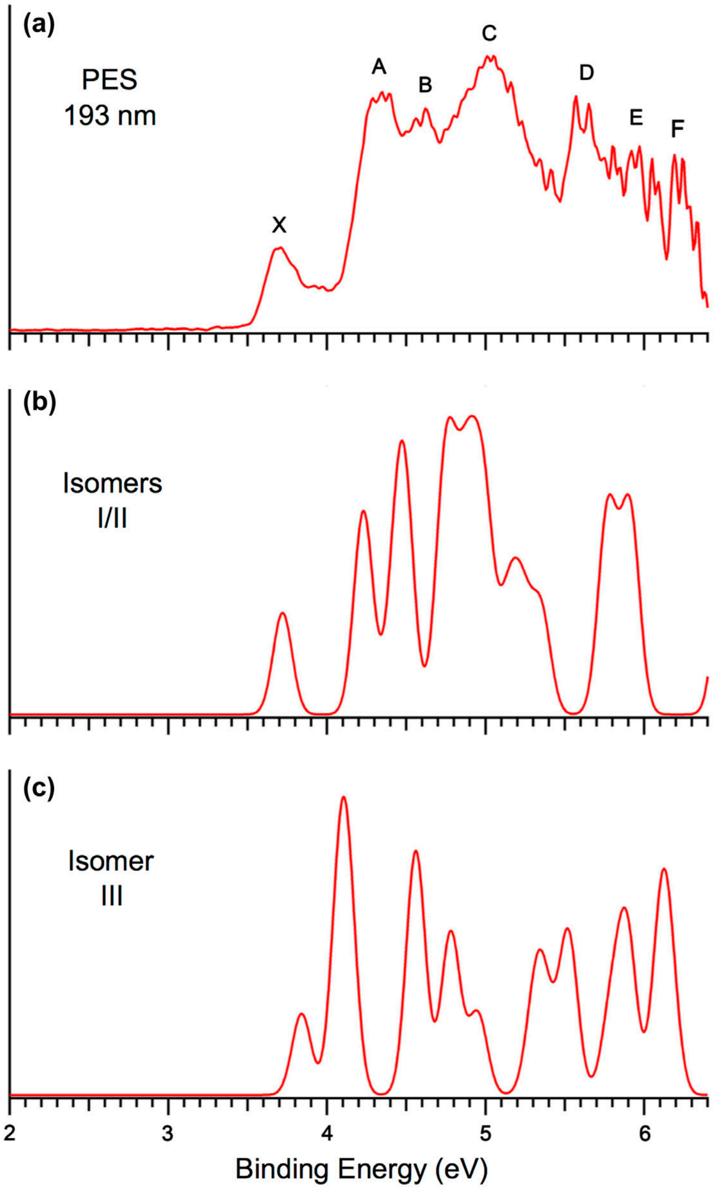

Figure 48. (Colour online) The photoelectron spectrum of $B_{30}^-$ at 193 nm (a), compared with the simulated spectra of the chiral global minimum of $B_{30}^-$ (b) and its low-lying isomer III (c) (see Figure 49) [130].

$B_{30}^-$ was due to the nonplanarity, because truly planar clusters or clusters with central symmetries could not be chiral. Figure 51 shows the barrier for the chiral transformation, involving the inversion of the nonplanar cluster. The chiral barrier was found to be 6.2 kcal/mol at the CCSD level of theory with a nearly planar transition state. This barrier was significant relative to the thermal energy at room temperature and thus the two chiral isomers could co-exist experimentally. A computational investigation by Tai

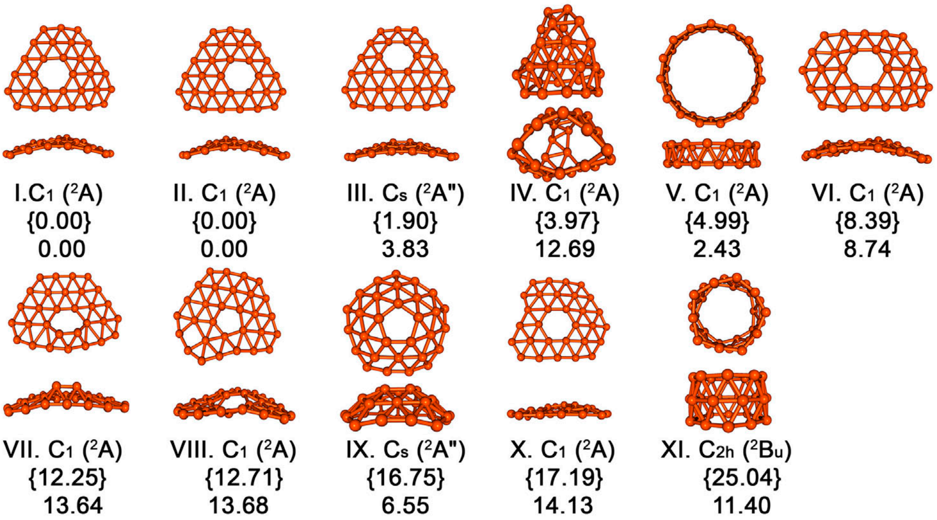

Figure 49. (Colour online) The global minimum and low-lying isomers of $B_{30}^{-}$ at PBE0 and LPNO–CCSD (in curly brackets) levels of theory. Note that isomers I and II are enantiomers of a chiral global minimum [130].

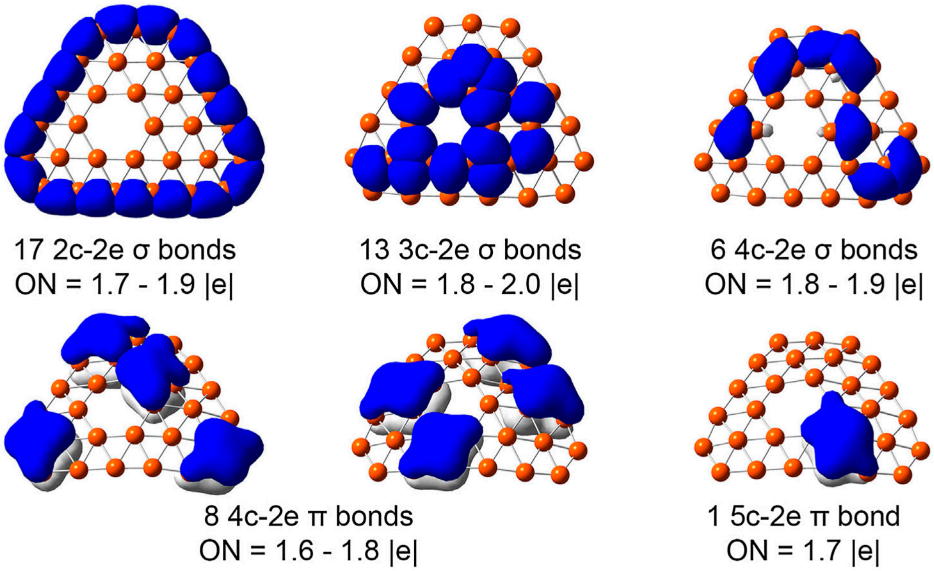

Figure 50. (Colour online) AdNDP analyses of the chemical bonding in the closed-shell $B_{30}$ global minimum. ON indicates the occupation number [130].

*et al.* found the global minimum of neutral $B_{30}$ had a bowl shape with a pentagonal hole [152], similar to isomer IX for the $B_{30}^{-}$ in Figure 49. Clearly, this isomer was a much higher energy structure in the anion.

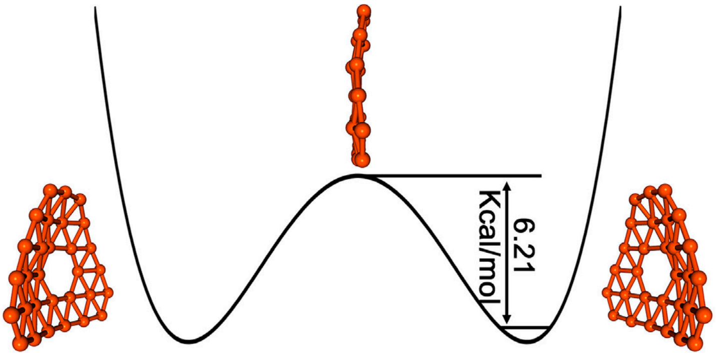

Figure 51. (Colour online) A schematic drawing of the potential energy curve for the chiral transformation between the two chiral enantiomers of $B_{30}^-$ via the bending coordinate [130].

## 7. All-boron cage clusters: borospherenes

In addition to the unusually low EA for $B_{36}$, the preliminary Figure 11 showed that $B_{40}$ had an even lower EA, suggesting a very stable electronic system for this cluster. Over the years, several structures were tested, mainly the tubular types, but none agreed with the experiment. The 40-atom boron cluster was finally solved after the solution of $B_{36}$ as a result of new global minimum search methods and increased computer powers through a multi-way experimental and theoretical collaborative effort [46].

### 7.1. ***$B_{40}^-$ and $B_{40}$: the first all-boron fullerene − borospherene***

#### 7.1.1. *PES and global minimum searches*

The photoelectron spectra of $B_{40}^-$ at two detachment photon energies are shown in Figure 52 [46]. The weak X' peak defined a very low EA of 2.50 eV for $B_{40}$. The weak intensity of this peak suggested that it might come from a weakly populated isomer, whereas the X band might represent the ground state transition for the main isomer of the $B_{40}^-$ anion. The global minimum of $B_{40}^-$ was searched using two methods independently, the TGmin code [45] and the stochastic surface walking (SSW) method [153]. A total of 5300 structures were searched for $B_{40}^-$ by TGmin and 3565 structures by SSW. Similar searches were performed for neutral $B_{40}$ using TGmin and SSW. Figure 53 displays the configurational energy spectra within 1.5 eV of the global minimum for both $B_{40}^-$ and $B_{40}$ at the PBE0 level of theory. The structures of the global minima and selected isomers are given. In general, three types of structures were found: quasi-planar, 3D cage, and tubular structures (Figure 53(a)). The global minimum of $B_{40}^-$ was a quasi-planar structure with a DHV, similar to that of $B_{35}^-$ (Figure 45). Most interestingly, the second isomer of $B_{40}^-$ was a cage structure only 0.1 eV above the DHV planar global minimum. The third isomer was a quasi-planar structure, similar to $B_{36}^-$ (Figure 40). The fourth isomer was also a cage structure, while the fifth isomer was planar, featuring a heptagon. $B_{40}^-$ was the first boron cluster, where a heptagonal hole appeared in a low-lying 2D isomer.

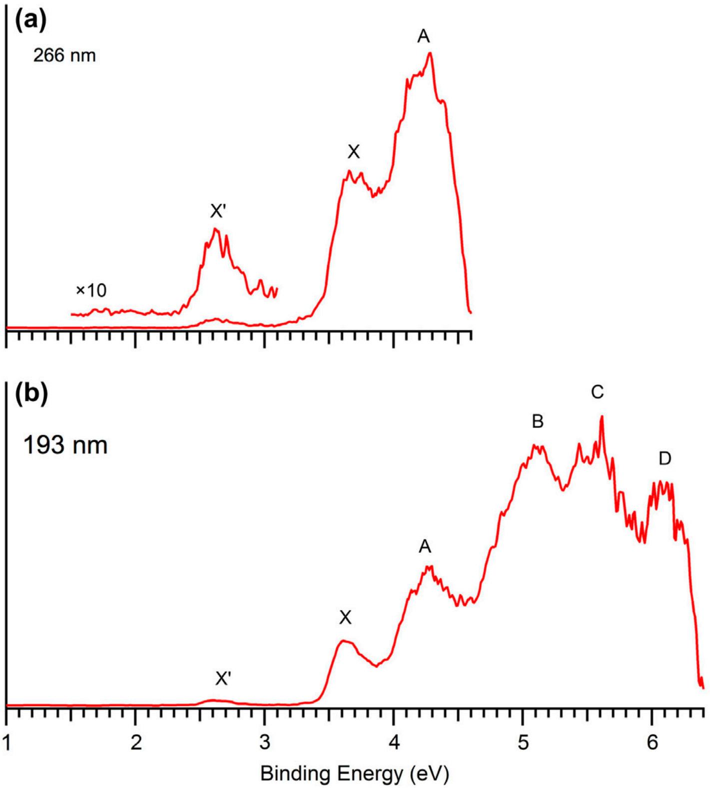

Figure 52. (Colour online) Photoelectron spectra of $B_{40}^-$ at (a) 266 nm and (b) 193 nm [46].

### 7.1.2. *Experimental confirmation and characterisation of the first all-boron fullerene*

The simulated spectrum of the DHV global minimum was compared with the experiment in Figure 54. The DHV global minimum gave very high electron binding energies and its simulated spectrum was in good agreement with the intense PES features (X, A−D). The cage isomer was very close to the DHV global minimum in energy and could be populated experimentally. The simulated spectrum of the cage structure was shown in Figure 54(c). The cage structure exhibited a very large HOMO-LUMO gap and a very low electron binding energy for its first detachment feature, in excellent agreement with the weak PES band (X’) at the low binding energy side. The higher binding energy detachment features of the cage isomer overlapped with the PES bands of the DHV global minimum. The combination of the two lowest-energy isomers was in perfect agreement with the experiment, providing considerable credence for the global minimum of $B_{40}^-$ and its low-lying cage isomer.

There was a re-ordering of the different isomers in neutral $B_{40}$ (Figure 53(b)). In the neutral, the cage structure was the global minimum and was overwhelmingly stable. The lowest isomer of $B_{40}$ was also a cage 0.5 eV higher in energy, whereas the DHV isomer was about 1 eV higher in energy in the neutral. The detailed structures of the DHV global minimum and the cage isomer are shown in Figure 55 for both the anion and the neutral species. There was relatively little structural change between the anions

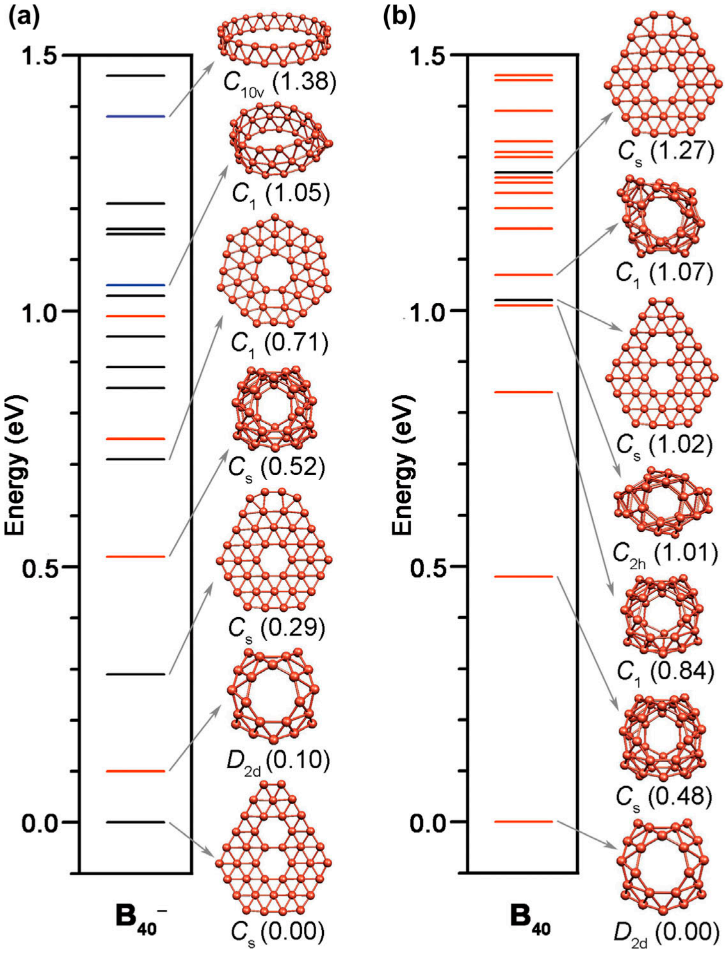

Figure 53. (Colour online) The configurational energy spectra of (a) $B_{40}^{-}$ and (b) $B_{40}$ at the PBE0 level of theory. The global minima and structures of selected isomers are shown [46]. Note the overwhelming stability of the $D_{2d}$ cage for neutral $B_{40}$.

and the neutrals of the two isomers. The DHV isomer had $C_s$ symmetry with a slight bowl shape.

The cage structure had $D_{2d}$ symmetry, with two hexagons and four heptagons with an overall shape akin to a Chinese red lantern. The cage structure was unprecedented for boron clusters. Even though a $B_{80}$ cage was suggested computationally previously [154], subsequent calculations showed that it was energetically unfavourable in comparison with other low-symmetry more closed packed structures [155–158]. The $B_{40}$ cage had a diameter of 6.2 Å, compared to the 7.1 Å diameter for the fullerene $C_{60}$ [64]. The $B_{40}^{-}$ cage was the first all-boron fullerene to be observed and characterised experimentally. A name, ‘borospherene’, was coined for the all-boron fullerene [46].

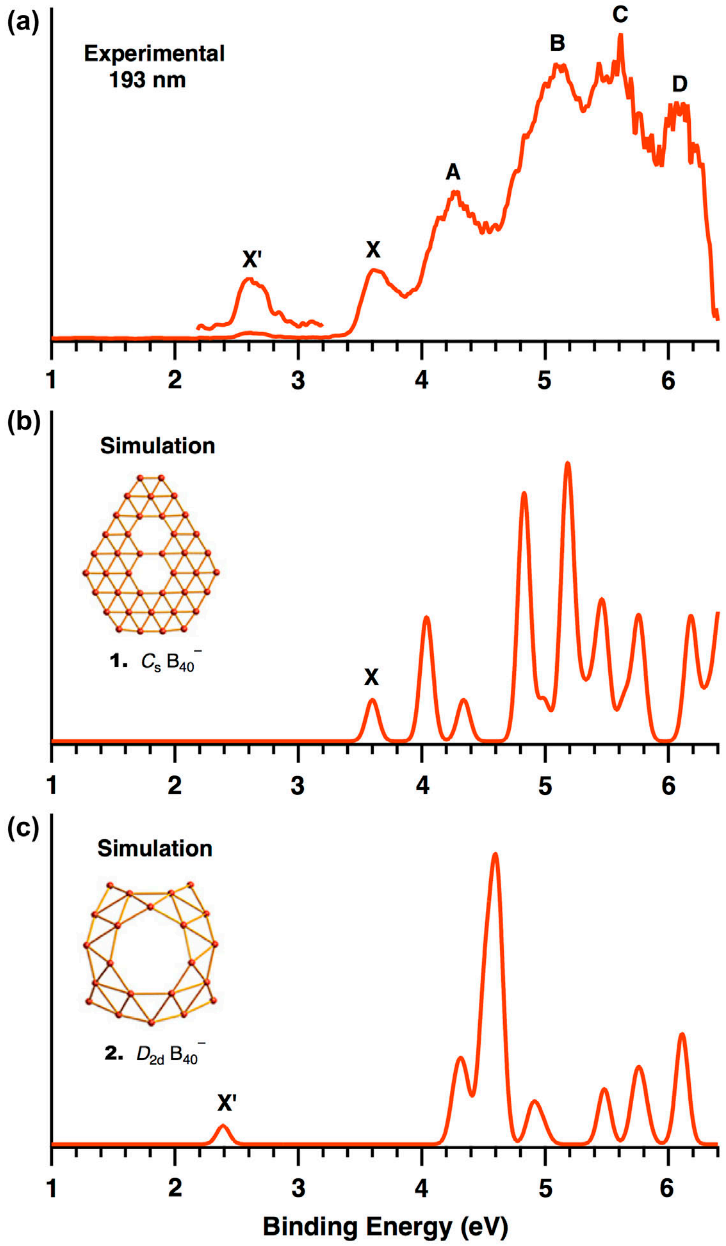

Figure 54. (Colour online) Comparison of the simulated spectra of the global minimum planar $B_{40}^-$ (b) and the $D_{2d}$ borospherene cage (c) with the experimental spectrum [46].

### 7.1.3. *The electronic structure, chemical bonding, and stability of the $B_{40}$ borospherene*

The low binding energy PES feature (X') for the $B_{40}^-$ cage implied a large HOMO-LUMO gap for the neutral species, as was borne out by the simulated spectrum (Figure 54(c)). The frontier MOs of the $B_{40}$ cage is shown in Figure 56, with a computed HOMO–LUMO gap of 3.13 eV at the PBE0 level, suggesting the $B_{40}$

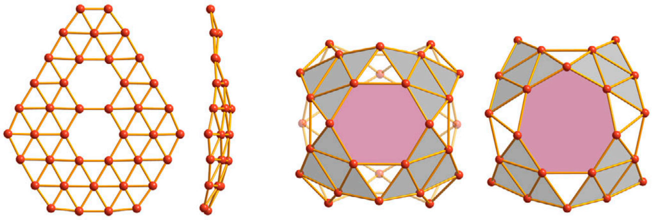

**1.** $C_s$ $B_{40}^-$ ($^2A'$)  **2.** $D_{2d}$ $B_{40}^-$ ($^2B_2$)

**3.** $C_s$ $B_{40}$ ($^1A'$)  **4.** $D_{2d}$ $B_{40}$ ($^1A_1$)

Figure 55. (Colour online) More detailed top and side views of the two lowest energy structures of $B_{40}^-$ and the corresponding neutrals [46]. The shades in the cage structures were for easier viewing.

borospherene was an extremely stable electronic system. The large HOMO–LUMO gap implied that the extra electron in its anion would be in a much higher energy orbital, making it less stable as an anion, which explained the reverse of stability in the anion between the cage and the DHV isomers (Figure 53). The LUMO of the $B_{40}$ borospherene was a nondegenerate orbital of $b_2$ symmetry (Figure 56). Occupation of the LUMO in the anion gave rise to the $^2B_2$ electronic state (**2** in Figure 55) for the anion with the same $D_{2d}$ symmetry as the neutral, resulting in little structural change. Zeng and co-workers recently studied the electronic and vibrational absorption spectra of the $B_{40}$ borospherene [159]. Their computed electronic absorption threshold of 1.96 eV, corresponding to the HOMO → LUMO transition, was in good agreement with the separation of the first and second simulated PES bands in Figure 54(c).

The chemical bonding of borospherene was analysed using AdNDP, as shown in Figure 57. There were forty 3c–2e and eight 6c–2e $\sigma$ bonds, which basically corresponded to a multi-centre $\sigma$ bond for each of the forty-eight $B_3$ triangles on the borospherene surface. There were twelve delocalised $\pi$ bonds, leaving no localised bonds in borospherene. Both the $\sigma$ and $\pi$ bonds were uniformly distributed over the borospherene surface, resulting in the extraordinarily stable electronic structure for borospherene.

The stability of the $B_{40}$ borospherene was further studied using molecular dynamics (MD) simulations [46], as shown in Figure 58. The MD simulations showed that the $B_{40}$ borospherene was highly robust even at high temperatures, dynamically stable at 700 and 1000 K for the 30 ps duration used in the simulation (Figure 58). Merino and co-workers carried out more detailed MD simulations and found that the $B_{40}$ borospherene was fluxional above 1200 K [160]. They observed continuous conversions between the hexagonal and heptagonal rings on the borospherene surface with an activation barrier of 14.3 kcal/mol. They concluded that below 1000 K, borospherene behaved as a solid, consistent with the MD simulations in Figure 58. Between 1200 and 1500 K, borospherene could be described as a 2D liquid-like system due to the continuous conversion between the hexagonal and heptagonal rings on the cage surface. Hence, under high temperatures the $B_{40}$ borospherene behaved like a spherical 2D liquid or a nanobubble [160].

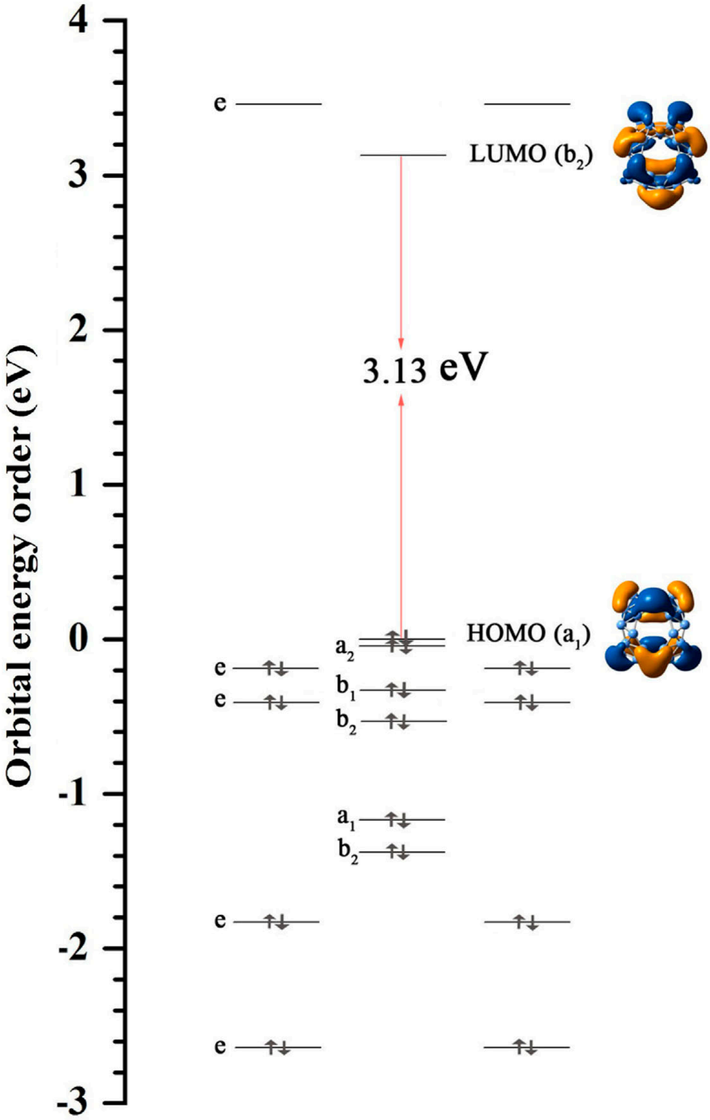

Figure 56. (Colour online) The frontier MO energy levels of the $D_{2d}$ $B_{40}$ cage. The contours of the HOMO and LUMO and the HOMO-LUMO gap are indicated [46].

### 7.1.4. *The electronic structure and chemical bonding of the planar isomer of $B_{40}$ and its charge-state-dependent stability*

The DHV planar global minimum of $B_{40}^-$ was also extremely interesting. It was shown above that the reverse of stability between this structure and the borospherene cage in the anion and neutral states was due to the large HOMO–LUMO gap of the cage, that resulted in a very small EA for borospherene. It was also due to the fact that the DHV structure had a small HOMO–LUMO gap with a very large EA, as could be seen from the small separation between the first and second simulated PES bands in Figure 54(b).

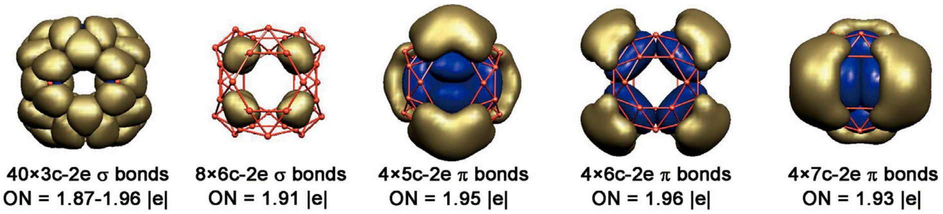

Figure 57. (Colour online) AdNDP analyses of the chemical bonding of the $B_{40}$ all-boron fullerene [46]. ON indicates the occupation number.

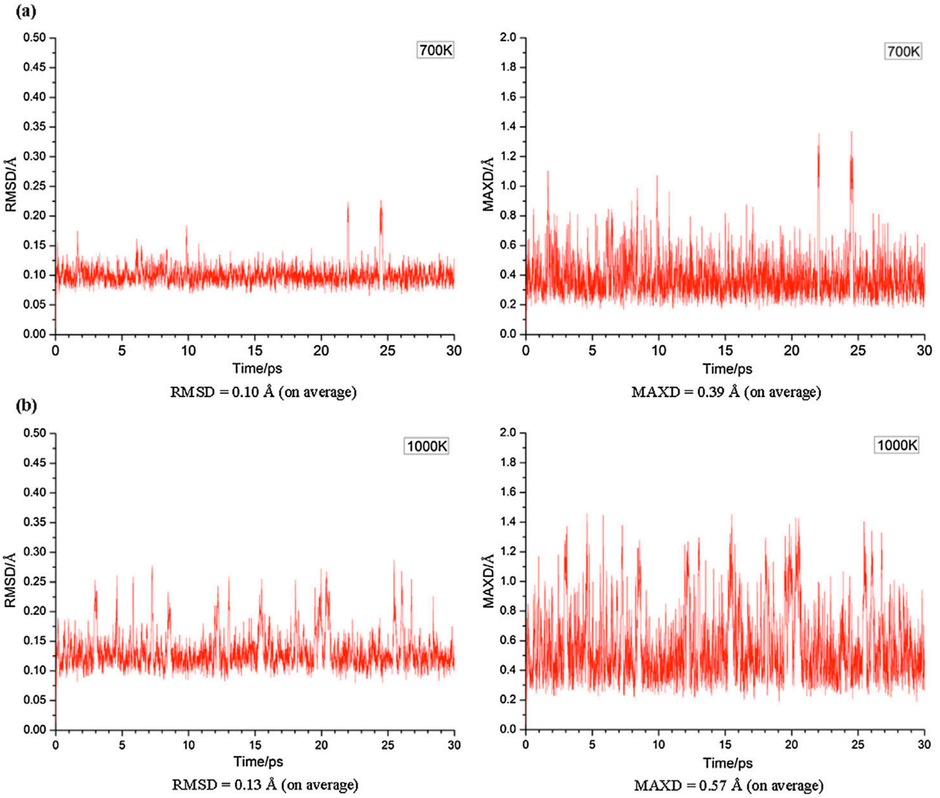

Figure 58. (Colour online) Born-Oppenheimer molecular dynamics simulations of the $B_{40}$ borospherene at (a) 700 K and (b) 1000 K for 30 ps using the CP2 K software suite (http://cp2 k.berlios.de/). The root-mean-square-deviation (RMSD) and maximum bond length deviation (MAXD) values on average are given in angstrom [46].

The measured EA of 3.51 eV for the DHV structure was higher than that of borospherene (2.50 eV) by 1 eV. This difference in their EAs directly led to the near degeneracy of the two structures in the anions, because the DHV isomer was much higher in energy as a neutral. The energetic relationships between the different charge states are shown in Figure 59. Remarkably, because of the smaller HOMO–LUMO gap of the DHV isomer and its high EA, the addition of a second electron led to an extremely stable DHV $B_{40}^{2-}$ dianion with a positive second EA of 0.68 eV (Figure 59). This was also an extraordinary result, suggesting that the closed shell DHV $B_{40}^{2-}$ was a thermodynamically stable species. Naturally, the filling of a second electron to the high energy LUMO of borospherene led to a much less stable $B_{40}^{2-}$ borospherene cage (Figure 59).

The chemical bonding of the DHV 2D structure of $B_{40}$ was also interesting. The $\pi$ bonding pattern of the planar $B_{40}^{-}$ was found to be similar to the $C_{27}H_{23}{}^{+}$ PAH molecule [161], as shown in Figure 60. The AdNDP analyses showed more clearly the analogy between the $\pi$ bonding in the closed-shell DHV $B_{40}^{2-}$ and the closed-shell $C_{27}H_{23}{}^{+}$ PAH, as displayed in Figure 61, extending the hydrocarbon analogy to the largest 2D boron cluster thus far.

### 7.1.5. *The competition between the cage and the planar structures as a function of boron cluster size*

In addition to the proposed $B_{80}$ cage, various smaller boron cages had been considered computationally [162–167]. To provide further insight into the stability of the $B_{40}$ borospherene, its cohesive energy ($E_{coh}$) at the PBE0 level of theory was compared with selected neutral boron clusters in Figure 62. As expected, the cohesive energies of the 2D boron clusters increased monotonically with the cluster size from $B_7$ to $B_{40}$. Interestingly, low-lying cage-like structures started to emerge at $B_{32}$. The cage isomers for $B_{32}$ and $B_{36}$ were found to be less stable than their respective 2D structures by 0.028 eV/atom and 0.081 eV/atom, respectively. The crossover was estimated to be at $B_{38}$. The $B_{40}$ fullerene was overwhelmingly more stable than the 2D structure, even

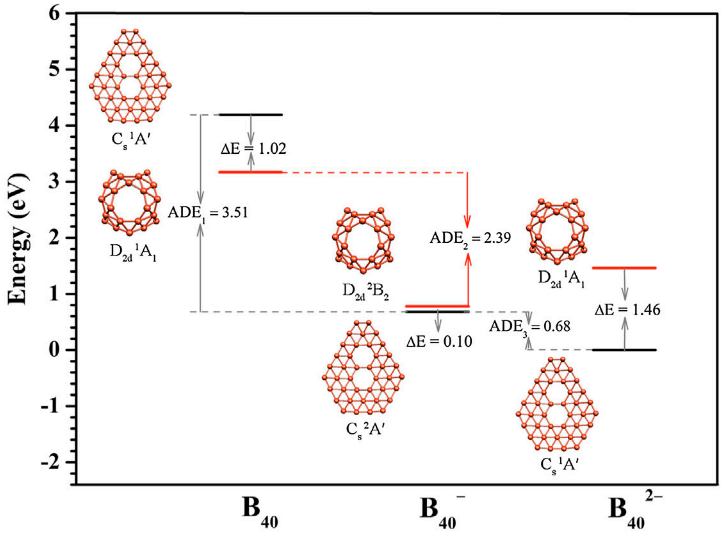

Figure 59. (Colour online) Comparison of the relative stabilities (ΔE) of the $C_s$ planar and the $D_{2d}$ cage structures of $B_{40}$ at different charge states at the PEB0 level of theory. The computed ADEs of the $C_s$ $B_{40}^{-}$ ($ADE_1$), the $D_{2d}$ $B_{40}^{-}$ ($ADE_2$), and the first ADE of the $C_s$ $B_{40}^{2-}$ ($ADE_3$) are given. Note that the $C_s$ $B_{40}^{2-}$ dianion was predicted to be a thermodynamically stable species [46].

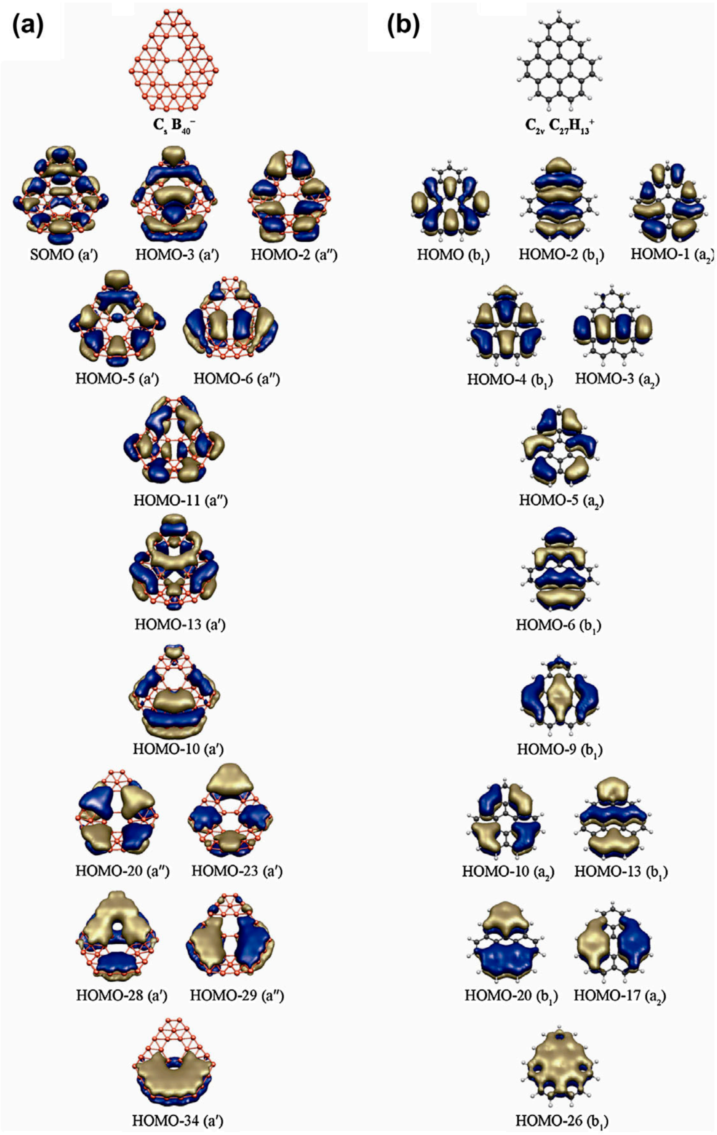

Figure 60. (Colour online) Comparison of the $\pi$ MOs of (a) the $C_s$ $B_{40}^-$ and (b) the $C_{27}H_{13}^+$ PAH molecular ion [46]. The singly occupied MO of $B_{40}^-$ is labelled as SOMO.

though for the $B_{40}^-$ anion the 2D structure was slightly more stable than the cage structure (Figure 53).

Recently, Lv *et al.* reported that the $B_{38}$ cluster had a cage global minimum at the PBE0, PBE, and MP2 levels of theory [168]. A DHV 2D isomer, similar to the DHV $B_{40}^-$ global minimum, was only 0.21 and 0.02 eV above the cage structure at PBE0 and PBE, respectively. However, a subsequent comment by Tai *et al.* showed that the relative energies between the cage and DHV isomers were method-dependent [169]. At the TPSSH level of theory, the cage isomer was higher in energy than the DHV isomer

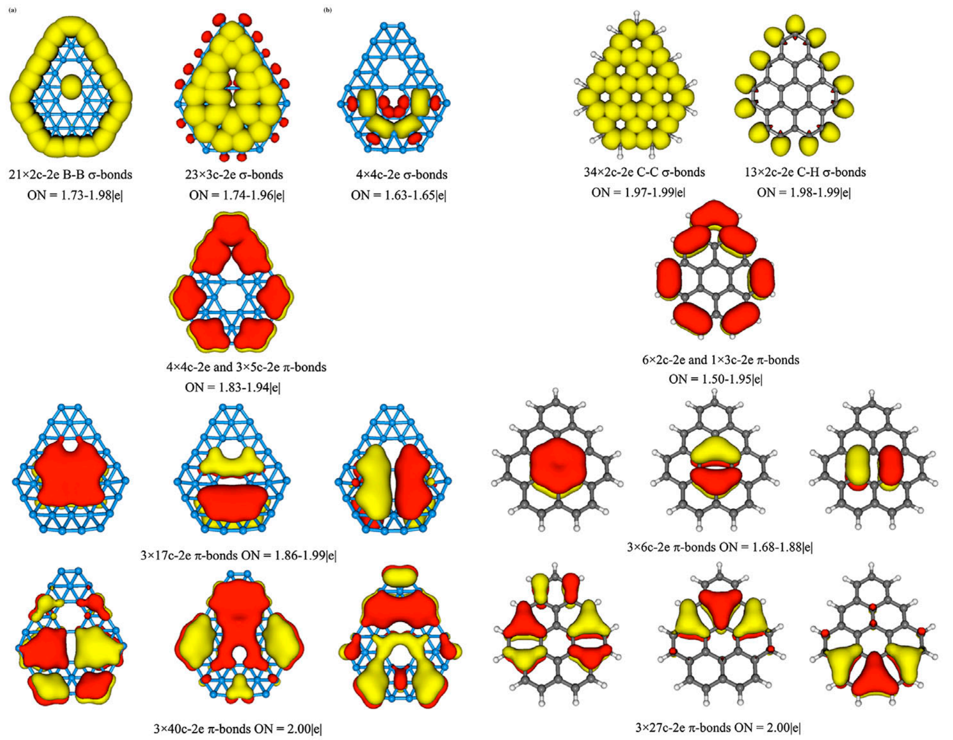

Figure 61. (Colour online) Comparison of the AdNDP bonding analyses for (a) the closed-shell $C_s$ $B_{40}^{2-}$ and (b) the closed-shell $C_{27}H_{13}^{+}$ PAH molecular ion [46].

by 0.34 eV, whereas at the CCSD(T) level the cage was nearly degenerate with the DHV isomer, only 0.02 eV higher in energy. These results were consistent with the data shown in Figure 62, where the 2D and cage crossed over at $B_{38}$. It should be noted that Figure 62 showed the slopes of the cage and 2D cohesive energy curves were different. In fact, the gap between the 2D and cage isomers was closing from $B_{36}$ to $B_{32}$. Extrapolating that trend, one would find that the two cohesive energy curves would cross at $B_{27}$ or $B_{28}$ again, where the cohesive energy of the cage would be equal to or larger than the 2D isomers. Interestingly, Zhao *et al.* recently reported a cage structure as the global minimum for $B_{28}$, whereas a 2D isomer was nearly degenerate with the cage, only 0.029 eV higher in energy [170], exactly as Figure 62 anticipated. Clearly, the competition between the different structural types is complicated and is not a simple function of size. There is experimental evidence that the cage isomer is present in the photoelectron spectrum of $B_{28}^{-}$ as a minor species in a very recent study[171].

The large volume inside the $B_{40}$ borospherene suggested that it could host additional atoms [46], similar to endohedral fullerenes [172,173]. Indeed, endohedral borospherenes have been investigated recently. Jin *et al.* have reported calculations of $M@B_{40}$ (M = Sc, Y, La) [174]. They found that the metal atoms tended to locate off centre, similar to the $M@C_{82}$ endohedral fullerene family [173]. They further calculated the dimerisation of $M@B_{40}$ and their IR and NMR spectra. Bai *et al.* reported calculations on the doping of the $B_{40}$ borospherene with alkali earth elements and found that

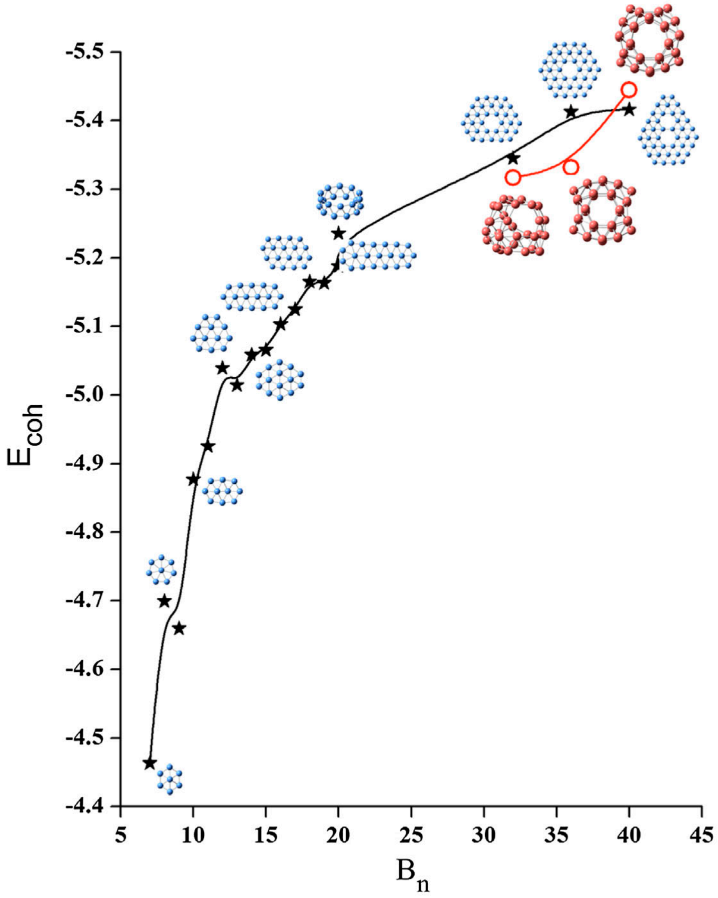

Figure 62. (Colour online) The cohesive energies per atom for $B_n$ ($n = 7-40$) clusters computed at the PBE0 level of theory. The black stars stand for the planar or double ring ($B_{20}$) structures of $B_n$. The red circles stand for the cage structures of $B_{32}$, $B_{36}$, and $B_{40}$. The lines are drawn to guide the eyes [46].

Ca and Sr stay in the centre of the borospherene, while Be and Mg favour exohedral doping [175].

## 7.2. *$B_{39}^-$: a chiral borospherene*

### 7.2.1. *PES and global minimum searches*

The cohesive energy curves shown in Figure 62 suggested that the global minimum of $B_{39}^-$ might be a cage structure. However, the photoelectron spectrum of $B_{39}^-$ was quite complicated, posing considerable challenges for comparison with theory. The spectrum of $B_{39}^-$ at 193 nm is shown in Figure 63(a) [132]. Its electron binding energies were considerably higher than that of $B_{40}^-$. The spectrum was congested with numerous unresolved features, suggesting the possibility of co-exiting isomers in the cluster beam. Global minimum searches for $B_{39}^-$ were done using the minimum-hopping and TGmin methods independently. Initial structures for the minimum-hopping searches were primarily based on the $B_{40}$ cage structure by removing one boron atom from different positions of the borospherene surface, as well as manual structural constructions. About 5000 isomers were found from eight independent minimum-hopping searches. Many cage-like structures were found to be among the low-lying isomers, along with 2D and tubular type isomers. More than 4600 isomers were produced independently using the TGmin code. The low-lying isomers within 0.5 eV of the global minimum are shown in Figure 64 at the CCSD(T) level of theory.

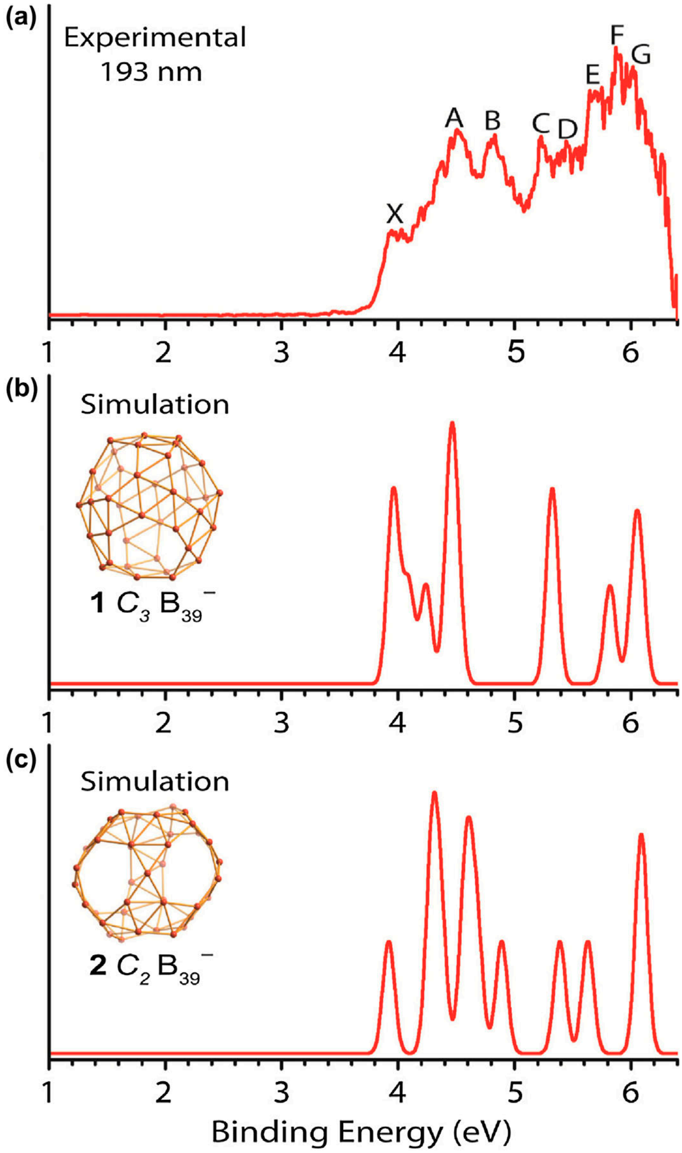

Figure 63. (Colour online) The photoelectron spectrum of $B_{39}^-$ at 193 nm (a), compared with the simulated spectra of the $C_3$ global minimum of $B_{39}^-$ (b) and its $C_2$ low-lying isomer (c) [132].

Figure 65 shows in more detail the global minimum $C_3$ cage structure of $B_{39}^-$ at the CCSD(T) level and the second lowest-lying $C_2$ cage isomer, which is only 0.08 eV above the $C_3$ isomer. It was found that both the $C_3$ and $C_2$ cage isomers were axially chiral and their enantiomers are also shown in Figure 65, where the hexagonal and heptagonal rings are shaded for better structural viewing. The degenerate global minima $C_3$(**1**) and $C_3$(**1'**) formed a pair of axially chiral enantiomers with respect to the $C_3$ symmetry axis; the $C_2$(**2**) and $C_2$(**2'**) isomers formed a pair of axially chiral enantiomers about the $C_2$ symmetry axis. Among the first ten most stable isomers at the CCSD(T) level (Figure 64), there were five additional low-symmetry cages: $C_1$(**3**), $C_1$(**5**), $C_1$(**6**), $C_2$(**8**), and $C_1$(**10**), which were all chiral in nature. The first non-cage isomer had a slightly distorted tubular structure (**4** in Figure 64). The first quasi-planar isomer (**7**, $C_s$) was 0.28 eV above the global minimum at CCSD(T) and it was similar to the hexagonal $B_{36}^-$ cluster by attaching three B atoms along one edge (Figure 40). Another quasi-planar isomer (**9**, $C_s$) had a central heptagonal hole.

The simulated spectrum for the $C_3$ global minimum (Figure 63(b)) was compared with the experiment in Figure 63 and was in agreement with some of the observed features. Clearly, other isomers must be populated experimentally and contributed to the observed spectrum. The simulated spectrum of the low-lying $C_2$ isomer is shown in Figure 63(c). The combination of the two isomers agreed well with the experiment.

### 7.2.2. *The structure and bonding of the $B_{39}^-$ chiral borospherene*

The structure and bonding of the chiral $C_3$(**1**) and $C_2$(**2**) cage structures of $B_{39}^-$ were related to those of the $B_{40}$ borospherene. The $C_3$(**1**) $B_{39}^-$ could be constructed from the $B_{40}$ cage by replacing a $B_7$ heptagon with a $B_6$ hexagon, followed by a structural rearrangement. Hence, the $C_3$ cage consisted of three heptagons on the top half and three hexagons on the bottom half, as well as forty-seven triangles. It had a closed-shell electronic structure with a large HOMO–LUMO gap of 2.89 eV at the PBE0 level, compared with the 3.13 eV gap of $B_{40}$ at the same level of theory. The $C_2$(**2**) $B_{39}^-$ cage could be obtained from the $B_{40}$ borospherene by removal of one B atom on the waist, so that one of the boron double chain on the waist was narrowed to a single atom to cause a 'defect' site (Figure 65). Thus, the $C_2$ cage had the same numbers of hexagons and heptagons as the $B_{40}$ borospherene, as well as forty-six triangles. It also had a sizable HOMO–LUMO gap of 2.73 eV.

The chemical bonding of the $C_3$ and $C_2$ $B_{39}^-$ borospherenes was analysed using AdNDP, as shown in Figure 66. The $C_3$ cage possessed thirty-nine 3c–2e and eight 6c–2e $\sigma$ bonds (Figure 66(a)). For the 6c–2e $\sigma$ bonds, the central $B_3$ triangles made major contributions. Thus, all forty-seven $\sigma$ bonds were practically 3c–2e $\sigma$ bonds, covering the cage surface uniformly with one multi-centre $\sigma$ bond for each $B_3$ triangle. The remaining 12 bonds formed the delocalised $\pi$ framework. The three 6c–2e and three 5c–2e $\pi$ bonds were associated with the top and bottom $B_6$ triangles perpendicular to the $C_3$ symmetry axis, respectively. The six 6c–2e $\pi$ bonds on the waist cover the zigzag double chain between the top and bottom $B_6$ triangles. Thus, all the 118 valence electrons in the $C_3$ $B_{39}^-$ borospherene were evenly delocalised over the cage surface in both the $\sigma$ and $\pi$ frameworks, which effectively compensated for boron's intrinsic electron deficiency. This bonding pattern was similar to that in the $B_{40}$ borospherene (Figure 57) and seemed to be critical for the high stability of borospherenes. Because of the less symmetric $C_2$ cage, an unusual 5c–2e $\sigma$ bond was found (Figure 66(b)). It could be approximately viewed as a B 2p lone-pair. Other than that, the bonding

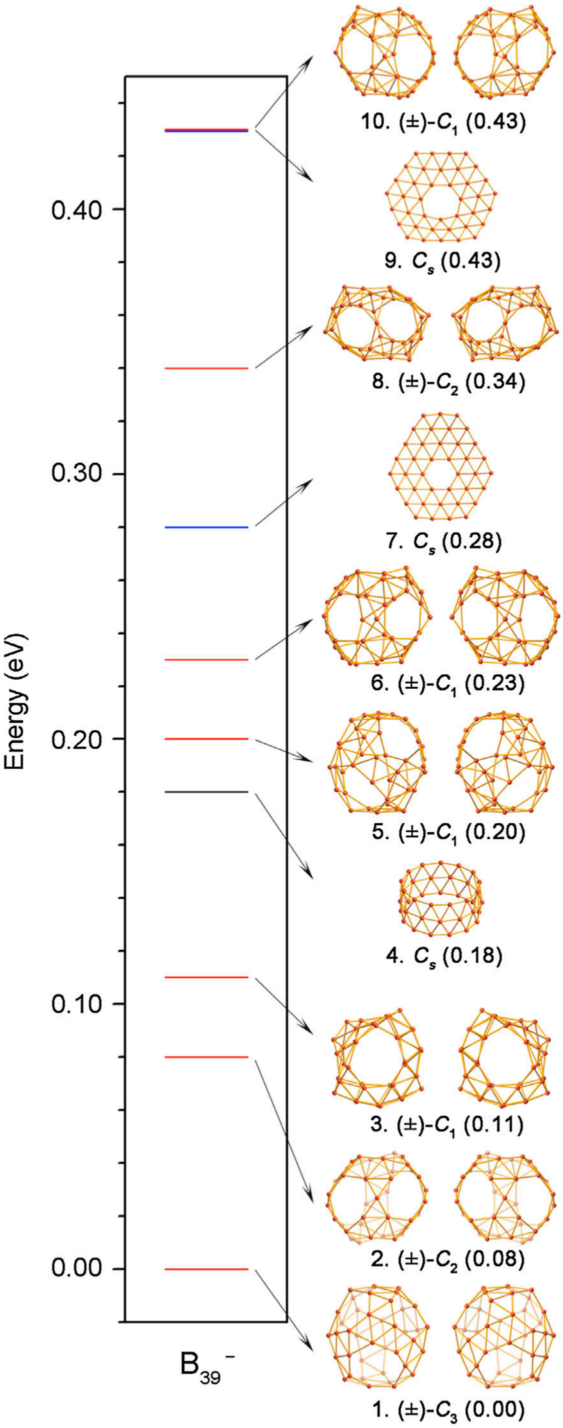

Figure 64. (Colour online) The global minimum and low-lying isomers of $B_{39}^-$ within 0.45 eV of the global minimum [132].

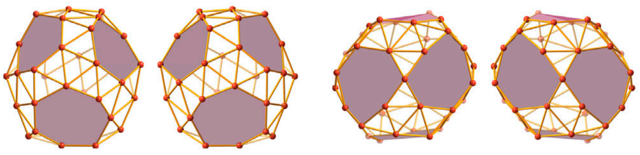

**1** $C_3$ $B_{39}^-$ ($^1A$) **1'** $C_3$ $B_{39}^-$ ($^1A$) **2** $C_2$ $B_{39}^-$ ($^1A$) **2'** $C_2$ $B_{39}^-$ ($^1A$)

Figure 65. (Colour online) Detailed structures of the global minimum of the chiral $C_3$ $B_{39}^-$, its low-lying chiral $C_2$ isomer, and their respective enantiomers. The shades are for easier viewing [132].

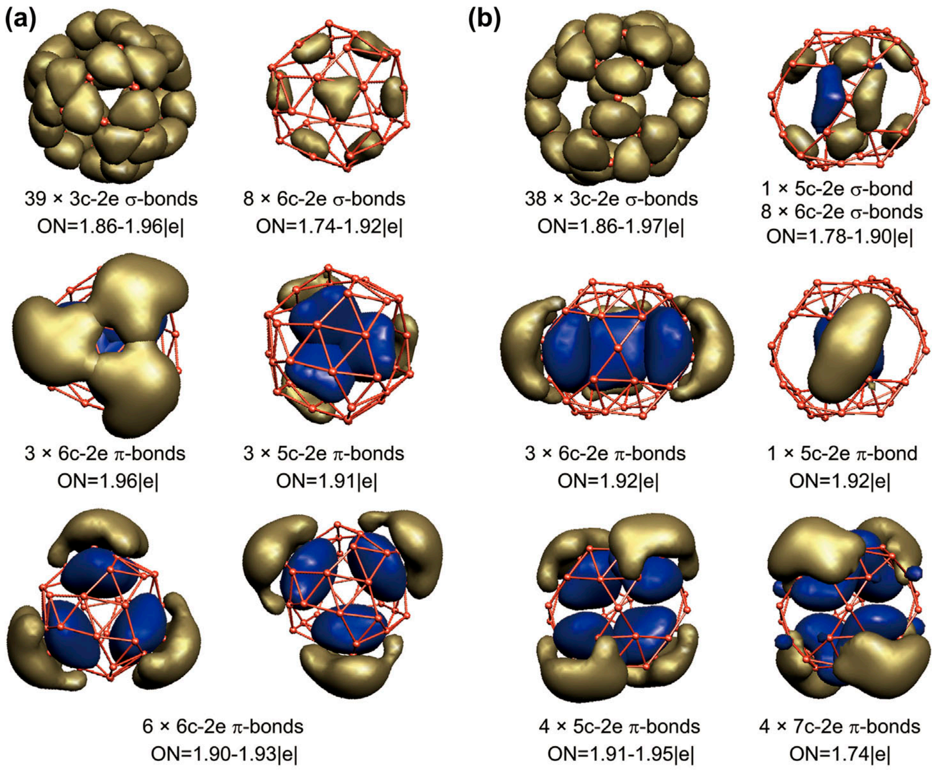

Figure 66. (Colour online) AdNDP bonding analyses for (a) the global minimum $C_3$ $B_{39}^-$ and (b) the low-lying $C_2$ isomer [132]. ON indicates the occupation number.

pattern in the $C_2$ $B_{39}^-$ borospherene was similar to that in the $C_3$ isomer. The twelve delocalised $\pi$ bonds found in the $B_{40}$ cage seemed to be characteristic of borospherenes, and they were well maintained in both the $C_3$ and $C_2$ cages of $B_{39}^-$.

Chen *et al.* reported recently a computational study of $B_{41}^+$ and $B_{42}^{2+}$ and found that these boron cluster cations had cage structures with $\pi$ bonding patterns also similar to the $B_{40}$ borospherene [176]. The $B_{41}^+$ borospherene had $C_1$ symmetry and the $B_{42}^{2+}$ borospherene had $C_2$ symmetry. Hence, both were chiral like $B_{39}^-$. Chen *et al.* further considered doping of the $B_{39}^-$ cage by $Ca^{2+}$ to form $Ca@B_{39}^+$ endohedral borospherenes [177]. There appeared to be a family of borospherenes for mid-sized boron clusters, similar to the fullerene family. Large boron cages beyond $B_{80}$ have also been considered computationally [158,164,178–184], but they are unlikely to be the global minimum on the potential energy surfaces.

## 8. Summary and concluding remarks

Since the last comprehensive review in 2006 [28], significant progresses have been made in our understanding of boron clusters by combining PES of size-selected boron clusters with computational chemistry. Boron seems to be the ultimate ‘rule breaker’, not only in its bulk forms, but also in the nanoscale. Even with the extensive experimental and theoretical efforts, no rules or construction principles can be derived to predict the structures or growth of boron clusters. Each cluster has its own characteristics and requires the greatest care in global minimum searches and careful comparison with experimental data in order to make reliable conclusions about the most stable structures. That being said, a few general observations can still be made. The planarity of boron clusters as anions persists up to $B_{40}^-$, where both a 2D structure and the borospherene cage compete for the global minimum, despite the fact that the borospherene cage was the overwhelmingly stable form for neutral $B_{40}$. Most 2D boron clusters do not have perfect triangle lattices and contain various ‘defects’ or ‘vacancies’. The size of the defects seems to increase with the cluster size from tetragonal to even heptagonal holes appearing in low-lying 2D structures of the large boron clusters. Heptagonal rings are rare in fullerenes [184–186], but they are common in borospherenes. The $\pi$ bonding patterns of the 2D boron clusters continue to be found to be similar to PAH molecules, extending the all-boron hydrocarbon analogues to $B_{40}^-$: its 2D isomer with a DHV was found to have $\pi$ bonding patterns similar to the $C_{27}H_{13}{}^+$ PAH cation.

The discovery of the 2D hexagonal $B_{36}$ cluster was a significant breakthrough in our understanding of boron clusters, providing indirect experimental evidence for the viability of atom-thin boron nanosheets or borophenes. The discovery of the first all-boron fullerene in $B_{40}^-$ and $B_{40}$ was a major landmark in the study of boron clusters. It seems that there may be a family of borospherenes in the mid-size range, parallel to the fullerene family. These momentous findings have been tremendously exciting and have stimulated renewed interests in boron clusters and nanostructures. It is conceivable that the pace of discovery will continue to accelerate in boron clusters and more interesting structures and chemical bonds will be uncovered with increasing experimental and computational sophistication, laying the foundation for novel boron nanostructures.

## Disclosure statement

No potential conflict of interest was reported by the author.

## Funding

The experimental work on boron clusters at Brown University was supported by the National Science Foundation, Division of Materials Research [grant number DMR-0904034]; and Division of Chemistry [grant number CHE-1263745].

## Acknowledgements

This review summarises collaborative researches with several outstanding theoretical colleagues over more than a decade, including Prof. Alexander I. Boldyrev from Utah State University, Prof. Jun Li from Tsinghua University, Prof. Si-Dian Li from Shanxi University, and Prof. Xiao Chen Zeng from University of Nebraska-Lincoln. I am indebted to them and their group members for the fruitful collaborations. I would also like to thank many current and former group members for their contributions, specifically, Dr Hua-Jin Zhai, and Dr Constantin Romanescu, Dr Wei Huang, Dr Wei-Li Li, and Dr Zachary Piazza. I am also grateful to Dr Andre Fielicke for the collaboration on the two-color IR/UV experiment to probe the structures of neutral boron clusters.

## References

[1] W.N. Lipscomb, Science. **196**, 1047–1055 (1977).

[2] B. Albert and H. Hillebrecht, Angew. Chem. Int. Ed. **48**, 8640–8668 (2009).

[3] A.R. Oganov and V.L. Solozhenko, J. Superhard Mater. **31**, 285–291 (2009).

[4] L. Hanley, J.L. Whitten, and S.L. Anderson, J. Phys. Chem. **92**, 5803–5812 (1988).

[5] S.A. Ruatta, L. Hanley, and S.L. Anderson, J. Chem. Phys. **91**, 226–239 (1989).

[6] P.A. Hintz, S.A. Ruatta, and S.L. Anderson, J. Chem. Phys. **92**, 292–303 (1990).

[7] P.A. Hintz, M.B. Sowa, S.A. Ruatta, and S.L. Anderson, J. Chem. Phys. **94**, 6446–6458 (1991).

[8] M.B. Sowa-Resat, J.S. Smolanoff, A. Lapicki, and S.L. Anderson, J. Chem. Phys. **106**, 9511–9522 (1997).

[9] S.J.L. Placa, P.A. Roland, and J.J. Wynne, Chem. Phys. Lett. **190**, 163–168 (1992).

[10] S.J. Xu, J.M. Nilles, D. Radisic, W.J. Zheng, S. Stokes, K.H. Bowen, R.C. Becker, and I. Boustani, Chem. Phys. Lett. **379**, 282–286 (2003).

[11] H.J. Zhai, L.S. Wang, A.N. Alexandrova, and A.I. Boldyrev, J. Chem. Phys. **117**, 7917–7924 (2002).

[12] R. Kawai and J.H. Weare, J. Chem. Phys. **95**, 1151–1159 (1991).

[13] R. Kawai and J.H. Weare, Chem. Phys. Lett. **191**, 311–314 (1992).

[14] V. Bonacic-Koutecky, P. Fantucci, and J. Koutecky, Chem. Rev. **91**, 1035–1108 (1991).

[15] H. Kato, K. Yamashita, and K. Morokuma, Chem. Phys. Lett. **190**, 361–366 (1992).

[16] I. Boustani, Chem. Phys. Lett. **240**, 135–140 (1995).

[17] I. Boustani, Phys. Rev. B. **55**, 16426–16438 (1997).

[18] A. Ricca and C.W. Bauschlicher Jr, Chem. Phys. Lett. **208**, 233–242 (1996).

[19] A. Ricca and C.W. Bauschlicher Jr., J. Chem. Phys. **106**, 2317–2322 (1997).

[20] J.E. Fowler and J.M. Ugalde, J. Phys. Chem. A. **104**, 397–403 (2000).

[21] J. Aihara, J. Phys. Chem. A. **105**, 5486–5489 (2001).

[22] A.N. Alexandrova, A.I. Boldyrev, H.J. Zhai, L.S. Wang, E. Steiner, and P.W. Fowler, J. Phys. Chem. A. **107**, 1359–1369 (2003).

[23] Z.H. Zhai, L.S. Wang, A.N. Alexandrova, A.I. Boldyrev, and V.G. Zakrzewski, J. Phys. Chem. A. **107**, 9319–9328 (2003).

[24] H.J. Zhai, A.N. Alexandrova, K.A. Birch, A.I. Boldyrev, and L.S. Wang, Angew. Chem. Int. Ed. **42**, 6004–6008 (2003).

[25] H.J. Zhai, B. Kiran, J. Li, and L.S. Wang, Nat. Mater. **2**, 827–833 (2003).

[26] A.N. Alexandrova, A.I. Boldyrev, H.J. Zhai, and L.S. Wang, J. Phys. Chem. A. **108**, 3509–3517 (2004).

[27] B. Kiran, S. Bulusu, H.J. Zhai, S. Yoo, X.C. Zeng, and L.S. Wang, Proc. Natl. Acad. Sci. **102**, 961–964 (2005).

[28] A.N. Alexandrova, A.I. Boldyrev, H.J. Zhai, and L.S. Wang, Coord. Chem. Rev. **250**, 2811–2866 (2006).

[29] A.P. Sergeeva, D.Y. Zubarev, H.J. Zhai, A.I. Boldyrev, and L.S. Wang, J. Am. Chem. Soc. **130**, 7244–7246 (2008).

[30] W. Huang, A.P. Sergeeva, H.J. Zhai, B.B. Averkiev, L.S. Wang, and A.I. Boldyrev, Nat. Chem. **2**, 202–206 (2010).
[31] A.P. Sergeeva, B.B. Averkiev, H.J. Zhai, A.I. Boldyrev, and L.S. Wang, J. Chem. Phys. **134**, 224304 (2011).
[32] Z.A. Piazza, W.L. Li, C. Romanescu, A.P. Sergeeva, L.S. Wang, and A.I. Boldyrev, J. Chem. Phys. **136**, 104310 (2012).
[33] A.P. Sergeeva, Z.A. Piazza, C. Romanescu, W.L. Li, A.I. Boldyrev, and L.S. Wang, J. Am. Chem. Soc. **134**, 18065–18073 (2012).
[34] I.A. Popov, Z.A. Piazza, W.L. Li, L.S. Wang, and A.I. Boldyrev, J. Chem. Phys. **139**, 144307 (2013).
[35] Z.A. Piazza, I.A. Popov, W.L. Li, R. Pal, X.C. Zeng, A.I. Boldyrev, and L.S. Wang, J. Chem. Phys. **141**, 034303 (2014).
[36] W.L. Li, R. Pal, Z.A. Piazza, X.C. Zeng, and L.S. Wang, J. Chem. Phys. **142**, 204305 (2015).
[37] C. Romanescu, T.R. Galeev, W.L. Li, A.I. Boldyrev, and L.S. Wang, Acc. Chem. Res. **46**, 350–358 (2013).
[38] C. Romanescu, T.R. Galeev, W.L. Li, A.I. Boldyrev, and L.S. Wang, Angew. Chem. Int. Ed. **50**, 9334–9337 (2011).
[39] W.L. Li, C. Romanescu, T.R. Galeev, Z.A. Piazza, A.I. Boldyrev, and L.S. Wang, J. Am. Chem. Soc. **134**, 165–168 (2012).
[40] T.R. Galeev, C. Romanescu, W.L. Li, L.S. Wang, and A.I. Boldyrev, Angew. Chem. Int. Ed. **51**, 2101–2105 (2012).
[41] W.L. Li, C. Romanescu, Z.A. Piazza, and L.S. Wang, Phys. Chem. Chem. Phys. **14**, 13663–13669 (2012).
[42] C. Romanescu, T.R. Galeev, A.P. Sergeeva, W.L. Li, L.S. Wang, and A.I. Boldyrev, J. Organomet. Chem. **721–722**, 148–154 (2012).
[43] C. Romanescu, T.R. Galeev, W.L. Li, A.I. Boldyrev, and L.S. Wang, J. Chem. Phys. **138**, 134315 (2013).
[44] W.L. Li, A.S. Ivanov, J. Federič, C. Romanescu, I. Černušák, A.I. Boldyrev, and L.S. Wang, J. Chem. Phys. **139**, 104312 (2013).
[45] Z.A. Piazza, H.S. Hu, W.L. Li, Y.F. Zhao, J. Li, and L.S. Wang, Nat. Commun. **5**, 3113 (2014).
[46] H.J. Zhai, Y.F. Zhao, W.L. Li, Q. Chen, H. Bai, H.S. Hu, Z.A. Piazza, W.J. Tian, H.G. Lu, Y.B. Wu, Y.W. Mu, G.F. Wei, Z.P. Liu, J. Li, S.D. Li, and L.S. Wang, Nat. Chem. **6**, 727–731 (2014).
[47] A.P. Sergeeva, I.A. Popov, Z.A. Piazza, W.L. Li, C. Romanescu, L.S. Wang, and A.I. Boldyrev, Acc. Chem. Res. **47**, 1349–1358 (2014).
[48] J.R. Rabalais, *Principle of Ultraviolet Photoelectron Spectroscopy*, (Wiley, New York, 1977).
[49] D.G. Leopold and W.C. Lineberger, J. Chem. Phys. **85**, 51–55 (1986).
[50] O. Cheshnovsky, S.H. Yang, C.L. Pettiette, M.J. Craycraft, and R.E. Smalley, Rev. Sci. Instrum. **58**, 2131–2137 (1987).
[51] G. Gantefor, K.H. Meiwes-Broer, and H.O. Lutz, Phys. Rev. A. **37**, 2716–2718 (1988).
[52] K.M. McHugh, J.G. Eaton, G.H. Lee, H.W. Sarkas, L.H. Kidder, J.T. Snodgrass, M.R. Manaa, and K.H. Bowen, J. Chem. Phys. **91**, 3792–3793 (1989).
[53] S.M. Casey and D.G. Leopold, J. Phys. Chem. **97**, 816–830 (1993).
[54] C.C. Arnold and D.M. Neumark, J. Chem. Phys. **99**, 3353–3362 (1993).
[55] J. Fan, and L.S. Wang, J. Phys. Chem. **98**, 11814–11817 (1994).
[56] H. Handschuh, G. Gantefor, and W. Eberhardt, Rev. Sci. Instrum. **66**, 3838–3843 (1995).
[57] N. Zhang, H. Kawamata, A. Nakajima, and K. Kaya, J. Chem. Phys. **104**, 36–41 (1996).
[58] H. Yoshida, A. Terasaki, K. Kobayashi, M. Tsukada, and T. Kondow, J. Chem. Phys. **102**, 5960 (1995).
[59] G. Wrigge, M.A. Hoffmann, and B.V. Issendorff, Phys. Rev. A. **65**, 063201 (2002).

[60] P. Kruit and F.H. Read, J. Phys. E: Sci. Instrum. **16**, 313–324 (1983).

[61] L.S. Wang, H.S. Cheng, and J. Fan, J. Chem. Phys. **102**, 9480–9493 (1995).

[62] L.S. Wang and H.Wu, in *Advances in Metal and Semiconductor Clusters. IV. Cluster Materials*, edited by M.A. Duncan, (JAI Press, Greenwich, 1998), pp. 299–343.

[63] E.A. Rohlfing, D.M. Cox, and A. Kaldor, J. Chem. Phys. **81**, 3322–3330 (1984).

[64] H.W. Kroto, J.R. Heath, S.C. O'Brien, R.F. Curl, and R.E. Smalley, Nature. **318**, 162–163 (1985).

[65] H. Wu, S.R. Desai, and L.S. Wang, J. Phys. Chem. A. **101**, 2103–2111 (1997).

[66] O. Kostko, B. Huber, M. Moseler, and B. von Issendorff. Phys. Rev. Lett. **98**, 043401 (2007).

[67] X.B. Wang and L.S. Wang, Rev. Sci. Instrum. **79**, 073108 (2008).

[68] C. Hock, J.B. Kim, M.L. Weichman, T.I. Yacovitch, and D.M. Neumark, J. Chem. Phys. **137**, 244201 (2012).

[69] L.S. Wang, J. Conceicao, C. Jin, and R.E. Smalley, Chem. Phys. Lett. **182**, 5–11 (1991).

[70] X. Li, H. Wu, X.B. Wang, and L.S. Wang, Phys. Rev. Lett. **81**, 1909–1912 (1998).

[71] L.S. Wang and X. Li, in *Anion photoelectron spectroscopy of metal clusters in clusters and nanostructure interfaces*, edited by P. Jena, S.N. Khanna, and B.K. Rao (World Scientific, River Edge, NJ, 2000), pp. 293–300.

[72] J. Akola, M. Manninen, H. Hakkinen, U. Landman, X. Li, and L.S. Wang, Phys. Rev. B. **60**, 11297–11300(R) (1999).

[73] W. Huang and L.S. Wang, Phys. Chem. Chem. Phys. **11**, 2663–2667 (2009).

[74] W. Huang and L.S. Wang, Phys. Rev. Lett. **102**, 153401 (2009).

[75] W. Huang, S. Bulusu, R. Pal, X.C. Zeng, and L.S. Wang, ACS Nano. **3**, 1225–1230 (2009).

[76] Y. Gao, W. Huang, J. Woodford, L.S. Wang, and X.C. Zeng, J. Am. Chem. Soc. **131**, 9484–9485 (2009).

[77] E. Oger, N.R.M. Crawford, R. Kelting, P. Weis, M.M. Kappes, and R. Ahlrichs, Angew. Chem. Int. Ed. **46**, 8503–8506 (2007).

[78] C. Romanescu, D.J. Harding, A. Fielicke, and L.S. Wang, J. Chem. Phys. **137**, 014317 (2012).

[79] L.L. Pan, J. Li, and L.S. Wang, J. Chem. Phys. **129**, 024302 (2008).

[80] T.B. Tai, D.J. Grant, M.T. Nguyen, and D.A. Dixon, J. Phys. Chem. A. **114**, 994–1007 (2010).

[81] L.J. Cheng, J. Chem. Phys. **136**, 104301 (2012).

[82] T.B. Tai, N.M. Tam, and M.T. Nguyen, Theor. Chem. Acc. **131**, 1241 (2012).

[83] A.G. Arvanitidis, T.B. Tai, M.T. Nguyen, and A. Ceulemans, Phys. Chem. Chem. Phys. **16**, 18311–18318 (2014).

[84] D.Y. Zubarev and A.I. Boldyrev, J. Comput. Chem. **28**, 251–268 (2007).

[85] D.Y. Zubarev and A.I. Boldyrev, Phys. Chem. Chem. Phys. **10**, 5207–5217 (2007).

[86] C. Romanescu, A.P. Sergeeva, W.L. Li, A.I. Boldyrev, and L.S. Wang, J. Am. Chem. Soc. **133**, 8646–8653 (2011).

[87] T.R. Galeev, C. Romanescu, W.L. Li, L.S. Wang, and A.I. Boldyrev, J. Chem. Phys. **135**, 104301 (2011).

[88] W.L. Li, C. Romanescu, T.R. Galeev, L.S. Wang, and A.I. Boldyrev, J. Phys. Chem. A. **115**, 10391–10397 (2011).

[89] B.B. Averkiev and A.I. Boldyrev, Russ. J. Gen. Chem. **78**, 769–773 (2008).

[90] L.M. Wang, W. Huang, B.B. Averkiev, A.I. Boldyrev, and L.S. Wang, Angew. Chem. Int. Ed. **46**, 4550–4553 (2007).

[91] B.B. Averkiev, D.Y. Zubarev, L.M. Wang, W. Huang, L.S. Wang, and A.I. Boldyrev, J. Am. Chem. Soc. **130**, 9248–9250 (2008).

[92] B.B. Averkiev, L.M. Wang, W. Huang, L.S. Wang, and A.I. Boldyrev, Phys. Chem. Chem. Phys. **11**, 9840–9849 (2009).

[93] T.R. Galeev, A.S. Ivanov, C. Romanescu, W.L. Li, K.V. Bozhenko, L.S. Wang, and A.I. Boldyrev, Phys. Chem. Chem. Phys. **13**, 8805–8810 (2011).

[94] T.R. Galeev, W.L. Li, C. Romanescu, I. Černušák, L.S. Wang, and A.I. Boldyrev, J. Chem. Phys. **137**, 234306 (2012).

[95] H.J. Zhai, C.Q. Miao, S.D. Li, and L.S. Wang, J. Phys. Chem. A. **114**, 12155–12161 (2010).

[96] Q. Chen, H.J. Zhai, S.D. Li, and L.S. Wang, J. Chem. Phys. **138**, 084306 (2013).

[97] H. Bai, H.J. Zhai, S.D. Li, and L.S. Wang, Phys. Chem. Chem. Phys. **15**, 9646–9653 (2013).

[98] D.Y. Zubarev and A.I. Boldyrev, J. Org. Chem. **73**, 9251–9258 (2008).

[99] T.R. Galeev, Q. Chen, J.C. Guo, H. Bai, C.Q. Miao, H.G. Lu, A.P. Sergeeva, S.D. Li, and A.I. Boldyrev, Phys. Chem. Chem. Phys. **13**, 11575–11578 (2011).

[100] I.A. Popov and A.I. Boldyrev, J. Phys. Chem. C. **116**, 3147–3152 (2012).

[101] J.P. Foster and F. Weinhold, J. Am. Chem. Soc. **102**, 7211–7218 (1980).

[102] D.C. Parent and M.T. Bowers, Chem. Phys. **60**, 257–275 (1981).

[103] F. Furche, R. Ahlrichs, P. Weis, C. Jacob, S. Gilb, T. Bierweiler, and M.M. Kappes, J. Chem. Phys. **117**, 6982–6990 (2002).

[104] A.N. Alexandrova, A.I. Boldyrev, Y.J. Fu, X. Yang, X.B. Wang, and L.S. Wang, J. Chem. Phys. **121**, 5709–5719 (2004).

[105] A.N. Alexandrova and A.I. Boldyrev, J. Chem. Theory Comput. **1**, 566–580 (2005).

[106] M. Saunders, J. Comput. Chem. **25**, 621–626 (2004).

[107] D.J. Wales and J.P.K. Doye, J. Phys. Chem. A. **101**, 5111–5116 (1997).

[108] I. Boustani, Z. Zhu, and D. Tománek, Phys. Rev. B. **83**, 193405 (2011).

[109] J.O.C. Jiménez-Halla, R. Islas, T. Heine, and G. Merino, Angew. Chem. Int. Ed. **49**, 5668–5671 (2010).

[110] F. Cervantes-Navarro, G. Martínez-Guajardo, E. Osorio, D. Moreno, W. Tiznado, R. Islas, K.J. Donald, and G. Merino, Chem. Commun. **50**, 10680–10682 (2014).

[111] G. Martínez-Guajardo, A.P. Sergeeva, A.I. Boldyrev, T. Heine, J.M. Ugalde, and G. Merino, Chem. Commun. **47**, 6242–6244 (2011).

[112] J. Zhang, A.P. Sergeeva, M. Sparta, and A.N. Alexandrova, Angew. Chem. Int. Ed. **51**, 8512–8515 (2012).

[113] T.B. Tai, A. Ceulemans, and M.T. Nguyen, Chem. Eur. J. **18**, 4510–4512 (2012).

[114] T.B. Tai, R.W.A. Havenith, J.L. Teunissen, A.R. Dok, S.D. Hallaert, M.T. Nguyen, and A. Ceulemans, Inorg. Chem. **52**, 10595–10600 (2013).

[115] D. Moreno, S. Pan, L.L. Zeonjuk, R. Islas, E. Osorio, G. Martínez-Guajardo, P.K. Chattaraj, T. Heine, and G. Merino, Chem. Commun. **50**, 8140–8143 (2014).

[116] W. An, S. Bulusu, Y. Gao, and X.C. Zeng, J. Chem. Phys. **124**, 154310 (2006).

[117] F.Y. Tian and Y.X. Wang, J. Chem. Phys. **129**, 024903 (2008).

[118] M.P. Johansson, J. Phys. Chem. C. **113**, 524–530 (2009).

[119] D.E. Bean and P.W. Fowler, J. Phys. Chem. C. **113**, 15569–15575 (2009).

[120] M. Atis, C. Ozdogan, and Z.B. Guvenc, Chin. J. Chem. Phys. **22**, 380–388 (2009).

[121] T.B. Tai, N.M. Tam, and M.T. Nguyen, Chem. Phys. Lett. **530**, 71–76 (2012).

[122] Y. Yuan and L.J. Cheng, J. Chem. Phys. **137**, 044308 (2012).

[123] H.G. Lu and S.D. Li, J. Chem. Phys. **139**, 224307 (2013).

[124] H.T. Tam, L.V. Duong, and M.T. Nguyen, J. Phys. Chem. C. **118**, 24181–24187 (2014).

[125] R. Casillas, T. Baruah, and R.R. Zope, Chem. Phys. Lett. **557**, 15–18 (2013).

[126] B.C. Hikmat, T. Baruah, and R.R. Zope, J. Phys. B: At. Mol. Opt. Phys. **45**, 225101 (2012).

[127] H.T. Pham, L.V. Duong, B.Q. Pham, and M.T. Nguyen, Chem. Phys. Lett. **577**, 32–37 (2013).

[128] S. Chacko, D.G. Kanhere, and I. Boustani, Phys. Rev. B. **68**, 035414 (2003).

[129] T.B. Tai and M.T. Nguyen, Phys. Chem. Chem. Phys. **17**, 13672–13679 (2015).

[130] W.L. Li, Y.F. Zhao, H.S. Hu, J. Li, and L.S. Wang, Angew. Chem. Int. Ed. **53**, 5540–5545 (2014).

[131] W.L. Li, Q. Chen, W.J. Tian, H. Bai, Y.F. Zhao, H.S. Hu, J. Li, H.J. Zhai, S.D. Li, and L.S. Wang, J. Am. Chem. Soc. **136**, 12257–12260 (2014).

[132] Q. Chen, W.L. Li, Y.F. Zhao, S.Y. Zhang, H.S. Hu, H. Bai, H.R. Li, W.J. Tian, H.G. Lu, H.J. Zhai, S.D. Li, J. Li, and L.S. Wang, ACS Nano. **9**, 754–760 (2015).

[133] Q. Chen, G.F. Wei, W.J. Tian, H. Bai, Z.P. Liu, H.J. Zhai, and S.D. Li, Phys. Chem. Chem. Phys. **16**, 18282–18287 (2015).

[134] I. Boustani and A. Quandt, Europhys. Lett. **39**, 527–532 (1997).

[135] A. Gindulyte, W.N. Lipscomb, and N.L. Massa, Inorg. Chem. **37**, 6544–6545 (1998).

[136] I. Boustani, A. Quandt, E. Hernández, and A. Rubio, J. Chem. Phys. **110**, 3176–3185 (1999).

[137] M.H. Evans, J.D. Joannopoulos, and S.T. Pantelides, Phys. Rev. B. **72**, 045434 (2005).

[138] J. Kunstmann and A. Quandt, Phys. Rev. B. **74**, 035413 (2006).

[139] K.C. Lau and R. Pandey, J. Phys. Chem. C. **111**, 2906–2912 (2007).

[140] H. Tang and S. Ismail-Beigi, Phys. Rev. Lett. **99**, 115501 (2007).

[141] X. Yang, Y. Ding, and J. Ni, Phys. Rev. B. **77**, 041402 (2008).

[142] J. Kunstmann, V. Bezugly, H. Rabbel, M.H. Rümmeli, and G. Cuniberti, Adv. Funct. Mater. **24**, 4127–4134 (2014).

[143] E.S. Penev, S. Bhowmick, A. Sadrzadeh, and B.I. Yakobson, Nano Lett. **12**, 2441–2445 (2012).

[144] X. Wu, J. Dai, Y. Zhao, A. Zhuo, J. Yang, and X.C. Zeng, ACS Nano. **6**, 7443–7453 (2012).

[145] H. Lu, Y. Mu, H. Bai, Q. Chen, and S.D. Li, J. Chem. Phys. **138**, 024701 (2013).

[146] Y. Liu, E.S. Penev, and B.I. Yakobson, Angew. Chem. Int. Ed. **52**, 3156–3159 (2013).

[147] H. Liu, J. Gao, and J. Zhao, Sci. Rep. **3**, 3228 (2013).

[148] Z. Zhang, Y. Yang, G. Gao, and B.I. Yakobson, Angew. Chem. Int. Ed. **54**, 1–6 (2015).

[149] S.G. Xu, Y.J. Zhao, J.H. Liao, and X.B. Yang, J. Chem. Phys. **142**, 214307 (2015).

[150] A.B. Rahane and V. Kumar, Nanoscale. **7**, 4055–4062 (2015).

[151] S. Goedecker, J. Chem. Phys. **120**, 9911–9917 (2004).

[152] T.B. Tai, L.V. Duong, H.T. Pham, D.T.T. Mai, and M.T. Nguyen, Chem. Commun. **50**, 1558–1560 (2014).

[153] C. Shang and Z.P. Liu, J. Chem. Theory Comput. **9**, 1838–1845 (2013).

[154] N.G. Szwacki, A. Sadrzadeh, and B.I. Yakobson, Phys. Rev. Lett. **98**, 166804 (2007). [Erratum: Phys. Rev. Lett. **100**, 159901 (2008)]

[155] D.L.V.K. Prasad and E.D. Jemmis, Phys. Rev. Lett. **100**, 165504 (2008).

[156] H. Li, N. Shao, B. Shang, L.F. Yuan, J. Yang, and X.C. Zeng, Chem. Commun. **46**, 3878–3880 (2010).

[157] S. De, A. Willand, M. Amsler, P. Pochet, L. Genovese, and S. Goedecker, Phys. Rev. Lett. **106**, 225502 (2011).

[158] F. Li, P. Jin, D.E. Jiang, L. Wang, S.B. Zhang, J. Zhao, and Z. Chen, J. Chem. Phys. **136**, 074302 (2012).

[159] R. He and X.C. Zeng, Chem. Commun. **51**, 3185–3188 (2015).

[160] G. Martínez-Guajardo, J.L. Luis Cabellos, A. Díaz-Celaya, S. Pan, R. Islas, P.K. Chattaraj, T. Heine, and G. Merino, Sci. Rep. **5**, 11287 (2015).

[161] D.M. Hudgins, C.W. Bauschlicher Jr, and L.J. Allamandola, Spectrochim. Acta Part A. **57**, 907–930 (2001).

[162] A.C. Tang, Q.S. Li, C.W. Liu, and J. Li, Chem. Phys. Lett. **201**, 465–469 (1993).

[163] I. Boustani, A. Rubio, and J.A. Alonso, Chem. Phys. Lett. **311**, 21–28 (1999).

[164] Q.B. Yan, X.L. Sheng, Q.R. Zheng, L.Z. Zhang, and G. Su, Phys. Rev. B. **78**, 201401(R) (2008).

[165] R.R. Zope, Europhys. Lett. **85**, 68005 (2009).

[166] L. Wang, J. Zhao, F. Li, and Z. Chen, Chem. Phys. Lett. **501**, 16–19 (2010).

[167] W. Hayami and S. Otani, J. Phys. Chem. A. **115**, 8204–8207 (2011).
[168] J. Lv, Y. Wang, L. Zhu, and Y. Ma, Nanoscale. **6**, 11692–11696 (2014).
[169] T.B. Tai, and M.T. Nguyen, Nanoscale. **7**, 3316–3317 (2015).
[170] J. Zhao, X. Huang, R. Shi, H. Liu, Y. Su, and R.B. King, Nanoscale. **7**, 15086–15090 (2015).
[171] Y.J. Wang, Y.F. Zhao, W.L. Li, T. Jian, Q. Chen, X.R. You, T. Ou, X.Y. Zhao, H.J. Zhai, S.D. Li, J. Li, and L.S. Wang, J. Chem. Phys. **144**, 064307 (2016).
[172] L.S. Wang, J.M. Alford, Y. Chai, M. Diener, J. Zhang, S.M. McClure, T. Guo, G.E. Scuseria, and R.E. Smalley, Chem. Phys. Lett. **207**, 354–359 (1993).
[173] A.A. Popov, S. Yang, and L. Dunsch, Chem. Rev. **113**, 5989–6113 (2013).
[174] P. Jin, Q. Hou, C. Tang, and Z. Chen, Theor. Chem. Acc. **134**, 13 (2015).
[175] H. Bai, Q. Chen, H.J. Zhai, and S.D. Li, Angew. Chem. Int. Ed. **54**, 941–945 (2015).
[176] Q. Chen, S.Y. Zhang, H. Bai, W.J. Tian, T. Gao, H.R. Li, C.Q. Miao, Y.W. Mu, H.G. Lu, H.J. Zhai, and S.D. Li, Angew. Chem. Int. Ed. **54**, 8160–8164 (2015).
[177] Q. Chen, T. Gao, W.J. Tian, H. Bai, S.Y. Zhang, H.R. Li, C.Q. Miao, Y.W. Mu, H.G. Lu, H.J. Zhai, and S.D. Li, Phys. Chem. Chem. Phys. **17**, 19690–19694 (2015).
[178] N.G. Gonzalez Szwacki, Nanoscale Res. Lett. **3**, 49–54 (2008).
[179] R.R. Zope, T. Baruah, K.C. Lau, A.Y. Liu, M.R. Pederson, and B.I. Dunlap, Phys. Rev. B. **79**, 161403(R) (2009).
[180] C. Özdoğan, S. Mukhopadhyay, W. Hayami, Z.B. Güvenç, R. Pandey, and I. Boustani, J. Phys. Chem. C. **114**, 4362–4375 (2010).
[181] B. Shang, L.F. Yuan, X.C. Zeng, and J. Yang, J. Phys. Chem. A. **114**, 2245–2249 (2010).
[182] J.T. Muya, G. Gopakumar, M.T. Nguyen, and A. Ceulemans, Phys. Chem. Chem. Phys. **13**, 7524–7533 (2011).
[183] R.R. Zope and T. Baruah, Chem. Phys. Lett. **501**, 193–196 (2011).
[184] P.A. Troshin, A.G. Avent, A.D. Darwish, N. Martsinovich, A. Abdul-Sada, J.M. Street, and R. Taylor, Science. **309**, 278–281 (2005).
[185] Y.Z. Tan, R.T. Chen, Z.J. Liao, J. Li, F. Zhu, X. Lu, S.Y. Xie, J. Li, R.B. Huang, and L.S. Zheng, Nat. Commun. **2**, 420 (2011).
[186] S. Yang, S. Wang, E. Kemnitz, and S.I. Troyanov, Angew. Chem. Int. Ed. **53**, 2460–2463 (2014).